ALMA MATER STUDIORUM – Università di Bologna

School of Science
Department of Physics and Astronomy
Master Degree Programme in Astrophysics and Cosmology

A full simulations pipeline for Coupled Dark Energy models with PANDA-Gadget4

Graduation Thesis

Presented by:
Daniele Tamburri

Supervisor:
Prof. Marco Baldi

Co-supervisors:
Dott. Alessandro Casalino
Dott. Fulvio Ferlito

Academic Year: [2024-2025]
Graduation Date: I

Abstract

The ΛCDM model is founded evidence of non-baryonic cold dark matter (CDM), which dominates the matter content of the Universe, and a cosmological constant Λ in the assumption of a spatially flat universe. While it successfully explains a broad range of cosmological observations, in the last years, with the increase of the experimental sensitivity, statistically significant tensions have emerged among different observations on the Hubble parameter H_0, the amplitude of the growth of structure S_8 and the dark energy equation-of-state parameter w. These discrepancies motivate the exploration of alternative DE models.

In this work, we focus our study in a particular class of Coupled Dark Energy models, where DE component is represented a scalar field which evolves under a confining self-interaction potential and interacts with other species. These models, named Bouncing Coupled Dark Energy (BCDE) models, present a peculiar dynamic represented by a bouncing point in which the field stop and inverts in motion. This dynamic may alleviate the observed tensions by suppressing the growth of structure at late-times. To test these models at the non linear regime of the structure formation, we developed a new implementation of the `PANDA-Gdget4` N-body code. Our modifications incorporate the key physical effects of BCDE, including the mass evolution of coupled particles, a velocity-dependent friction term, and a fifth force which enhances the gravitational interaction. This new implementation not only enables the study of BCDE cosmologies but also provides a foundation for simulating a broader class of Interacting Dark Energy (IDE) models. Using our implementation, we perform cosmological simulations and analyze their outcomes with the newly developed DORIAN Python library, which extracts weak lensing observables from `Gadget4` lightcone outputs. Our results highlight the distinct signatures of BCDE models in the matter power spectrum, halo mass function, and weak lensing signals, offering testable predictions for future observational surveys.

Together, this pipeline, from theoretical analysis of dark energy models to their non-linear evolution with our new implementation in `PANDA-Gadget` and observational signatures in weak lensing with DORIAN, provides a robust toolset to test and constrain coupled dark energy scenarios with upcoming cosmological data.

Contents

Chapter 1

Introduction

Cosmology can be defined as the study of the universe regarded as a whole.

One of the most fundamental ideas in Cosmology is the Cosmological Principle which asserts that, on sufficiently large scales, the Universe is both homogeneous and isotropic. In other words, no location or direction in the universe is favored with respect to others when viewed at large scales.

Obviously the universe is not perfectly homogeneous or isotropic on small scales, as the distribution of stars, galaxies and clusters forms a highly structured pattern. However, when observed at scales much larger than those of individual galaxies or galaxy clusters, the universe starts to appear more homogeneous.

The Cosmological Principle was first introduced by Einstein as a simplifying assumption (Einstein, 1917), but later has been supported by extensive observations. Measurements on Cosmic Microwave Background (CMB) strongly suggest an universe which is uniform in all directions, (Aghanim et al., 2020). Additionally, large-scale galaxy surveys demonstrate that the distribution of matter becomes increasingly uniform when examined over large distances, (Yadav et al., 2005).

In this chapter, we will present the fundamental concepts and theoretical frameworks that feature modern cosmology. We will begin by outlining the essentials of General Relativity and the FLRW metric, followed by a discussion of cosmological distances and the Hubble law. Subsequently, we will explore the role of the cosmological constant and the Friedmann models, examine linear perturbation theory, and discuss the statistical properties of cosmic structure. Finally, we will review key observational constraints and the successes and challenges of the ΛCDM model in describing our Universe.

1.1 Fundamentals of General Relativity

The aim of cosmology is to construct theoretical models that explain and predict the observed properties and behavior of the universe, from its large-scale structure to its evolution over time.

On large scales, the dominant force is gravity, so the most important ingredient for a Cosmological model to physically describe the Universe is a theory of gravity.

The best gravitational theory we have so far is Einstein's General Relativity (Einstein, 1915; Will, 2014; Abbott et al., 2016) .

General Relativity links the geometrical properties of the Universe with its energy content.

In Special Relativity (Einstein, 1905), the invariant interval between two events, located at coordinates (t, x, y, z) and $(t + dt, x + dx, y + dy, z + dz)$, is defined as:

$$ds^2 = c^2dt^2 - (dx^2 + dy^2 + dz^2)\,, \tag{1.1}$$

where ds^2 is invariant under a change of coordinate system. For material particles moving under no external forces, their trajectories between two events are those that make the value of $\int ds$ stationary, corresponding to straight-line motion between points, representing the shortest distance in spacetime.

When external forces like gravity or electromagnetism act, they cause deviations from these straight-line trajectories. Gravity exerts the same force per unit mass on all objects, this principle is called Equivalence Principle and is the fundamental pillar of General Relativity. Einstein's theory of General Relativity reformulates gravity not as a force but as a property of spacetime itself. Unlike the flat geometry of Minkowski spacetime, representative of the Special Relativity, General Relativity allows spacetime to be curved. In this framework, the interval between two event is expressed as:

$$ds^2 = g_{\mu\nu}(x)dx^\mu dx^\nu\,,$$

where we used the Einstein summation convention for which repeated indices imply summation. The indices μ, ν range from 0 to 3, $x^0 = ct$ represent the time coordinate, while x^1, x^2, x^3 the three spatial coordinates. The metric returns the actual physical distance between two infinitesimally close points in spacetime defined in some arbitrary coordinate system. The metric tensor $g_{\mu\nu}$ encodes the geometry of spacetime, determining how distances and intervals are measured in a curved spacetime.

As mentioned above, particles move in the spacetime in such a way that the integral along their path is stationary:

$$\delta \int_{path} ds = 0 \tag{1.2}$$

but in the presence of a gravitational field, these trajectories are no longer straight and, from the stationary condition, it can be proved that the path of a free particle is described by the geodesic equation:

$$\frac{d^2x^\lambda}{d\tau^2} + \Gamma^\lambda_{\mu\nu}\frac{dx^\mu}{d\tau}\frac{dx^\nu}{d\tau} = 0\,, \tag{1.3}$$

where Γ is called Christoffel symbol and describes the gravitational force acting on the particle. It can also be shown that the following relation between the Christoffel symbol and the metric tensor holds

$$\Gamma^{\rho}_{\lambda\mu} = \frac{1}{2} g^{\rho\nu} \left(\frac{\partial g_{\mu\nu}}{\partial x^{\lambda}} + \frac{\partial g_{\lambda\nu}}{\partial x^{\mu}} + \frac{\partial g_{\mu\lambda}}{\partial x^{\nu}} \right). \tag{1.4}$$

The key factor in Einstein's equations is the relationship between the distribution of matter and the metric describing the space–time geometry. The energy content of the universe is described by the energy-momentum tensor $T_{\mu\nu}$ which, considering a perfect fluid with pressure p and energy density ρ is defined as

$$T_{\mu\nu} = (p + \rho c^2) u_{\mu} u_{\nu} - p g_{\mu\nu} \,, \tag{1.5}$$

where u_{μ}, u_{ν} are the fluid four-vectors defined as

$$u_{\mu} = g_{\mu\nu} u^{\nu} = g_{\mu\nu} \frac{dx^{\nu}}{d\tau} \,, \tag{1.6}$$

and τ represent the proper time $c^2 d\tau^2 = -ds^2$

In General Relativity, writing conservation equations requires taking derivatives of tensors, such as the energy-momentum tensor $T_{\mu\nu}$. However, the ordinary partial derivative of a tensor is not itself a tensor, because it does not transform properly under general coordinate changes. To account for this, we introduce the covariant derivative, which includes correction terms involving the Christoffel symbols $\Gamma^{\lambda}_{\mu\nu}$. These terms ensure that the derivative remains tensorial, preserving proper transformation properties under coordinate transformations. We can then define the covariant derivative ∇_{μ}, applied to a general tensor V^{μ}_{ν} as

$$\nabla_{\alpha} V^{\mu}_{\nu} = \partial_{\alpha} V^{\mu}_{\nu} + \Gamma^{\mu}_{\lambda\alpha} V^{\lambda}_{\nu} - \Gamma^{\lambda}_{\alpha\nu} V^{\mu}_{\lambda} \,. \tag{1.7}$$

In this way, the correct conservation equation of the energy-momentum tensor can be written as

$$\nabla_{\mu} T^{\mu}_{\nu} = 0 \,. \tag{1.8}$$

To obtain a relation that connects the energy content (represented by energy-momentum tensor $T_{\mu\nu}$) and the geometry of spacetime, which will be some function of $g_{\mu\nu}$, we need to define the Riemann curvature tensor $R^{\lambda}_{\mu\nu\rho}$ as

$$R^{\lambda}_{\mu\nu\rho} \equiv \Big[\nabla_{\mu} \,, \nabla_{\nu} \Big] \,, \tag{1.9}$$

where ∇ represents the covariant derivative and the notation [,] indicates the commutator between two vectors.

It can be shown that equation 1.9 can be rewritten as

$$R^{\lambda}_{\mu\nu\rho} = \partial_{\mu} \Gamma^{\lambda}_{\nu\rho} - \partial_{\nu} \Gamma^{\lambda}_{\mu\rho} + \Gamma^{\lambda}_{\mu\sigma} \Gamma^{\sigma}_{\nu\rho} - \Gamma^{\lambda}_{\nu\sigma} \Gamma^{\sigma}_{\mu\rho} \,, \tag{1.10}$$

and, being Γ a function of the metric tensor $g_{\mu\nu}$, also the Riemann curvature tensor is a function of $g_{\mu\nu}$.

Defining the Ricci tensor $R_{\mu\nu}$ as a contraction of the Riemann curvature tensor, $R_{\mu\nu} \equiv R^{\lambda}_{\lambda\mu\nu}$, and the Ricci scalar R as the contraction of the Ricci tensor, $R \equiv g^{\mu\nu}R_{\mu\nu}$, we can then introduce the Einstein tensor $G_{\mu\nu}$ as:

$$G_{\mu\nu} = R_{\mu\nu} - \frac{1}{2}g_{\mu\nu}R\,. \tag{1.11}$$

Finally, using the Bianchi's identity $\nabla^{\mu}G_{\mu\nu} = 0$ the equation 1.11 leads to

$$R_{\mu\nu} - \frac{1}{2}g_{\mu\nu}R = \frac{8\pi G}{c^4}T_{\mu\nu}\,, \tag{1.12}$$

which is the Einstein field equation. The right-hand side of the Einstein equation represents the source term which is described by the energy-momentum tensor $T_{\mu,\nu}$, while the left-hand side describes the geometry of the space-time.

1.2 FLRW metric

The Cosmological Principle provides the foundation for constructing models of the Universe. Since General Relativity is a theory rooted in geometry, our analysis begins by examining the geometric characteristics of spaces that are homogeneous and isotropic. To simplify, we can model the Universe as a continuous fluid, where each element of the fluid is assigned three spatial coordinates x^i, with $i = 1, 2, 3$. These coordinates, known as comoving coordinates, uniquely identify the position of a fluid element in space. Additionally, every point in space-time can be described by these coordinates and a time parameter τ, which corresponds to the proper time measured by a clock moving with the fluid. The geometric properties of space-time are encoded in the metric. By applying purely geometric reasoning, without resorting to field equations, it can be shown that the most general form of the space-time metric for a Universe obeying the Cosmological Principle is the so called Friedmann-Lemaitre-Robertson-Walker metric (Friedmann, 1922; Lemaître, 1931; Robertson, 1935; Walker, 1937)

$$ds^2 = (cdt)^2 - a(t)^2\left[\frac{dr^2}{1-Kr^2} + r^2(d\theta^2 + sin^2\theta d\phi)\right], \tag{1.13}$$

where r, θ, ϕ are the (spherical polar) comoving coordinates, t is the proper time, $a(t)$ is the cosmic scale factor. The scale factor $a(t)$ is a function used to take into account the expansion of the Universe. The parameter K is a constant which describes the curvature of the Universe and takes only the values 1,0,-1 which correspond to a hypersphere, a Euclidean space and a space of negative curvature, respectively.

As we already mentioned, the Einstein equations of General Relativity link the geometrical properties of space–time with the energy–momentum tensor describing the contents of the Universe. In particular, for a homogeneous and isotropic perfect fluid with rest-mass energy density ρc^2 and pressure p, the solutions of the Einstein equations are the Friedmann cosmological equations

$$\ddot{a} = -\frac{4}{3}\pi G\left(\rho + 3\frac{p}{c^2}\right)a\,, \tag{1.14}$$

$$\dot{a}^2 + Kc^2 = \frac{8\pi G}{3}\rho a^2\,. \tag{1.15}$$

The time evolution of the scale factor $a(t)$ can be obtained from the Friedmann equations assuming an equation of state which relates pressure and density

$$\frac{K}{a^2} = \frac{1}{c^2}H^2\left(\frac{\rho}{\rho_c} - 1\right), \tag{1.16}$$

where

$$\rho_c \equiv \frac{3H}{8\pi G}\,, \quad H \equiv \frac{\dot{a}}{a}\,. \tag{1.17}$$

The quantity $H = \frac{\dot{a}}{a}$ is called Hubble function and it will be explored in detail in the next paragraph.

The parameter $\rho_c(t)$ is called the critical density and is used to define another quantity called the density parameter Ω

$$\Omega(t) = \frac{\rho(t)}{\rho_c(t)}\,. \tag{1.18}$$

We can understand the importance of Ω from equation 1.16 by considering a one-component universe. If the density of the fluid is exactly equal to the critical density, $\rho(t) = \rho_c(t)$, then $\Omega(t) = 1$. Substituting this result into equation 1.16, we find that $K = 0$, so the universe is flat. Similarly, if $\rho(t) > \rho_c(t)$, then $\Omega(t) > 1$, resulting in a positive curvature, $K = 1$, whereas if $\rho(t) < \rho_c(t)$, then $\Omega(t) < 1$, which corresponds to a negative curvature, $K = -1$.

Thus, the critical density $\rho_c(t)$ represents a threshold value for the density to discriminate the geometry of the Universe.

Dividing eq 1.15 by a_0^2, where a_0 corresponds to the scale factor at the present time t_0, one gets:

$$\left(\frac{\dot{a}}{a_0}\right)^2 - \frac{8\pi G}{3}\rho\left(\frac{a}{a_0}\right)^2 = \frac{-Kc^2}{a_0^2}\,.$$

Given the fact that the right term is constant in time, also the left term must be a constant, this means that, to simplify the equation, we can evaluate it at the time $t = t_0$, which leads to

$$\left(\frac{\dot{a}}{a}\right)^2_{t=t_0} - \frac{8\pi G}{3}\rho(t_0)\left(\frac{a_0}{a_0}\right)^2 = H_0^2\left(1 - \frac{\rho_0}{\rho_{0c}}\right) = H_0^2(1-\Omega_0) = -\frac{Kc^2}{a_0^2}\,. \tag{1.19}$$

1.3 The Hubble law

Having defined a metric to describe the geometry of our spacetime, we can calculate the proper distance which separates two points on the spacetime (to simplify, we put ourselves in a frame of reference for which $d\theta = d\phi = 0$ and, of course, $dt = 0$) as

$$d_P = \int_0^r \frac{a}{\sqrt{1 - Kr'^2}} dr' = aF(r)\,, \tag{1.20}$$

where the function $F(r)$ is

$$F(r) = \begin{cases} \sin^{-1} r & (K = 1) \\ r & (K = 0) \\ \sinh^{-1} r & (K = -1) \end{cases} . \tag{1.21}$$

Due to the presence of cosmic expansion, the proper distance at time t is related to that at the present time t_0 by

$$d_P(t_0) = a_0 F(r) = \frac{a_0}{a} d_P(t)\,, \tag{1.22}$$

where $a_0 = a(t_0)$ So, considering only the cosmic expansion (no peculiar velocity), each point at a distance d_P from the origin of our reference frame exhibits a radial velocity

$$v_r = \dot{a}F(r) = \frac{\dot{a}}{a} d_P = H d_P\,, \tag{1.23}$$

where this equation is called the Hubble law (Hubble, 1929). As we anticipated, the quantity $H(t) = \frac{\dot{a(t)}}{a(t)}$ is called Hubble function. Its value computed at the present time $H_0 = H(t = t_0) = 67.4 \pm 0.5 kms^{-1}Mpc^{-1}$(Aghanim et al., 2020), which is called the Hubble constant, is still matter of debate and is the origin of the so-called "H tension", which, as we will see in chapter 1.11.2, constitutes one of the main challenges to the ΛCDM model. To take into account the uncertainty on H_0, the dimensionless Hubble parameter h, defined as

$$h = \frac{H_0}{100\, km\, s^{-1}\, Mpc^{-1}} \tag{1.24}$$

is often used.

1.4 Cosmological Redshift

As the universe expands, radiation traveling through spacetime experiences a stretching of its wavelength, causing photons to shift toward longer wavelengths and redder colors, a phenomenon known as cosmological redshift. The redshift z of a luminous source is defined as

$$z = \frac{\lambda_o - \lambda_e}{\lambda_e}\,, \tag{1.25}$$

where λ_e is the wavelength emitted from the source at time t_e and λ_0 is the wavelength observed at time t_0, with $t_e < t_0$.

The radiation travels along null geodesic, $ds = 0$ in the eq. 1.13, therefore

$$\int_{t_e}^{t_0} \frac{c\,dt}{a(t)} = \int_0^r \frac{dr}{\sqrt{1-Kr^2}} = f(r)\,. \tag{1.26}$$

A second photon emitted at $t'_e = t_e + \delta t_e$ reaches the observer at $t'_0 = t_0 + \delta t_0$. Given that f(r) is only a function of the comoving distance r we can write

$$\int_{t_e}^{t_0} \frac{c\,dt}{a(t)} = \int_{t_e+\delta t_e}^{t_0+\delta t_0} \frac{c\,dt}{a(t)}\,, \tag{1.27}$$

breaking the second integral as $\int_{t_e+\delta t_e}^{t_0+\delta t_0} = \int_{t_e}^{t_0} - \int_{t_e}^{t_e+\delta t_e} + \int_{t_0}^{t_0+\delta t_0}$ the relation becomes

$$\int_{t_e}^{t_e+\delta t_e} \frac{c\,dt}{a(t)} = \int_{t_0}^{t_0+\delta t_0} \frac{c\,dt}{a(t)}\,. \tag{1.28}$$

Assuming that the time interval between the emission and detection of two photons is sufficiently small, we can approximate the scale factor $a(t)$ as constant during this period. This allows us to take it out of the integral, yielding to:

$$\frac{a(t_0)}{a(t_e)} = \frac{\lambda_0}{\lambda_e}\,. \tag{1.29}$$

Using the definition of z in eq. 1.25, we obtain the following relation between the redshift and the scale parameter

$$1 + z = \frac{a_0}{a}\,. \tag{1.30}$$

1.5 Cosmological Distances

In section 1.2 we defined the link between comoving coordinates and proper distance, defining the FLRW (Friedmann-Lemaitre-Robertson-Walker) metric. However, it is not possible to directly measure the proper distances of astronomical objects. Since distant objects are only observed through the light they emit, which requires a finite time to reach us, we cannot make measurements along a surface of constant proper time, but only along sets of light paths traveling to us from the past, i.e., our past light cone. However, we can define other types of distances that are directly measurable.

1.5.1 Luminosity Distance

Considering a source with absolute bolometric luminosity $\mathcal{L}$ at a given comoving coordinate r and time t, given the relation between the luminosity and the flux $\mathcal{F}$ observed at a time t_0 we can define the luminosity distance d_l as

$$d_l = \left(\frac{L}{4\pi\mathcal{F}}\right)^{1/2}\,. \tag{1.31}$$

In the case of a Euclidean, i.e. geometrically flat, universe the flux represents the energy emitted by the source, per unit time, deposited in a spherical area which, at time t_0, is $4\pi a_0^2 r^2$. The photons coming from the source have been redshifted by the universe expansion by a factor a/a_0. Also, the photons emitted by a source in a small interval δt arrive to the observer in an interval $\delta t_0 = (a/a_0)\delta t$ due time-dilation effect. Combining all these effects in equation 1.31 we obtain that the observed flux corresponds to

$$\mathcal{F} = \frac{\mathcal{L}}{4\pi a_0^2 r^2}\left(\frac{a}{a_o}\right)^2 , \tag{1.32}$$

from which one can obtain the luminosity distance

$$d_l = \frac{a_0^2}{a} r = (1+z) a_0 r \, . \tag{1.33}$$

1.5.2 Angular-diameter distance

Let us consider an object at comoving coordinate r at time t with transverse physical size $D_p(t)$. Measuring the angle subtended by D_p as $\Delta\theta$, we can write, in the approximation of a very distant source,

$$D_p = a r \Delta\theta \, , \tag{1.34}$$

from which we can define the angular diameter distance as

$$d_a = \frac{D_p}{\Delta\theta} = a r \, . \tag{1.35}$$

It is interesting to notice that the angular diameter distance and the luminosity distance are related by

$$d_l = (1+z)^2 d_a \, . \tag{1.36}$$

1.6 The cosmological constant Λ

When Einstein formulated his theory of General Relativity, it was generally accepted that the Universe was static. The first Friedmann equation

$$\ddot{a} = -\frac{4}{3}\pi G\left(\rho + 3\frac{p}{c^2}\right) a \, ,$$

shows that the necessary condition for the Universe to be static is:

$$\rho = -3\frac{p}{c^2} \, ,$$

which means a negative energy density or pressure. In other words, considering

$$p = w\rho c^2 \, ,$$

the parameter w must be negative to account for the observed accelerated expansion of the universe. However, within the framework of standard physics, w is typically positive. For instance, non-relativistic matter (dust) has $w = 0$, as it exerts negligible pressure, while radiation and relativistic particles have $w = 1/3$, reflecting the relationship between energy density and pressure in such components. Scalar fields corresponding to ordinary matter or radiation generally yield to $w \geq 0$, therefore, a negative value of w suggests the presence of an exotic component, such as dark energy.

To justify a static universe Einstein modified his equations introducing the cosmological constant Λ

$$R_{i,j} - \frac{1}{2} g_{i,j} R - \Lambda g_{i,j} = \frac{8\pi G}{c^4} T_{i.j} \,. \tag{1.37}$$

If Λ is placed on the left-hand side of the equation, then it affects the geometrical part of the equation, while on the right-hand side it represents a modification of the energy content. In the latter case, considering Λ as a new cosmological fluid component, we obtain:

$$R_{i,j} - \frac{1}{2} g_{i,j} R = \frac{8\pi G}{c^4} \tilde{T}_{i,j} \,,$$

where we defined

$$\tilde{T}_{i,j} = T_{i,j} + \frac{\Lambda c^4}{8\pi G} = -\tilde{p} g_{ij} + (\tilde{p} + \tilde{\rho} c^2) u_i u_j \,, \tag{1.38}$$

and $\tilde{p}, \tilde{\rho}$ are the effective pressure,density corresponding to

$$\tilde{p} = p - p_\Lambda \quad with \quad p_\Lambda = \frac{\Lambda c^4}{8\pi G} \,,$$

$$\tilde{\rho} = \rho + \rho_\Lambda \quad with \quad \rho_\Lambda = \frac{\Lambda c^2}{8\pi G} \,,$$

p_Λ, ρ_Λ are the pressure,density associated to the cosmological constant Λ.

With these assumptions, the new Friedmann equations read

$$\ddot{a} = -\frac{4}{3}\pi G \left(\tilde{\rho} + 3\frac{\tilde{p}}{c^2} \right) a \,,$$

$$\dot{a}^2 + Kc^2 = \frac{8\pi G}{3} \tilde{\rho} a^2 \,.$$

The condition for a static universe now leads to the relation:

$$\tilde{\rho} = -3\frac{\tilde{p}}{c^2} = \frac{3Kc^2}{8\pi G a^2} \,.$$

With the discovery of the expansion of the Universe in the late 1920s (Hubble, 1929; Lemaître, 1931), the idea of a static solution was abandoned and Λ

discarded. Toward the end of the 20th century, a groundbreaking discovery revealed that the universe's expansion is currently accelerating (Riess et al., 1998; Perlmutter et al., 1997). This result reignited interest in the cosmological constant as a repulsive force counteracting the gravitational pull and offering a simple explanation consistent with the latest observations.

Together, the detection of cosmic acceleration and the CDM as the dominant matter component of the Universe (Bertone et al., 2005), form two of the key observational foundations of the currently accepted standard cosmological model.

1.7 Friedmann models

Now we will consider a set of homogeneous and isotropic model universes. The Friedmann models, which form the foundation of modern cosmology, are constructed under the assumptions of a perfect fluid, which presents an energy-momentum tensor described by equation 1.5. In general, we can consider a fluid which is described by the equation of state

$$p = w\rho c^2 \,, \tag{1.39}$$

where the parameter w is a constant and lies in the range $0 \leq w \leq 1$. The case $w \simeq 0$ represent any fluid component with negligible pressure. This is a good approximation for any non-relativistic fluid or gas (even if gas at some temperature exerts some pressure, this typically is way smaller than its rest mass mc^2). Instead, for a fluid composed by photons in thermal equilibrium the equation of state takes the form

$$p = \frac{1}{3}\rho c^2 \,,$$

from which it can be derived the parameter w in case of a fluid composed by photons $w = \frac{1}{3}$.

Assuming an adiabatic expansion of the universe

$$d(\rho c^2 a^3) = -p da^3 \,,$$

if we replace the equation of state inside this adiabatic condition we get for a general fluid component

$$\rho(t) = \rho_0 exp\left[-3\int_1^a \frac{1+w(a')}{a'} da'\right]. \tag{1.40}$$

In the case w is constant in time, w can be moved out of the integral, leading to

$$\rho(t) = \rho_0 \left(\frac{a}{a_0}\right)^{-3(1+w)} . \tag{1.41}$$

This equation represents the evolution in time of the density ρ of a generic cosmic component with equation-of-state parameter w. Each species of the universe, possessing a different parameter w, presents a different density evolution. For matter, $w = 0$,

$$\rho_m(t) = \rho_0 \left(\frac{a}{a_0}\right)^{-3} \quad , \quad \rho_m \propto a^{-3} \,,$$

while for radiation, $w = \frac{1}{3}$,

$$\rho_r(t) = \rho_0 \left(\frac{a}{a_0}\right)^{-4} \quad , \quad \rho_r \propto a^{-4} \,.$$

Using the relation between the scale factor a and the redshift z, eq. 1.30, the conditions read

$$\rho_m(t) = \rho_{0,m}(1+z)^3 \quad , \quad \rho_m \propto (1+z)^3 \,,$$

$$\rho_r(t) = \rho_{0,r}(1+z)^4 \quad , \quad \rho_r \propto (1+z)^4 \,.$$

Is important to notice that, following the definition of p_Λ,ρ_Λ in chapter 1.6, the parameter w associated with the cosmological constant is

$$w_\Lambda = \frac{p_\Lambda}{\rho_\Lambda c^2} = -1 \,,$$

so, not only Λ does not act as a standard physical component, but using equation 1.41, one can show that its energy density is constant in time

$$\rho_\Lambda(t) = \rho_{0,\Lambda} \,.$$

Using equation 1.19 we can rewrite the second Friedmann equation, in the case of a single-component universe, as

$$\left(\frac{\dot{a}}{a_0}\right)^2 = H_0^2 \left[\Omega_0 \left(\frac{a_0}{a}\right)^{1+3w} + (1-\Omega_0)\right] , \tag{1.42}$$

or also as

$$H(t)^2 = H_0^2 \left(\frac{a_0}{a}\right)^2 \left[\Omega_0 \left(\frac{a_0}{a}\right)^{1+3w} + (1-\Omega_0)\right] . \tag{1.43}$$

Assuming a flat Universe ($\Omega = 1$) dominated by non-relativistic matter ($w = 0$), the equation 1.43 leads to:

$$a(t) = a_0 \left(\frac{t}{t_0}\right)^{\frac{2}{3}} . \tag{1.44}$$

This model is also known as Einstein-de Sitter and, as we can notice from the above equation, represents a Universe that expands for an indefinite time.

In the ΛCDM model, the dark energy component is represented by the cosmological constant with a constant value of $w = -1$, which corresponds to a constant equation-of-state parameter $w = -1$. In this case the equation 1.43 can be rewritten as:

$$H(z)^2 = H_0^2 \Big[\Omega_{0,k}(1+z)^2 + \Omega_{0,m}(1+z)^3 + \Omega_{0,r}(1+z)^4 + \Omega_{0,\Lambda} \Big] . \quad (1.45)$$

1.8 Linear perturbations

While the cosmological principle states that the Universe is homogeneous and isotropic on large scales, observations show that it is neither homogeneous nor isotropic on smaller scales. From stars and galaxies to clusters and superclusters, cosmic structures exhibit significant density fluctuations.

Gravitational instability is the primary mechanism driving the formation of these structures.

In 1902, Jeans formulated a theory (Jeans, 1902) demonstrating that, starting with a homogeneous and isotropic fluid, small perturbations in density ($\delta\rho$) and velocity (δv) could evolve over time. His calculations revealed that such density fluctuations could grow if the influence of pressure is significantly weaker than the contribution of self-gravity, which drives the collapse.

However, in his calculations, Jeans did not take into account the expansion of the Universe, which had not been discovered yet.

The presence of a cosmic expansion significantly suppresses the growth of density fluctuations: while gravitational pull tends to induce the collapse by accreting matter in overdense regions, the same matter is being diluted by the cosmic expansion.

Starting from primordial overdensities with small amplitude, these fluctuations grew over time under the influence of gravity, eventually forming the complex cosmic structures we observe today.

Using Jeans theory, we can find analytic solutions to describe the evolution of density perturbations.

Jeans theory is valid only under the assumption of small perturbations, i.e. within the linear regime. In chapter 3, we will see how to follow the evolution of perturbations in a non-linear regime.

The core principle of Jeans theory is the concept of the Jeans scale, λ_J, which represents the threshold above which the gravitational force of a matter distribution dominates over the opposing force generated by the pressure gradient. The collapse conditions reads

$$F_g \simeq \frac{GM}{\lambda^2} \simeq \frac{G\rho\lambda^3}{\lambda^2} > F_p \simeq \frac{p\lambda^2}{\rho\lambda^3} \simeq \frac{v_s^2}{\lambda} , \quad (1.46)$$

from which it can be retrieved that the Jeans scale is

$$\lambda_J \simeq \frac{v_s}{\sqrt{G\rho}}\,.$$

Considering an expanding universe, we also have to take into account the scale of the cosmological horizon R_H. The horizon scale indicates the length under which we have causal connection, and it is defined as

$$R_H(t) = a(t)\int_0^t \frac{cdt'}{a(t')}\,. \tag{1.47}$$

On scales larger than the cosmological horizon, $\lambda > R_H$, regions of the Universe are not causally connected, as there has not been enough time for signals to travel across these distances. As a result, gravity is the dominant interaction governing the evolution of perturbations on super-horizon scales. In contrast, on sub-horizon scales, i.e. $\lambda < R_H$, microphysical processes, such as radiation pressure, become significant. These effects can oppose to the gravitational collapse, especially in the early universe when radiation is the dominant component, thereby influencing the growth rate and amplitude of density perturbations.

1.8.1 Super-horizon scales

Let us first consider the case of perturbation over the horizon scale $\lambda > R_H$. As we said we consider only gravitational interaction. We treat the perturbation as a small spherical overdense universe, $\Omega > 1$, inside a flat universe, $\Omega = 0$, which for simplicity we approximate as Einstein-de Sitter.

Applying the second Friedmann equation (1.15) to both the perturbation and the background, one gets:

$$H_b^2 = \frac{8\pi G}{3}\rho_b \quad (background) \tag{1.48a}$$

$$H_p^2 = \frac{8\pi G}{3}\rho_p - \frac{c^2}{a^2} \quad (perturbation) \tag{1.48b}$$

Given the fact that the perturbation is evolving inside the background universe, we can synchronize the two by matching their Hubble parameters, $H_b(t) = H_p(t)$. By equating the two expressions and defining the density contrast δ as

$$\delta \equiv \frac{\rho_p - \rho_b}{\rho_b} \tag{1.49}$$

we obtain that the evolution in time of the perturbation is given by

$$\delta = \frac{3c^2}{8\pi G}\frac{1}{a^2\rho_b} \propto \frac{1}{a^2}\frac{1}{\rho_b} \tag{1.50}$$

This equation tells us that the evolution of the density contrast of the perturbation at scales $\lambda > R_H$ depends on the behavior of the background density ρ_b. In particular,

$$t < t_{eq}: \quad \rho_b = \rho_r \propto a^{-4} \quad so \quad \delta \propto a^2 \tag{1.51a}$$

$$t > t_{eq}: \quad \rho_b = \rho_{DM} \propto a^{-3} \quad so \quad \delta \propto a \tag{1.51b}$$

In the case $\lambda > \lambda_H$, all the components of the universe are coupled only by the effect of gravitational interaction. In this way, the perturbations follow the behavior of the dominant component of the respective epoch, which is radiation for $t < t_{eq}$ and dark matter for $t > t_{eq}$.

$$t < t_{eq} \qquad \delta_b \propto \delta_{DM} \propto \delta_R \propto a^2 \tag{1.52a}$$

$$t > t_{eq} \qquad \delta_R \propto \delta_b \propto \delta_{DM} \propto a \tag{1.52b}$$

1.8.2 Sub-horizon scales

We will now treat, instead, the solutions in the case of perturbation within the horizon scales $\lambda < \lambda_H$.

Within the horizon scale, the evolution of perturbations is shaped by microphysical effects that influence their growth and dynamics. To analyze their behavior in this regime, we begin with the fluid dynamic equations. From these, Jeans theory provides a framework for describing the interplay of forces governing the evolution of perturbations.

The equations of motion for a perfect fluid, in the Newtonian approximation, considering the cosmic expansion, are given by

$$\frac{\partial \rho}{\partial t} + \nabla \cdot \rho \vec{u} = 0 \tag{1.53a}$$

$$\frac{\partial \vec{u}}{\partial t} + (\vec{u} \cdot \nabla)\vec{u} + \frac{1}{\rho}\nabla p + \nabla \varphi = 0 \tag{1.53b}$$

$$\nabla^2 \phi - 4\pi G \rho = 0 \tag{1.53c}$$

$$p = p(\rho, s) = p(\rho) \tag{1.53d}$$

$$\frac{\partial s}{\partial t} + \vec{u} \cdot \nabla s = 0 \tag{1.53e}$$

These are respectively the continuity equation (1.53a), the Euler equation (1.53b), the Poisson equation (1.53c), the equation of state (1.53d) and the condition of adiabatic fluctuations (1.53e). In these equations, ρ represents the density of the fluid, $\boldsymbol{u}$ the total velocity [1], p the pressure, ϕ the gravitational potential, and s the entropy. The last equation (1.53e) leads to a fluid whose equation of state depends only on pressure and density. In this way, the pressure p can be expressed as a function of ρ only, and we can consider the system composed by only the first four equations.

[1] we call u the total velocity and v the peculiar one

The fundamental idea in Jeans theory is to start from a solution (background) which satisfies the equations above and add a small linear perturbation.

Here we consider r, x as the physical and comoving distances

$$r = ax \tag{1.54}$$

If we want to derive the total velocity we obtain

$$u = Hr + v \tag{1.55}$$

where the peculiar velocity v has been defined as

$$v = a\dot{x} \tag{1.56}$$

In this way, the background velocity corresponds to the Hubble flow Hr, while the small perturbation is given by the peculiar velocity v, leading to the following system of equations:

$$\rho = \rho_b + \delta\rho \tag{1.57a}$$
$$\boldsymbol{u} = H\boldsymbol{r} + \boldsymbol{v} \tag{1.57b}$$
$$\phi = \phi_b + \delta\phi \tag{1.57c}$$
$$p = p_b + \delta p \tag{1.57d}$$

Introducing this perturbed solution into the system of equations 1.53 and neglecting terms of higher order, we obtain the following system of equations:

$$\left.\frac{\partial}{\partial t}\right|_r \delta\rho + \rho_b \nabla_r \delta v + 3Hr\nabla_r\delta\rho = 0 \tag{1.58a}$$
$$\left.\frac{\partial}{\partial t}\right|_r \delta v + H\delta v + Hr\nabla_r\delta v = -\frac{v_s^2}{\rho_b}\nabla_r\delta\rho - \nabla_r\delta\phi \tag{1.58b}$$
$$\nabla_r^2\delta\Phi = 4\pi G\delta\rho \tag{1.58c}$$

where $\left.\frac{\partial}{\partial t}\right|_r$ and ∇_r are referred to the proper coordinate frame. Moving to comoving frame, the system becomes

$$\left.\frac{\partial}{\partial t}\right|_x \delta\rho + \frac{\rho_b}{a}\nabla_x\delta v + 3H\delta\rho = 0 \tag{1.59a}$$
$$\left.\frac{\partial}{\partial t}\right|_x \delta v + H\delta v = -\frac{1}{a}v_s^2\nabla_x\delta - \frac{1}{a}\nabla_x\delta\phi \tag{1.59b}$$
$$\frac{1}{a^2}\nabla_x^2\delta\Phi = 4\pi G\delta\rho \tag{1.59c}$$

where we defined $\delta = \delta\rho/\rho_b$.

To solve the system of equations we move to Fourier space considering solutions in the form of plane waves

$$\delta f(\boldsymbol{x}, t) = \delta f_k(t) exp(i\boldsymbol{k} \cdot \boldsymbol{x}) \tag{1.60}$$

in this way the system can be rewritten as

$$\delta_k + \frac{ik\delta v_k}{a} = 0 \tag{1.61}$$

$$\delta\dot{v}_k + \frac{\dot{a}}{a}\delta v_k = -\frac{ik}{a}\left[v_s^2\delta_k + \delta\Phi_k\right] \tag{1.62}$$

$$\delta\Phi_k = -\frac{4\pi G\rho_b\delta_k a^2}{k^2} \tag{1.63}$$

Splitting the velocity field in a parallel and perpendicular component with respect to the $\boldsymbol{k}$ direction as $\boldsymbol{v}_k = \boldsymbol{v}_{k,\parallel} + \boldsymbol{v}_{k,\perp}$ the perpendicular component of the Euler equation decrease with time, $\delta_{k,\perp} \propto a^{-1}$ so we will neglect it.

Finally, combining all three equations, we obtain that the growth of linear matter density perturbation at sub-horizon scales in comoving coordinates reads

$$\ddot{\delta}_k + 2H\dot{\delta}_k + k^2\frac{v_s^2}{a^2}\delta_k = 4\pi G\rho_b\delta_k \tag{1.64}$$

while, in physical coordinates it reads

$$\ddot{\delta}_k + 2H\dot{\delta}_k + v_s^2k^2\delta_m = 4\pi G\rho_b\delta_b \tag{1.65}$$

where $\ddot{\delta}_k$ represents the acceleration of the perturbation growth, $2H\dot{\delta}_k$ is the expansion term that slows down the perturbation growth, the term $v_s^2k^2\delta_k$ indicates the dissipation due to velocity, and $4\pi G\rho_b\delta_k$ represents the gravitational contribution to the perturbation growth.

For $t > t_{eq}$, the universe is matter-dominated, behaving like an Einstein-de Sitter model (section 1.7). In this case the equation 1.65 becomes the following

$$\ddot{\delta}_k + \frac{4}{3}\frac{\dot{\delta}_k}{t} + \frac{2}{3}\frac{\delta_k}{t^2}\left(\frac{k^2v_s^2}{4\pi G\rho_b} - 1\right) = 0 \tag{1.66}$$

To study the growth of density perturbations in the early universe, we consider solutions to the perturbation equations in the form of a power law in time, $\delta_k \propto t^\alpha$, obtaining the following dispersion relation:

$$3\alpha^2 + \alpha + 2\left[\frac{k^2v_s^2}{4\pi G\rho_b} - 1\right] = 0 \tag{1.67}$$

This is a quadratic equation in α, which means that it admits two solutions. By setting the discriminant $\Delta = 0$ we find the characteristic length

$$\lambda_J = \frac{v_s}{5}\sqrt{\frac{24\pi}{G\rho_b}} \tag{1.68}$$

which is called Jeans length. This length marks the threshold between gravitational collapse and pressure-supported oscillations.

For scales under the Jeans scale, $\lambda < \lambda_J$, the equation 1.67 has discriminant $\Delta < 0$, leading to two imaginary solutions. Physically, this means that perturbations do not grow but instead oscillate as sound waves. Since these modes do not contribute to structure formation, they can be neglected when studying the growth of cosmic structures.

For scales above the Jeans scale, $\lambda > \lambda_J$, the determinant $\Delta > 0$ so the equation 1.67 presents two real solutions defined by

$$\alpha_{1,2} = \frac{-1 \pm 5\sqrt{1 - \left(\frac{\lambda_J}{\lambda}\right)^2}}{6} \tag{1.69}$$

Assuming for simplicity scales way larger than Jeans length, $\lambda \gg \lambda_J$, then $\alpha_{1,2} \simeq \frac{-1 \pm 5}{6}$ leading to the following solutions:

$$\begin{aligned} \delta_- &\propto t^{-1} \propto a^{-3/2} \\ \delta_+ &\propto t^{2/3} \propto a \end{aligned} \tag{1.70}$$

The decaying solution δ_- rapidly becomes negligible as the universe expands. Since structure formation relies on the amplification of perturbations over time, the only physically relevant solution is the growing mode δ_+.

The above solution applies to all non-relativistic matter (baryons and CDM) once they decouple from radiation. However, the behavior of perturbations differs significantly before and after matter-radiation equality(t_{eq}).

It can be shown that in a radiation-dominated universe, radiation perturbations are not able to grow inside the horizon because radiation pressure (from relativistic particles) opposes to gravitational collapse. So for $t < t_{eq}$ radiation perturbations do not grow within the horizon and, given that baryonic matter is still coupled with radiation, neither baryonic perturbations are able to grow.

Unlike baryons, dark matter is collisionless and decoupled from radiation early on. Let us study the case of DM fluctuation inside the horizon at $t < t_{eq}$. Equation 1.65 can be written as

$$\ddot{\delta}_{DM} + 2H\dot{\delta}_{DM} - 4\pi G\rho_{b,DM} = 0 \tag{1.71}$$

where we wrote for simplicity $\delta_{k,DM} = \delta_{DM}$ and we neglected the dissipation term $k^2 v_s^2 \delta_{DM}$ assuming scales way bigger than the Jeans scale.

Solving this equation one can find that the growth of DM perturbation inside the horizon for $t < t_{eq}$ is described by

$$\delta_{DM} = 1 + 3\frac{a}{a_{eq}} \quad with \quad a < a_{eq} \tag{1.72}$$

This equation indicates a logarithmic growth of dark-matter perturbation during the radiation-dominated epoch, much slower than the $\delta \propto a$ growth in the

matter-dominated epoch. The cosmic horizon expands with time, meaning that progressively larger scales enter the horizon as time increases.

The fate of a DM perturbation depends on when it crosses the horizon:

- $t < t_{eq}$: Once inside the horizon, their growth is severely limited according to equation 1.72. By t_{eq}, they have grown by at most a factor of 5/2, this heavily suppression is called the Meszaros effect
- $t > t_{eq}$: They remains outside the horizon durin the readiation-domination epoch, continuing to grows as $\delta \propto \alpha^2$ until t_{eq}

Only after the equivalence, when the Universe passes from radiation-dominated to matter-dominated, the dark-matter perturbations inside the horizon continue to grow as $\delta \propto a$.

While DM perturbations restart to grow right after t_{eq}, baryonic matter remains coupled to radiation until they decouple at later times.

When baryonic matter finally decouples from radiation, dark matter has already formed shallow potential wells during the radiation era (due to its earlier decoupling). For this reason, baryonic perturbations do not evolve freely but instead fall into the preexisting DM halos. This rapid growth of baryonic perturbation is called baryon catch-up and is described by

$$\delta_b \propto \delta_{DM}\left(1 - \frac{a_{dec}}{a}\right) \tag{1.73}$$

1.9 Statistical properties of Clustering

In this section, we introduce the foundational methods used to quantify the clustering of matter in the Universe, focusing in particular on the two-point correlation function and the power spectrum. Together, these statistical measures are fundamental to connect theoretical models of structure formation with observational data, enabling precise constraints on cosmological parameters and the underlying physics of the Universe.

We already saw how gravitational instability is the main driving force leading to the formation of structures in the universe. To accurately analyze gravitational instability, we must develop statistical methods that can set the initial conditions to the gravitation instability equation and validate theoretical models by comparing them with observed galaxy distributions at large scales.

Density perturbations are believed to originate from quantum fluctuations stretched during the final stages of inflation, resulting in nearly Gaussian stochastic distributions, as confirmed by Planck measurements showing negligible deviations from Gaussianity in the CMB anisotropies (Akrami et al., 2019). For this reason we can define the density fluctuation $\delta(\vec{x})$

$$\delta(\mathbf{x}) = \frac{\rho(\mathbf{x}) - \bar{\rho}}{\bar{\rho}} \tag{1.74}$$

as a random field, whose probability is set by a Gaussian statistical distribution

$$p(\delta) = \frac{1}{\sqrt{2\pi}\sigma(t)} \exp\left\{-\frac{1}{2}\left[\frac{\delta}{\sigma(t)}\right]^2\right\} \tag{1.75}$$

with a zero mean $\langle\delta\rangle = 0$, to ensure that the universe is homogeneous and isotropic, and variance $\sigma^2(t) = \langle\delta^2\rangle$.

According to the ergodic hypothesis, each realization of a stochastic process, as long as constituted by a sufficiently large amount of data, becomes representative of the whole ensemble statistical properties. Therefore, it is possible to construct, formally, a 'realization' of the Universe by dividing it into cubic cells of volume V with periodic boundary conditions at the faces of each cube.

In Section 1.8, we analyzed the linear evolution of density perturbations by representing them as plane waves characterized by a wavevector $\boldsymbol{k}$. This approach is particularly effective because, according to the Fourier decomposition theorem, any general perturbation can be expressed as a sum of these plane wave modes, which evolve independently from one another as long as the evolution remains in the linear regime.

This allows us to write the following relation for the density fluctuation:

$$\delta(\mathbf{x}) = \int \frac{d^3k}{(2\pi)^3}\delta_k e^{i\mathbf{k}\cdot\mathbf{x}} \tag{1.76}$$

where $\mathbf{k}$ is the comoving wavenumber and $\mathbf{x}$ the comoving coordinate.

Given two points in space at positions $\mathbf{x}, \mathbf{x}+\mathbf{r}$ we can define the correlation function as

$$\xi(|\mathbf{r}|) = \langle\delta(\mathbf{x})\delta(\mathbf{x}+\mathbf{r})\rangle \tag{1.77}$$

Using equation 1.76 the correlation function can be written in Fourier space

$$\xi(r) = \int \frac{d^3k}{8\pi^3}\int \frac{d^3k'}{8\pi^3}\langle\delta_k\delta_{k'}\rangle e^{i(\mathbf{k}+\mathbf{k}')\cdot\mathbf{x}} e^{i\mathbf{k}\cdot\mathbf{r}} \tag{1.78}$$

where we called

$$\begin{aligned}\delta(\mathbf{x}) &= \int \frac{d^3k'}{(2\pi)^3}\delta_{k'} e^{i\mathbf{k}'\cdot\mathbf{x}} \\ \delta(\mathbf{x}+\mathbf{r}) &= \int \frac{d^3k}{(2\pi)^3}\delta_k e^{i\mathbf{k}\cdot\mathbf{x}}\end{aligned} \tag{1.79}$$

The power spectrum $P(k)$ can be defined using the relation

$$\langle\delta_k\delta_{k'}\rangle = (2\pi)^3\delta_D(\mathbf{k}+\mathbf{k}')P(k) \tag{1.80}$$

where $\delta_D(\mathbf{k}+\mathbf{k}')$ is the Dirac delta. Substituting equation 1.80 inside 1.78 we obtain the following relations between the Power spectrum $P(k)$ and the correlation function $\xi(r)$

$$\xi(r) = \frac{1}{(2\pi)^3}\int d^3k\, P(k) e^{i\mathbf{k}\cdot\mathbf{r}} \tag{1.81}$$

The Power spectrum determines the importance of a fluctuation with wavenumber k, in fact we can notice that for $\mathbf{k} = -\mathbf{k}'$ we have $P(k) \propto \langle|\delta(\mathbf{k})|^2\rangle$. Precisely the power spectrum P(k) represents a power density while the power is the integral of P(k) on the Fourier space volume $\int P(k)d^3k$. For this reason P(k) depends only on amplitude of k (and not $\mathbf{k}$).

Since $\xi(r)$ only depends on distance r, we can use spherical coordinates $,\int d^3k = \int dk_x \int dk_y \int dk_z = \int_0^{2\pi}\int_0^{\pi} sin\theta d\theta \int_0^{\infty} k^2 dk$ obtaining, for $k = -k'$

$$\langle|\delta(x)|^2\rangle = (2\pi)^3 P(k)\,\delta_D^{(3)}(0) = P(k)V_\infty \tag{1.82}$$

where V_∞ is the volume of the universe.

We can define the variance σ^2 of the density field as

$$\sigma^2 = \langle|\delta(x)|\rangle \tag{1.83}$$

If we divide the universe in independent samples, each large enough to be considered representative, we can compute the variance σ^2 through a double average: the average on all volumes of the spatial quadratic average of δ

$$\sigma^2 = \frac{1}{V}\int \langle\delta^2(x)\rangle d^3x \tag{1.84}$$

Using the Parseval theorem [2] the latter relation becomes

$$\sigma^2 = \frac{1}{(2\pi)^3}\int_{-\infty}^{\infty} P(k)d^3k \tag{1.85}$$

which indicates that the covariance is just the integral of the power spectrum on the whole Fourier space. Passing to spherical coordinates, equation 1.85 can be written as

$$\sigma^2 = \frac{1}{2\pi^2}\int_0^{\infty} k^2 P(k)dk \tag{1.86}$$

Actually, what we found is valid for a punctual variance, but in real situations we use average quantities such as the density within a given volume, so what we calculate is not a punctual variance but a filtered one.

We can define the filtered density field as

$$\delta_M(\mathbf{x}) = \delta(\mathbf{x}) * W(\mathbf{x}, R) \tag{1.87}$$

where $W(\mathbf{x}, R)$ is the filter function. A commonly used filter is the top-hat filter, which is centered at position $\boldsymbol{x}$ and has a radius R. The corresponding filter function W is constant within the sphere of radius R, and zero outside.

The convolution operation does not change the distribution property meaning that also δ_M is a Gaussian distribution.

[2] According to Parseval Thorem the integral on the whole range x $(-\infty, +\infty)$ of the product of two functions is equal to the integral on the infinite Fourier space of the transformed quantity times a factor $1/2\pi$

Using the convolution property in Fourier space we can finally define the mass variance as

$$\sigma_M = \frac{1}{(2\pi)^3} \int_{-\infty}^{\infty} P(K)\hat{W}^2(k,R)d^3\mathbf{k} \tag{1.88}$$

It is interesting to notice that as $R \to 0$, the mass variance $\sigma_M^2 \to \sigma$, meaning that when the filter radius tends to 0 we increase the precision (i.e. we are able to probe smaller and smaller regions) and the mass variance tends to coincide to the punctual one. Conversely, as $R \to \infty$, the variance $\sigma_M^2 \to 0$ which is expected since when filtering the whole space, the density contrast δ would have zero mean. By convention the filtering radius is set at $R = 8\,Mpc\,h^{-1}$, defining σ_8 as:

$$\sigma_8 = \frac{1}{(2\pi)^3} \int_{-\infty}^{\infty} P(K)\hat{W}^2(k,R = 8Mpc\,h^{-1})d^3\mathbf{k} \tag{1.89}$$

1.9.1 Power Spectrum

At the end of inflation, the oscillations of the inflaton field generate primordial density fluctuations, which provide the initial conditions for the later formation of cosmic structures. Inflation is a period of extremely rapid and nearly uniform exponential expansion, meaning that space expands at almost the same rate everywhere with negligible variations. This near-uniformity ensures that inflation does not introduce any preferred physical scale (no particular size or distance is favored over another). As a result, the statistical properties of the primordial fluctuations must be scale-invariant, meaning that they have the same amplitude across all observable scales, a prediction that aligns with observations of the cosmic microwave background (Akrami et al., 2019). This is reflected assuming a power spectrum in a power law form

$$P(k) = Ak^n \tag{1.90}$$

where A is the amplitude of the power spectrum and n the spectral index.

We have seen that density field fluctuations, which form with a primordial amplitude $\delta = \delta(x, t_i)$ at initial time t_i grow over time according to the growing solution of the dispersion relation. This means that at a later time $t > t_i$, the fluctuations evolve as $\delta(t) = \delta_+(t)$. Since this solution is solely a function of time, it does not introduce any dependence on scale. This statement holds as long as we consider scales significantly larger than the Jeans scale $\lambda \gg \lambda_J$ where gravitational interaction is the dominant force. In such a regime, all perturbations grow in the same way across all scales.

Now, if we assume that the initial power spectrum follows the form $P(k, t_i) = P_i \propto \delta_i^2$, at a given time $t > t_i$ the power spectrum evolves, in an EdS model, as

$$P(k,t) \propto \delta_i^2\, \delta_+^2(t) \tag{1.91}$$

With these assumptions, the mass variance

$$\sigma_M^2 \propto \delta_+^2(t) \int P_i d^3k \propto \delta_+^2(t) \int A k^n d^3k \propto \delta_+^2(t) k^{n+3} \propto \delta_+^2(t) M^{-\frac{n+3}{3}} \quad (1.92)$$

So far we assumed the validity of the linear approximation, which is valid in the limit $|\delta| < 1$, $\sigma^2 < 1$. To check the limit of our approximation we can define the mass M_* at which we lose linearity as $\sigma_M^2(M_*) \sim 1$ leading to

$$M_*(t) \propto \delta_+^{\frac{6}{n+3}} \quad (1.93)$$

As we saw in chapter 1.8 the horizon scale has an impact on the evolution of perturbation growth and so on the power spectrum.

Assuming the universe as an EdS model, the increase of horizon radius is given by

$$R_H \propto \begin{cases} a^2 & (a < a_{eq}) \\ a^{3/2} & (a > a_{eq}) \end{cases} \quad (1.94)$$

while the growth factor

$$\delta_+ \propto \begin{cases} a^2 & (a < a_{eq}) \\ a & (a > a_{eq}) \end{cases} \quad (1.95)$$

If we consider a perturbation entering the horizon before the equivalence $a_H < a_{eq}$, where we called a_H the time at which the perturbation enters the horizon, the growth of density fluctuations is significantly suppressed. This suppression occurs because the dominant radiation component exerts substantial pressure, counteracting the gravitational collapse that would otherwise amplify perturbations. The growth of such perturbations can be described by the relation:

$$\delta(k, t_{eq}) = \delta(k, t_i) \left(\frac{a_H}{a_i} \right)^2 \propto \delta(k, t_i)\, a_H^2 \quad (1.96)$$

which states that the power spectrum gets modified by a factor a_H^2. Smaller-scale perturbations (larger k) enter the horizon earlier, this relationship implies that $a_H \propto k^{-1}$, allowing us to rewrite the density contrast as: $\delta(k, t_{eq}) \propto \delta(k, t_i) k^{-2}$

and, since the power spectrum is proportional to the square of density contrast, it follows that:

$$P(k, t_{eq}) \propto P_i\, k^{-4} \quad (1.97)$$

The steep k^{-4} dependence implies a strong suppression of power on small scales, as a consequence of the Meszaros effect described in section 1.8, whereby perturbations that enter the horizon during the radiation-dominated era undergo minimal growth due to the opposing influence of radiation pressure counteracting gravitational collapse. Consequently, these small-scale modes contribute less to the overall structure formation, as their power spectrum falls

off rapidly for $k > k_{eq}$, where k_{eq} corresponds the scale of the cosmological horizon at t_{eq}.

In contrast, perturbations that enter the horizon after matter-radiation equality, corresponding to scales with $a_H > a_{eq}$, evolve under very different conditions. By this epoch, the universe has transitioned to matter domination, and the absence of significant pressure support allows perturbations to grow unimpeded by radiation effects. The growth of these perturbations is described by:

$$\delta(k, t_{eq}) = \delta(k, t_i)\left(\frac{a_{eq}}{a_i}\right)^2 \propto \delta(k, t_i) \tag{1.98}$$

Here, the growth factor depends only on the ratio of the scale factors and is independent on k. This means that the shape of thr primordial power spectrum is preserved:

$$P(k, t_{eq}) \propto P_i(k) \tag{1.99}$$

As a result, the power spectrum exhibits a peak at k_{eq}, corresponding to the scale that entered the horizon at matter-radiation equivalence.

In general we can link the initial power spectrum to the one at equivalence defining a transfer function $T(k)$ as

$$P(k, t_{eq}) = P(k, t_i)\, T^2(k) \tag{1.100}$$

where the transfer function accounts for the different perturbation evolution between large scales (small k) and small scales (large k).

Since dark matter is collisionless, we cannot speak of a true dissipation in its perturbations. However, once dark matter decouples from radiation (well before t_{eq}), its particles begin to propagate freely, interacting only gravitationally and moving from regions of higher density to lower density. This phenomenon, known as free streaming, determines the free-streaming scale λ_{FS} as the scale below which dark matter perturbations are smoothed out.

The free-streaming scale strongly depends on the Dark Matter nature. In Hot Dark Matter scenario (HDM) the dark matter particles are light particles which decouple from radiation when they are still relativistic. This implies a larger free-streaming mass $M_{FS} \sim 10^{16} M_\odot$ with respect to Cold Darm Matter (CDM) case, for which instead $M_{FS} \sim 10^{5-6} M_\odot$. This implies that in the case of Hot Dark Matter (HDM), small-scale perturbations are suppressed, causing structure formation to begin on large scales first, a so-called top-down scenario. In contrast, Cold Dark Matter (CDM) allows small-scale perturbations to grow first, leading to a hierarchical formation process known as a bottom-up scenario.

In figure 1.1 we can better see how in CDM-dominated universe most of the power reside in smaller scales while for HDM-dominated universe the opposite occurs. The WDM curve represents a Warm Dark Matter model which is a hypothetical form of dark matter composed of particles with masses and

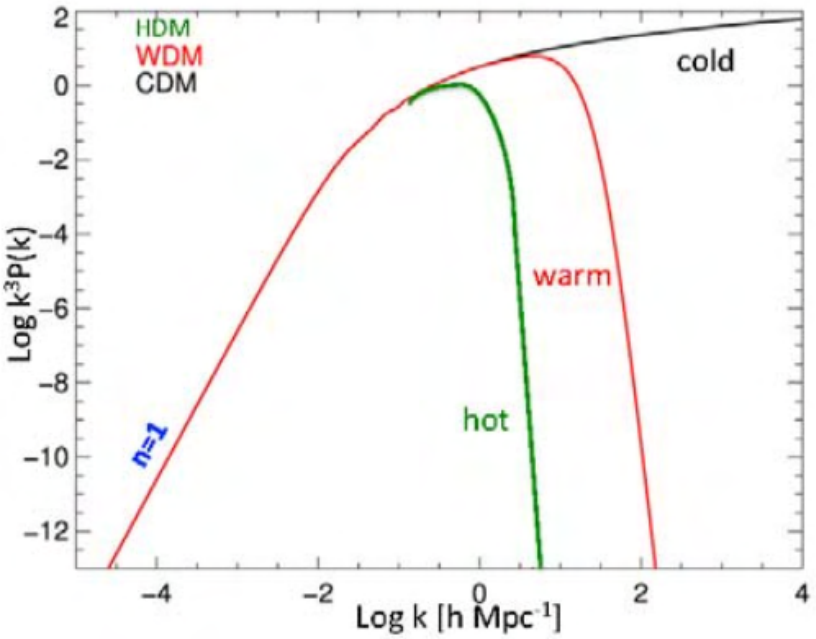

Figure 1.1: Late time linear power spectra in universe dominated by hot,warm and cold dark matter presented in Frenk and White (2012). The y-axis gives the total power density per decade in spatial frequency k.

thermal velocities intermediate between those of Cold Dark Matter (CDM) and Hot Dark Matter (HDM).

Current observations align well with the hierarchical merging of structures of CDM scenario (Frenk and White, 2012), for which the transfer function is represented by

$$T(k) \propto \begin{cases} k^0 & for \quad k < k_{eq} \\ k^{-2} & for \quad k > k_{eq} \end{cases} \tag{1.101}$$

Later in time, as density fluctuations approach unity in amplitude, they transition into the non-linear regime, where linear approximations are no longer valid for describing their growth.

1.10 Gravitational Lensing

Gravitational lensing is a powerful tool in modern cosmology, offering a unique method for probing the distribution of matter in the universe, including both visible and dark matter (Weinberg, 2008; Bartelmann and Schneider, 2001). This phenomenon arises from the deflection of light by gravitational fields, as predicted by Einstein's theory of General Relativity (Congdon and Keeton, 2018). When light from distant galaxies passes near massive objects, such as

galaxy clusters or large-scale structures, its trajectory is bent, leading to distortions in the observed images of background sources. Gravitational lensing is typically categorized into two regimes (Weinberg, 2008):

- **Strong Lensing**: Produces dramatic effects such as multiple images, arcs, or Einstein rings. It occurs when the lensing mass is very dense and it can provide detailed information about the mass distribution of the lens.
- **Weak Lensing**: Involves subtle distortions in the shapes of background galaxies, typically by large-scale structures. Although the individual distortions are small, statistical analysis over large galaxy samples enables the reconstruction of the underlying matter distribution, including dark matter.

To model the trajectories of light rays in a cosmological context, we make several simplifying assumptions. First, we assume that the geometry of the space-time is well described by the FLRW metric (see section 1.2).

We then adopt the Born approximation, which assumes that the perturbations of the light rays are sufficiently weak, allowing the deflection to be calculated along the unperturbed, straight path.

Third, we assume the gravitational potential Φ of the lens to be weak, $|\Phi^2| \ll c^2$, allowing it to be treated within the Newtonian approximation. Under these conditions, the deflection angle $\hat{\alpha}$ can be expresses as (Coles and Lucchin, 2002):

$$\hat{\alpha} = \frac{2}{c^2} \int \nabla_{\perp} \Phi dl \tag{1.102}$$

where the integral is taken along the photon's trajectory, and $\nabla_{\perp}\Phi$ denotes the gradient of the Newtonian potential perpendicular to the light path. We consider only $\nabla_{\perp}\Phi$ because only the perpendicular component of the gravitational potential gradient affects the direction of the light ray.

Considering the potential of a point-like lens with impact parameter b, i.e. the perpendicular distance between the light path and the lens, and distance along the ray's trajectory z, we can write the potential of the lens as

$$\Phi(b, z) = -\frac{GM}{\sqrt{b^2 + z^2}} \tag{1.103}$$

which, when substituted into the deflection angle equation, yields:

$$\nabla_{\perp}\Phi(b.z) = \frac{GMb}{(b^2 + z^2)^{3/2}} \tag{1.104}$$

By replacing the latter in equation 1.102, we obtain the following relation:

$$\hat{\alpha} = \frac{2}{c^2} \int \nabla_{\perp} \Phi dz = \frac{4GM}{c^2 b} \tag{1.105}$$

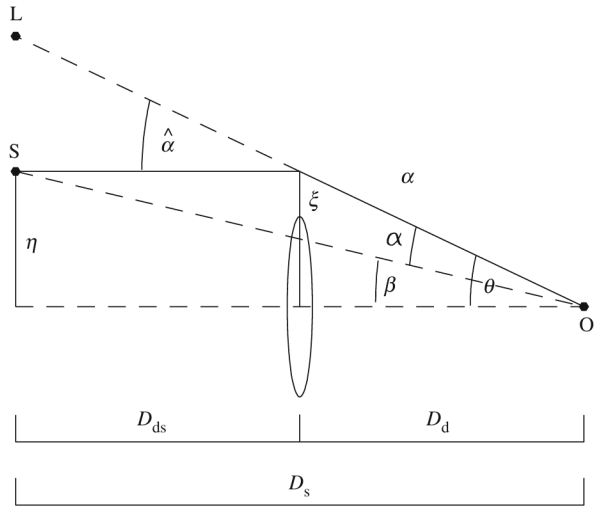

Figure 1.2: Picture from Coles and Lucchin (2002) which describes the gravitational lensing of a photon traveling from source S to the observer O. The photon is deflected by an angle $\hat{\alpha}$, the angular separation os the source S and image L from the optic axis are β and θ respectively.

In the weak lensing regime, the lens can be approximated as a thin mass layer characterized by its surface density Σ, which can be written as the integral of the matter density along the photon path

$$\Sigma(\boldsymbol{\xi}) = \int \rho(\boldsymbol{\xi}, z) dz \tag{1.106}$$

The total deflection angle is then a superposition of the contributions of all the mass elements in the lens plane (Bartelmann and Schneider, 2001):

$$\hat{\boldsymbol{\alpha}}(\boldsymbol{\xi}) = \frac{4G}{c^2} \int \frac{(\boldsymbol{\xi} - \boldsymbol{\xi}')\Sigma(\boldsymbol{\xi}')}{|\boldsymbol{\xi} - \boldsymbol{\xi}'|} d^2\boldsymbol{\xi}' \tag{1.107}$$

In other words, the deflection is a vector sum of contributions from all mass elements in the lens plane, weighted by their distance from the light ray.

If we assume that the lens has circular symmetry, the deflection angle always points toward the center of mass, and its magnitude depends only on the enclosed mass

$$M(\xi) = 2\pi \int_0^{\xi} \Sigma(\xi')\xi' d\xi' \tag{1.108}$$

allowing us to write

$$\hat{\alpha}(\xi) = \frac{4GM(\xi)}{c^2 \xi} \tag{1.109}$$

Considering the geometry in figure 1.2, we can introduce the reduced deflection angle α as

$$\boldsymbol{\alpha} = \frac{D_{ds}}{D_s} \hat{\boldsymbol{\alpha}} \tag{1.110}$$

Assuming $\beta, \theta, \hat{\alpha}$ to be small angles we get

$$\theta D_s = \beta D_s - \hat{\alpha} D_{ds} \tag{1.111}$$

from which, by employing equation 1.110, we obtain

$$\boldsymbol{\beta} = \boldsymbol{\theta} - \boldsymbol{\alpha} \tag{1.112}$$

This equation is called the lens equation and relates the angular position of the image (θ) to the angular position of the source (β).

To generalize beyond spherical symmetry, we can simplify the mathematical description of gravitational lensing by defining the scaled potential, also known as lensing potential, $\psi(\theta)$ with the following relation:

$$\psi(\theta) = \frac{1}{D}\frac{2}{c^2}\int \Phi(D_d\boldsymbol{\theta}, z)dz \tag{1.113}$$

While the gravitational potential Φ is a 3D function, the scaled potential ψ represents the projection of the 3D potential onto the 2D plane.

Having defined the scaled potential ψ, the gradient of ψ with respect to θ is precisely the deflection angle (Coles and Lucchin, 2002)

$$\nabla_\theta \psi = D_d \nabla_\xi \psi = \frac{2}{c^2}\frac{D_d s}{D_s}\int \nabla_\perp \Phi dz = \boldsymbol{\alpha} \tag{1.114}$$

where, as shown in figure 1.2, for small angles $\xi = D_d\theta$.

If we compute the Laplacian of the scaled potential, we obtain

$$\nabla^2_\theta \psi = \frac{2}{c^2}\frac{D_d D_{ds}}{D_s}\int \nabla^2_\xi \Phi dz = \frac{2}{c^2}\frac{D_d D_{ds}}{D_s} 4\pi G\Sigma = 2\frac{\Sigma}{\Sigma_*} \tag{1.115}$$

in which we used the Poisson equation $\nabla^2\Phi = 4\pi G\rho$, and we defined a critical surface density $\Sigma_* \equiv \frac{c^2}{4\pi G}\frac{D_s}{D_d D_{ds}}$.

Therefore, we can define the convergence κ as:

$$\kappa(\theta) \equiv \frac{\Sigma(\theta)}{\Sigma_*} \tag{1.116}$$

Combining equation 1.115 and the definition of the convergence κ in equation 1.116, We obtain a two-dimensional analogue of the Poisson equation (Coles and Lucchin, 2002)

$$\nabla^2_\theta \psi = 2k(\theta) \tag{1.117}$$

This relation highlights the direct link between the lensing potential and the surface mass density projected along the line of sight.

The critical surface density Σ_* serves as a threshold: if the local surface mass density Σ satisfies $\kappa = \Sigma/\Sigma_* \geq 1$, the lensing potential is strong enough to produce multiple images of the same background source.

According to the lens equation (1.112), if this equation admits more than one solution for a fixed source position β, then the observer detects multiple images at different angular positions θ (Bartelmann and Schneider, 2001; Congdon and Keeton, 2018).

This defines the strong lensing regime. In contrast, if $k < 1$, the lensing can be classified as weak and produces only small, single-image distortions.

Equation 1.117 admits as a general solution (Coles and Lucchin, 2002; Bartelmann and Schneider, 2001):

$$\psi(\boldsymbol{\theta}) = \frac{1}{\pi} \int \kappa(\boldsymbol{\theta}) log(|\boldsymbol{\theta} - \boldsymbol{\theta'}|) d^2\boldsymbol{\theta'} \tag{1.118}$$

From this, using the gradient of the potential as defined in equation 1.114, we obtain the deflection:

$$\boldsymbol{\alpha}(\boldsymbol{\theta}) = \frac{1}{\pi} \int \kappa(\boldsymbol{\theta}) \frac{\boldsymbol{\theta} - \boldsymbol{\theta'}}{|\boldsymbol{\theta} - \boldsymbol{\theta'}|^2} d^2\theta' \tag{1.119}$$

In general, the lens produces a mapping of the source plane onto the image plane. The local properties of this mapping are best specified by the Jacobian matrix (Coles and Lucchin, 2002)

$$\boldsymbol{A}_{ij} = \frac{\partial \beta_i}{\partial \theta_j} = \left(\delta_{ij} - \frac{\partial \alpha_i(\boldsymbol{\theta})}{\partial \theta_j} \right) = \left(\delta_{ij} - \frac{\partial^2 \psi}{\partial \theta_i \partial \theta_j} \right) \tag{1.120}$$

Defining the notation

$$\psi_{ij} \equiv \frac{\partial^2 \psi}{\partial \theta_i \partial \theta_j} \tag{1.121}$$

equation 1.117 brings to

$$k = \frac{1}{2}(\psi_{11} + \psi_{22}) \tag{1.122}$$

Using the elements of ψ_{ij} we can construct the components of a shear tensor

$$\begin{aligned} \gamma_1 &= \frac{1}{2}(\psi_{11} - \psi_{22}) \equiv \gamma cos(2\phi) \\ \gamma_2 &= \psi_{12} = \psi_{21}) \equiv \gamma sin(2\phi) \end{aligned} \tag{1.123}$$

Using these terms we can write the distortion matrix as

$$A = \begin{pmatrix} 1 - \kappa - \gamma_1 & -\gamma_2 \\ -\gamma_2 & 1 - \kappa + \gamma_1 \end{pmatrix} \tag{1.124}$$

which can be rewritten as

$$A = (1 - \kappa) \begin{pmatrix} 1 & 0 \\ 0 & 1 \end{pmatrix} - \gamma \begin{pmatrix} cos2\phi & sin2\phi \\ sin2\phi & -cos2\phi \end{pmatrix} \tag{1.125}$$

where we used $\gamma = \sqrt{\gamma_1^2 + \gamma_2^2}$. This notation is useful because it allows a simple visual interpretation of the effects of lensing. A pure convergence k

corresponds to an isotropic magnification of the source in such a way that a circular source becomes a larger, or smaller, but still circular image. The components γ_1 and γ_2 of the shear are represented in such a way that γ is the magnitude of the shear and ϕ its orientation. A non-zero shear transforms a circular source into an elliptical image.

1.10.1 Weak Lensing Observables

The ability of a gravitational lens to produce multiple images depends on its effective "strength," commonly quantified by the dimensionless convergence κ. While the classification into weak and strong lensing is a useful simplification, it is not a fundamental distinction as both phenomena arise from the same underlying physics (Normann et al., 2024). Nonetheless, from a mathematical standpoint, multiple imaging occurs when $k > 1$, corresponding to surface mass densities exceeding the critical threshold Σ_*.

In contrast, the weak lensing regime is defined by $k \ll 1$, where the lensing mass is insufficient to generate multiple images. Instead, it induces small but coherent distortions in the shapes of background galaxies, typically at the percent level. These subtle effects cannot be inferred from individual sources but emerge statistically across large samples of galaxies (Bartelmann and Schneider, 2001). Weak gravitational lensing thus serves as a powerful probe of the large-scale matter distribution in the universe. Measuring shear patterns over wide sky areas, enables the reconstruction of the projected mass density, tracing both luminous and dark matter structures.

Statistical analyses across wide fields of view, enabled by deep galaxy surveys and high-resolution imaging (Abbott et al., 2022; Heymans et al., 2021), have provided constraints on key cosmological parameters, including:

- The matter density parameter Ω_m
- The amplitude of matter fluctuations encoded in S_8
- Dark energy properties through redshift evolution of lensing signals

Furthermore, weak lensing tomography, combining shear measurements across multiple redshift bins, offers a powerful means of mapping the growth of structure over cosmic time. This makes weak lensing a uniquely sensitive tool for testing theories of gravity and distinguishing between dark energy models and modifications to General Relativity.

1.11 Observational contrains and ΛCDM model

The discovery of the accelerated expansion of the universe, primarily through observations of Type Ia supernovae (SNe Ia), marked a turning point in cosmology. This discovery, later corroborated by measurements of the Cosmic

Microwave Background (CMB) and large-scale structure, revealed that the universe is dominated by a mysterious form of energy known as dark energy. The standard cosmological framework, known as the ΛCDM model, incorporates both a cosmological constant Λ (as a form of dark energy) and cold dark matter (CDM) to describe the evolution of the Universe. While Λ successfully accounts for a wide range of cosmological observations, significant theoretical and observational tensions persist. This section outlines the key observational pillars supporting the ΛCDM model and introduces the central problems that challenge its completeness. These unresolved issues motivate the investigation of alternative dark energy models, which will be the focus of the next chapters.

CMB and BAO

The cosmic microwave background (CMB) anisotropies contain valuable information of the early universe, capturing conditions before cosmic structures formed, when photons decoupled from baryons. The angular power spectrum of CMB temperature anisotropies is dominated, at scales below the horizon, by acoustic peaks that arise from gravity-driven sound waves in the photon-baryon fluid. The measurement of the positions and the amplitude of these peaks (Frieman et al., 2008) allows cosmologists to determine that the universe is flat within a few percent and indicates that matter contributes only to a small fraction of the cosmic energy budget. However, they also reveal that matter accounts for only about a quarter of the total energy density. To make these observations consistent, in particular when combined with large-scale structure measurements or independent determinations of the Hubble constant, a smoothly distributed energy component is required. This leads naturally to the dark energy hypothesis, which explains the observed late-time acceleration of the Universe.

Dark energy also leaves its mark on large-scale CMB anisotropies through the integrated Sachs-Wolfe (ISW) effect. As photons traverse evolving gravitational potential wells, they experience differential redshifts, causing a small correlation between the CMB and the low-redshift matter distribution.

CMB provides critical constraints on cosmological parameters, such as the Hubble constant H_0 and the matter density Ω_M, the latest constrains of Planck satellite will be described in section 1.11.1.

Type Ia Supernovae

Type Ia supernovae (SNe Ia) are characterized by their hydrogen-free spectra and prominent silicon (Si II) absorption lines at peak brightness. Their light curves follow a well-defined pattern, brightening and fading smoothly with remarkable uniformity. At maximum luminosity, SNe Ia can rival the brightness of their host galaxies, making them detectable at high redshifts, where the influence of local peculiar velocities is minimal. This combination

of consistency in behavior and intrinsic brightness renders SNe Ia exceptional standard candles for measuring cosmic distances and constraining cosmological parameters.

However, the peak luminosity of Type Ia supernovae (SNe Ia) exhibits significant intrinsic variation, which initially posed a challenge for their use in cosmology. A breakthrough came with the discovery of a key empirical correlation (Phillips, 1993) which relates the shape of the light curve to the peak luminosity, allowing to determine the absolute magnitude M_B of SNIa.

In this way, by measuring the apparent magnitude m_B of Supernovae one can compute the luminosity distance d_L using

$$m - M = 5log_{10}(d_L) - 5 \tag{1.126}$$

where d_L is measure in parsec.

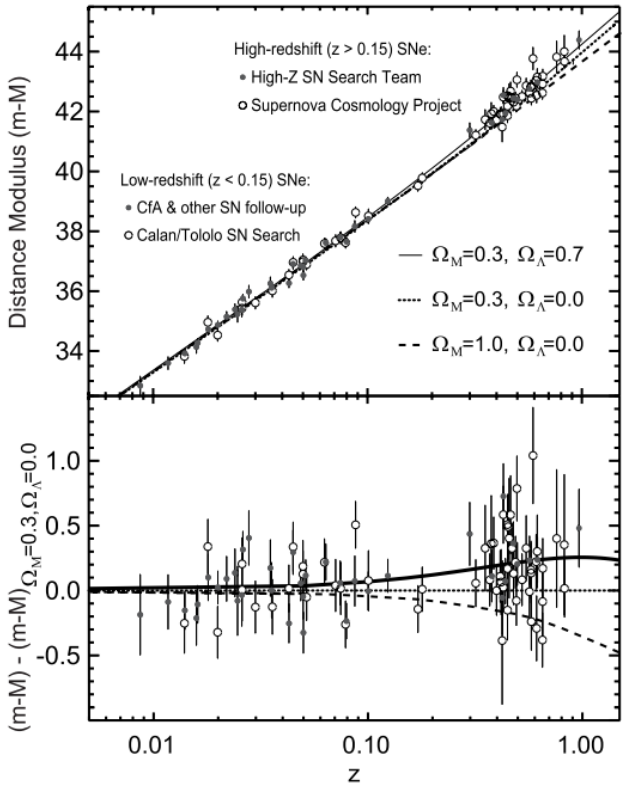

Figure 1.3: Hubble diagram of SNe Ia measured by th Supernova Cosmology Project and High-z Supernova Team from Perlmutter and Schmidt (2003).

In the late 1990s (Frieman et al., 2008) two independent teams, the Supernova Cosmology Project (Perlmutter et al., 1997) and the High-Z Supernova Search (Riess et al., 1998), used SNe Ia to measure the SN Hubble diagram to much larger distances than was previously possible, but discovered that distant supernovae were fainter than expected in a decelerating universe, providing the first direct evidence for cosmic acceleration.

The Hubble diagram, which plots the distance modulus of SNe Ia against redshift, is a powerful tool for constraining the properties of dark energy. The observed dimming of high-redshift SNe Ia implies that the universe has been accelerating for the past several billion years. By fitting the Hubble diagram to cosmological models, astronomers can constrain the equation-of-state parameter w of dark energy, as shown in 1.6, which describes the ratio of its pressure to its energy density.

Recent results from DESI collaboration (DESI et al., 2025a,b) suggest a deviation from the standard ΛCDM model, favoring a dynamical dark energy scenario where the equation-of-state parameter, modeled as $w(a) = w_0 + w_a(1-a)$, is consistent with $w_0 > -1$ and $w_a < 0$.

1.11.1 ΛCDM model and its challenges

The cosmological constant Λ and the evidence of non-baryonic cold dark matter (CDM) (Bertone et al., 2005; Bergström, 2012), which dominates the matter content of the Universe, constitute now the two fundamental pillars from which the cosmological model (ΛCDM) takes its name.

The ΛCDM model is founded on the assumption of a spatially flat universe, which is strongly supported by cosmic microwave background (CMB) observations. It successfully explains a broad range of cosmological observations, from the anisotropies in the CMB to large-scale structure formation and the observed accelerated expansion of the Universe.

The cosmological constant Λ is interpreted as the energy density of the vacuum, which has a constant equation of state $w = -1$, meaning that its density remains constant over cosmic time.

The latest and most precise constraints on the ΛCDM parameters come from the Planck satellite's 2018 data release (Aghanim et al., 2020), which provides a comprehensive analysis of the CMB power spectra and confirms a nearly flat universe with a total matter density parameter $\Omega_m \simeq 0.315$ and a cosmological constant contribution $\Omega_\Lambda \simeq 0.685$

Despite the agreement with observations (Aghanim et al., 2020), two fundamental problems arise from the cosmological constant Λ: the fine-tuning problem and the coincidence problem.

As we saw in section 1.6, the Einstein equations are modified by the presence of the cosmological constant Λ, which introduces a density ρ_Λ, and pressure p_Λ, related by:

$$\rho_\Lambda = -\frac{p_\Lambda}{c^2} = \frac{\Lambda c^2}{8\pi G} \tag{1.127}$$

As observations lead to $\Omega_\Lambda \simeq 0.68$ (Aghanim et al., 2020), one can find that the energy density associated with the cosmological constant must be

$$|\rho_\Lambda| \sim 10^{-48} GeV^4 \tag{1.128}$$

The energy density of the cosmological constant ρ_Λ can be interpreted as the energy of the vacuum in Quantum Field Theory, that can be theoretically estimated by summing the zero-point energies of all quantum fields up to a high-energy cut-off scale. Assuming such cut-off at the Planck scale, $M_{Pl} \sim 10^{18} GeV$ (Carroll, 2001), leads to:

$$|\rho_\Lambda| \sim 10^{72} GeV^4 \tag{1.129}$$

The cosmological constant problem arises when comparing this theoretical estimate of ρ_Λ to the value derived from observational constraints, revealing a discrepancy of ~ 120 orders of magnitude.

The cosmological constant problem highlights a severe fine-tuning issue: the observed vacuum energy density is incredibly small compared to theoretical predictions, requiring a severe cancellation of nearly 120 orders of magnitude. Alternative theories, such as Dynamical dark energy models, propose that the vacuum energy evolves over time, potentially avoiding the need for such extreme fine-tuning by naturally driving the effective cosmological constant toward a small value through dynamical processes rather than static cancellation.

The cosmological coincidence problem, instead, questions why the densities of dark energy and matter are of the same order of magnitude today ($\rho_\Lambda/\rho_m \sim O(1)$) (Velten et al., 2014), given that their evolution differs drastically: while matter dilutes with expansion according to $\rho_m \propto a^{-3}$, the cosmological constant term ρ_Λ remains constant. As we saw, the cosmic history can be divided into three different epochs. First, a radiation-dominated epoch which lasts until the matter component overcomes the radiation one, starting the matter-dominated epoch. Then, at recent epochs, the Universe moves from matter-domination to dark-energy domination. Under the assumption of a cosmological constant ($w = -1$), the redshift of this equivalence can be easily evaluated as

$$\rho_{0,m}(z_{\Lambda,eq})(1 + z_{\Lambda,eq})^3 = \rho_{0,\Lambda} \tag{1.130}$$

which leads to

$$z_{\Lambda,eq} = \left(\frac{\rho_{0,\Lambda}}{\rho_{0,m}}\right)^{1/3} - 1 \simeq 0.30 \tag{1.131}$$

In the standard ΛCDM model dark energy remains constant while matter dilutes as $\rho_m \propto a^{-3}$, making their current similarity appear an unnatural coincidence. This would require highly fine-tuned initial conditions, as their densities diverge drastically in both the early universe (dominated by matter and radiation) and the far future (dark energy-dominated).

These Λ-related problems suggest that the cosmological constant might not be the complete explanation for dark energy. As such, theorists have explored dynamical alternatives, such as interpreting dark energy as a scalar field (Wetterich, 1988) or modeling interactions between dark energy and dark

matter (Wetterich, 1994; Amendola, 2000), to refine our understanding of cosmic acceleration. In chapter 2 we will describe a particular class of Interacting Dark Energy (IDE) models to offer a viable alternative to ΛCDM model.

1.11.2 Observational Tensions

In the last few years, with the increase of the experimental sensitivity, statistically significant tensions have emerged among different observations on the Hubble constant H_0, figure 1.4, the amplitude of the growth of structure S_8 (Di Valentino et al., 2021b,a) and a third tension from DESI results (DESI et al., 2025a,b) related to the dark energy equation-of-state parameter w within the ΛCDM model.

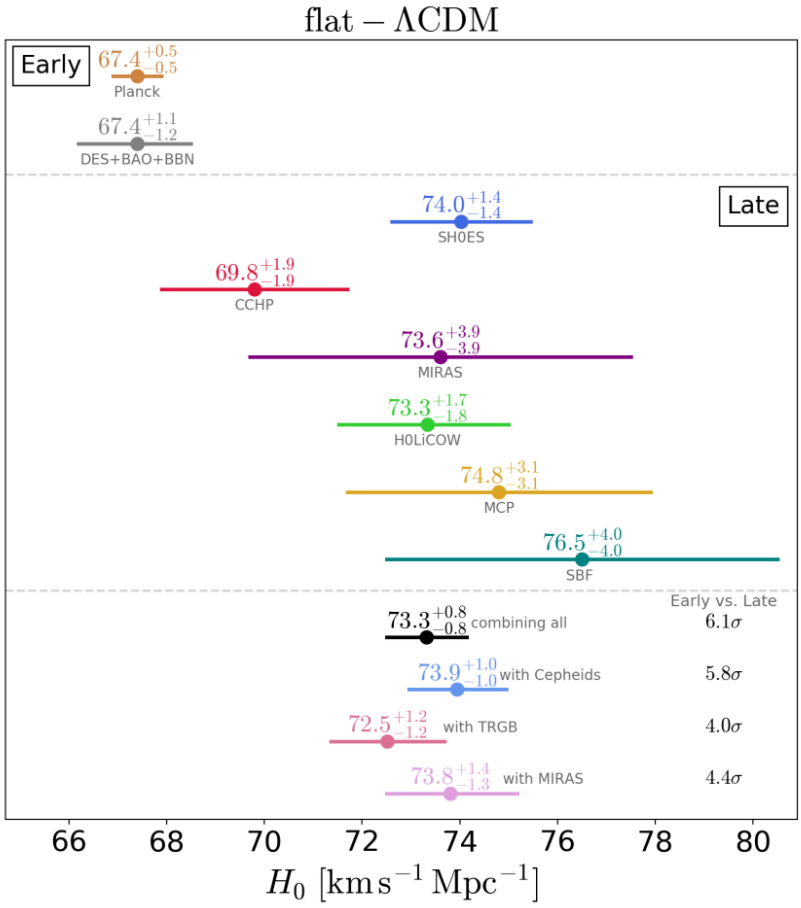

Figure 1.4: Hubble Constant predictions and measurements taken from the recent literature shown in Verde et al. (2019). Bottom panel shows late-Universe measurements which are in tension with the early-Universe measurements in the top panel.

Regarding H_0, while observations based on the CMB and on the assumption of a ΛCDM cosmology lead to $H_0 = (67.36 \pm 0.54)\ km/s/Mpc$ (Aghanim

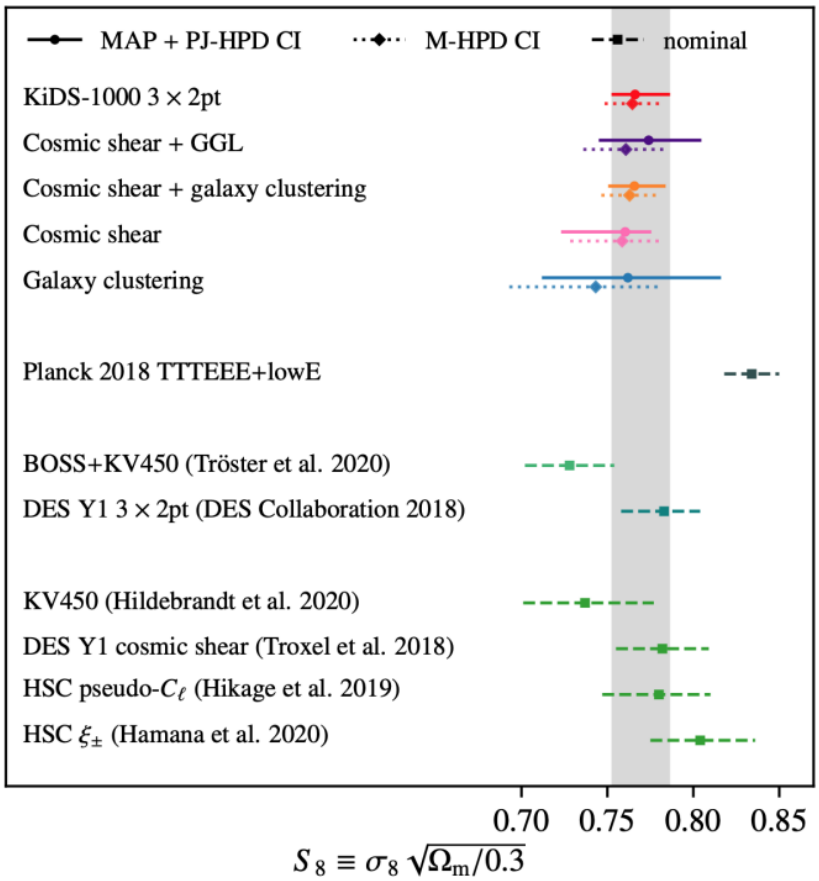

Figure 1.5: Constraints on the structure growth parameter S_8 from different probe combinations shown in Heymans et al. (2021). As we can notice the Planck-2018 (Aghanim et al., 2020) contrain on S_8 (from CMB analysis) is in tension with S_8 measures in later times (such as the cosmic shear observations from Heymans et al. (2021))).

et al., 2020), recent observations of Cepheid variables in the the Small Magellanic Cloud (SMC) find $H_0 = (73.17 \pm 0.86)\ km/s/Mpc$ (Breuval et al., 2024). In the same way, a tension on the parameter $S_8 \equiv \sigma_8 \sqrt{\Omega_m/0.3}$ is found, where Ω_m represents the cosmic matter density in units of critical density and σ_8 the amplitude of linear matter density fluctuations measured on the $8Mpc/h$ scale. As shown in figure 1.5, extimations based on CMB observations lead to $S_8 = 0.834 \pm 0.016$ (Di Valentino et al., 2021a) while low-redshift measurements conduct to values of $S_8 \simeq 0.73 \pm 0.01$ (Burger et al., 2023).

Recent results from the Dark Energy Spectroscopic Instrument (DESI, (DESI et al., 2025a,b)) have further challenged the ΛCDM model. The DESI collaboration reports a 2.3σ tension between their baryon acoustic oscillation (BAO) measurements and CMB-derived parameters within ΛCDM (DESI et al., 2025a,b). When combined with CMB data, the DESI measurements favor a dynamical dark energy model with a time-evolving equation of state,

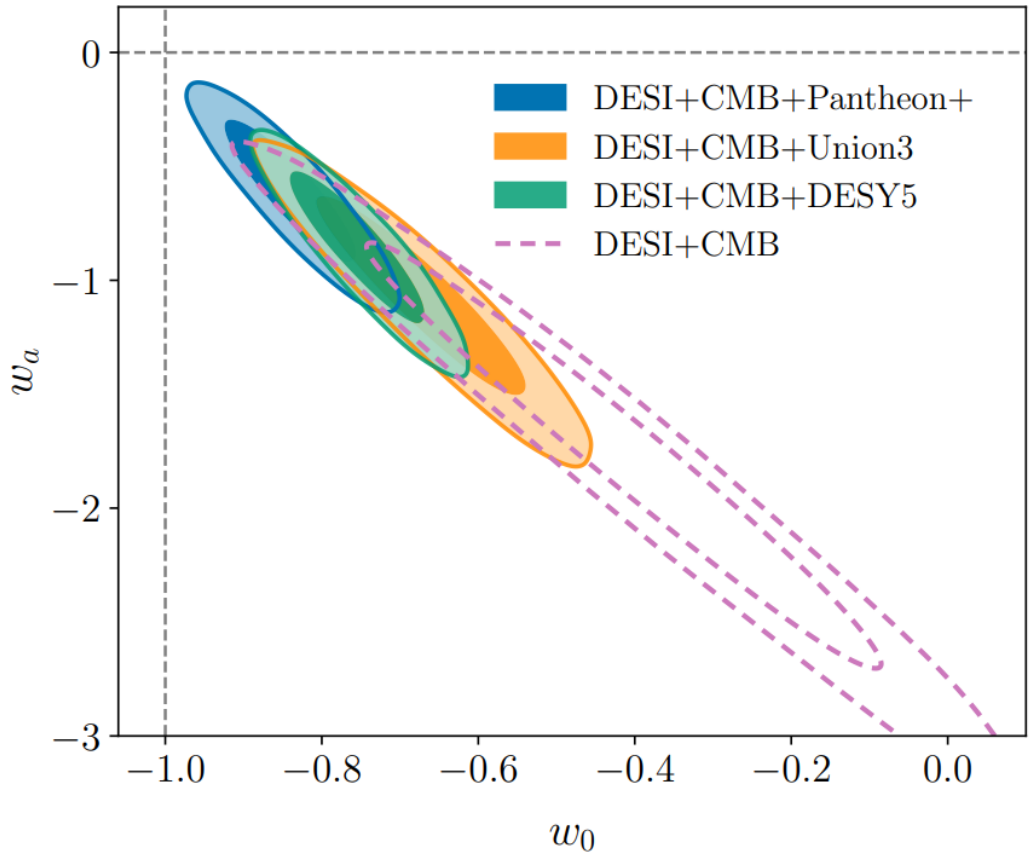

Figure 1.6: Tension on the Dark Energy w parameter presented in DESI et al. (2025b). While the ΛCDM constant value of $w = -1$ is represented by the intersection of the dotted lines ($w_0 = -1, w_a = 0$), the DESI results suggest a time-dependent w with $w_0 > -1$ and $w_a < 0$

parametrized as $w(a) = w_0 + w_a(1 - a)$ resulting in a w that evolves from $\sim (w_0 + w_a)$ at high redshifts to a present-day value of w_0, over ΛCDM at 3.1σ significance. The preferred solutions (figure 1.6) lies in the quadrant with $w_0 > -1$ and $w_a < 0$, suggesting a weakening of dark energy at late times. This preference increases to $2.8 - 4.2\sigma$ when Supernova datasets are included, depending on the SNe sample used (DESI et al., 2025b).

These tensions pose persistent challenges to the standard ΛCDM cosmology, suggesting the need for alternatives to the latter. Among the proposed solutions, dynamical dark energy models, particularly those involving interactions in the dark sector, have gained traction as potential ways to reconcile these tensions (Poulin et al., 2018; Di Valentino et al., 2021b,c).

In the next chapter, we will focus on a specific class of these models, called coupled dark energy (Amendola, 2000), examining how its non-gravitational interactions could provide a unified framework for mitigating both the H_0 and S_8 tensions.

Chapter 2

Dark Energy models

The ΛCDM model, while remarkably successful in describing a wide range of cosmological observations, faces significant theoretical and observational challenges, as we have seen in the previous chapter. These include the fine-tuning problem of the cosmological constant Λ, the cosmic coincidence problem and tensions in current measurements of the Hubble constant H_0, the amplitude of matter fluctuations S_8 and the deviation of the Dark Energy equation-of-state parameter w from the $w = -1$ ΛCDM case, as recently highlighted by DESI results (DESI et al., 2025a,b).

In this chapter, we investigate several dark energy models that extend the standard cosmological framework. We begin by introducing quintessence models in which the dark energy is represented by a time-evolving scalar field. From there, more complex interactions can be introduced, such as couplings between dark energy and dark matter (Amendola, 2000), leading to Coupled Dark Energy models. Finally, a particular subclass of Coupled Dark Energy models is represented by Bouncing Dark Energy models, in which the scalar field evolves under a confining self-interaction potential, giving rise to a peculiar dynamics. These models, in fact, offer an alternative to standard attractor solutions by allowing the field to undergo a "bounce" in its trajectory, potentially addressing both early and late-time acceleration.

As we will describe later, the latter models provide viable alternatives that may help resolve some of the limitations of the ΛCDM model.

2.1 Quintessence

Since the discovery of an accelerated cosmic expansion, the cosmological constant Λ has been widely adopted to explain this effective repulsive pull acting against gravitational attraction at cosmological scales. While ΛCDM successfully describes a broad range of cosmological observations, it faces two major challenges, as discussed in Chapter 1.11:

- **The fine-tuning problem**: A precise and unnatural tuning of Λ is

required to match observations, given the large discrepancy between theoretical predictions and the observed value.

- **The coincidence problem**: Dark matter and dark energy have comparable energy density in the current epoch, leading to question their independent nature and origin as postulated in the ΛCDM model.

Among dynamical dark energy models, one of the simplest and most natural extensions of ΛCDM is quintessence, in which a light classical scalar field ϕ slowly rolls down a self-interaction potential $V(\phi)$, leading to a time-dependent equation of state (Joyce et al., 2016; Wetterich, 1988; Ratra and Peebles, 1988). In this scenario, the equation of motion for the scalar field is described by the homogeneous Klein-Gordon equation:

$$\ddot{\phi} + 3H\dot{\phi} + \frac{dV}{d\phi} = 0\,, \tag{2.1}$$

where ϕ is assumed to be spatially homogeneous, i.e. $\phi(\vec{x}, t) = \phi(t)$ and $V(\phi)$ is the self-interaction potential.

The energy density ρ_ϕ and pressure p_ϕ of a quintessence field follow from its stress-energy tensor (Wetterich, 1988; Ratra and Peebles, 1988; Peebles and Ratra, 2003). Starting with the action:

$$S = \int d^4x\sqrt{-g}\left[-\frac{1}{2}g^{\mu\nu}\partial_\mu\phi\partial_\nu\phi - V(\phi)\right], \tag{2.2}$$

the stress-energy tensor is obtained by variation of the action with respect to the metric $g_{\mu\nu}$:

$$T_{\mu\nu} = \partial_\mu\phi\partial_\nu\phi - g_{\mu\nu}\left[\frac{1}{2}g^{\alpha\beta}\partial_\alpha\phi\partial_\beta\phi - V(\phi)\right]. \tag{2.3}$$

For a homogeneous field $\phi(t)$ in FLRW metric, we compute the pressure p and density ρ as:

$$T_{00} = \frac{1}{2}\dot{\phi}^2 + V(\phi) \equiv \rho_\phi \tag{2.4}$$

$$T_{ii} = a^2\left(\frac{1}{2}\dot{\phi}^2 - V(\phi)\right) \equiv a^2 p_\phi\,. \tag{2.5}$$

In this way the energy density and pressure are

$$\begin{aligned} \rho_\phi &= \frac{1}{2}\dot{\phi}^2 + V(\phi) \\ p_\phi &= \frac{1}{2}\dot{\phi}^2 - V(\phi)\,. \end{aligned} \tag{2.6}$$

The scalar-field dark energy can be described by the equation-of-state parameter

$$w = \frac{p_\phi}{\rho_\phi} = \frac{\dot{\phi}^2/2 - V(\phi)}{\dot{\phi}^2/2 + V(\phi)} = \frac{-1 + \dot{\phi}^2/2V}{1 + \dot{\phi}^2/2V}\,. \tag{2.7}$$

If the scalar field evolves slowly ($\dot{\phi}^2/2V \ll 1$) we have $w \simeq -1$, which means that the scalar field behaves like a cosmological constant.

Conversely, if the term $\frac{\dot{\phi}}{2V}$ gets larger, the quintessence model can exhibit a significant departure from the cosmological constant ($w \simeq 1$) behavior. As we show in chapter 5.1, if the kinetic term $\frac{\dot{\phi}}{2} \gg V$ the equation-of-state parameter w approaches the value $+1$, behaving like a "stiff matter" (La Vacca et al., 2009).

2.2 Coupled Dark Energy

After introducing quintessence as a dynamical scalar field responsible for cosmic acceleration, it is natural to consider interactions between this field and other cosmic components. The coupled quintessence model, proposed by Wetterich (1994) and Amendola (2000), explores this idea by allowing explicit coupling between the quintessence field and matter. Coupled Dark Energy models are essentially quintessence models, i.e. dark energy is represented by a dynamic scalar field, with the presence of a direct coupling between the quintessence scalar field and the matter component.

In Coupled Dark Energy models, interactions between the DE scalar field and other species can be controlled by a time-dependent coupling function, named β.

A scalar field coupled to ordinary matter (beyond gravitational interactions) with a strength comparable to gravity would likely has already been detected (Carroll, 1998). However, if the coupling to baryonic matter differs from the coupling to dark matter (Amendola, 2000), it is possible that such a coupling exists. In the case of constant coupling, observational constraints (Gómez-Valent et al., 2020) place upper limits on the coupling constant $\beta \lesssim 0.05$.

In this work, we consider a coupled dark energy (DE) model where the DE scalar field interacts exclusively with cold dark matter (CDM). While such models could, in principle, include a coupling to baryonic matter, this scenario is strongly disfavored by local gravity experiments, as discussed in Damour et al. (1990). For instance, solar system tests impose stringent constraints on deviations from General Relativity, effectively ruling out significant couplings to baryons (Will, 2014). Therefore, we set the DE-baryon coupling to zero, focusing instead on the interaction between DE and CDM.

Considering a multi-component system, the total stress energy tensor $T^{\mu\nu}$ is conserved (Kodama and Sasaki, 1984)

$$\sum_{\alpha} \nabla_{\nu} T^{\nu}_{(\alpha)\mu} = 0\,. \tag{2.8}$$

However, for an individual species α, this conservation law may not hold, as long as 2.8 is fulfilled.

The energy transfer between different species and the DE scalar field can be described by introducing a source term $Q_{(\alpha)\mu}$. For a single component α

$$\nabla_\nu T^\nu_{(\alpha)\mu} = Q_{(\alpha)\mu}(\phi) T_{(\alpha)} \nabla_\nu(\phi)\,, \tag{2.9}$$

where ∇_ν represents the covariant derivative, $T_{(\alpha)}$ is the trace of the stress-energy tensor relative to the component α with α=c for CDM, b for baryons, r for radiation, n for neutrinos.

Maintaining valid the total stress-energy conservation , eq. 2.8, we can write the coupling term associated with the dark energy scalar field as

$$\nabla_\nu T^\nu_{(\phi),\mu} = \sum_\alpha \left[Q_{(\alpha)}(\phi) T_{(\alpha)}\right] \nabla_\nu \phi\,. \tag{2.10}$$

Given the definition of stress-energy tensor in section 1.1, we can compute its trace T, in a FLRW metric, as

$$T = T^\mu_\mu = 3p - \rho\,. \tag{2.11}$$

For radiation and relativistic neutrinos, the equation-of-state parameter is $w = 1/3$, which implies $p = \rho/3$, leading to a vanishing trace T. Therefore, their stress-energy tensors are traceless and, as we can see from 2.9 they remain uncoupled, regardless of the value of Q.

Assuming a Friedmann-Lemaitre-Robertson-Walker (FLRW) metric, for which we have the line element $ds^2 = a^2(\tau)(-d\tau^2 + \delta i j dx^i dx^j)$, we obtain

$$\begin{aligned} &\Gamma^0_{00} = \Gamma^i_{00} = \Gamma^0_{i0} = 0\,, \\ &\Gamma^i_{j0} = \delta^i_j \frac{\dot{a}}{a}\,, \\ &\Gamma^0_{ij} = \delta_{ij} \dot{a} a\,. \end{aligned} \tag{2.12}$$

The $\nu = 0$ component of 2.9 sets the conservation equation for each species

$$\begin{aligned} &\frac{\partial \rho_c}{\partial t} + 3H\rho_c = -Q_{(c)} \rho_c \dot{\phi}\,, \\ &\frac{\partial \rho_b}{\partial t} + 3H\rho_b = 0\,, \\ &\frac{\partial \rho_r}{\partial t} + 4H\rho_r = 0\,, \end{aligned} \tag{2.13}$$

while, for the ϕ component we obtain the following Klein-Gordon equation

$$\ddot{\phi} + 3H\dot{\phi} + \frac{\partial V(\phi)}{\partial \phi} = Q_{(\phi)0} \rho_c\,. \tag{2.14}$$

If we define the coupling coefficient β as

$$\beta_\alpha \equiv \sqrt{\frac{3}{2}} Q_{(\alpha)0} M_{Pl} \quad , where \quad M_{Pl} = \frac{1}{8\pi G}\,, \tag{2.15}$$

then we can rewrite the Klein Gordon equation as

$$\ddot{\phi} + 3H\dot{\phi} + \frac{dV(\phi)}{d\phi} = \sqrt{\frac{2}{3}}\beta_c(\phi)\frac{\rho_c}{M_{Pl}}\,, \tag{2.16}$$

and the CDM conservation equation as

$$\frac{\partial \rho_c}{\partial t} + 3H\rho_c = \sqrt{\frac{2}{3}}\beta_c(\phi)\frac{\rho_c\dot{\phi}}{M_{Pl}}\,. \tag{2.17}$$

While the first Friedmann equation can be written as

$$3H^2 = \frac{1}{M_{Pl}}(\rho_r + \rho_c + \rho_b + \rho_\phi)\,. \tag{2.18}$$

We can notice that, differently from the ΛCDM case, the CDM density does not scale anymore like a^{-3}, but its density evolution is affected by the presence of the coupling with the DE scalar field according to

$$\rho_m(a) = \rho_m(a_0)a^{-3}exp\left[-\sqrt{\frac{2}{3}}\int \frac{\beta(\phi)}{M_{Pl}}\frac{d\phi}{da}da\right], \tag{2.19}$$

where the exponential extra factor accounts for the energy exchange between the DE scalar field and the CDM component.

If one assumes the conservation of the number density of CDM particles, the mass of coupled matter particles is not constant anymore but changes in time according to

$$M_c(a) = M_c(a_0)exp\left[-\sqrt{\frac{2}{3}}\int \frac{\beta(\phi)}{M_{Pl}}\frac{d\phi}{da}da\right]. \tag{2.20}$$

So, finally, the background dynamic equations which describe the evolution of a cosmological model characterized by the coupling between dark energy and dark matter are given by

$$\begin{aligned}
&\ddot{\phi} + 3H\dot{\phi} + \frac{dV(\phi)}{d\phi} = \sqrt{\frac{2}{3}}\beta_c(\phi)\frac{\rho_c}{M_{Pl}}\,,\\
&\dot{\rho}_c + 3H\rho_c = \sqrt{\frac{2}{3}}\beta_c(\phi)\frac{\rho_c\dot{\phi}}{M_{Pl}}\,,\\
&\dot{\rho}_b + 3H\rho_b = 0\,,\\
&\dot{\rho}_r + 3H\rho_r = 0\,,\\
&3H^2 = \frac{1}{M_{Pl}}(\rho_r + \rho_c + \rho_b + \rho_\phi)\,.
\end{aligned} \tag{2.21}$$

2.3 Bouncing Coupled Dark Energy

The time evolution of the scalar field ϕ is determined by the choice of the self-interacting potential $V(\phi)$. Different choices of $V(\phi)$ will also affect the expansion history and consequently the growth of cosmic structures. Two widely used the potentials $V(\phi)$ are the inverse power-law (Ratra and Peebles, 1988)

$$V(\phi) = A\phi^{-\alpha}\,, \tag{2.22}$$

and the exponential (Wetterich, 1988)

$$V(\phi) = Ae^{-\alpha\phi}\,, \tag{2.23}$$

where ϕ has been expressed in units of the reduced Plank mass $M_{Pl} = 1/\sqrt{8\pi G}$. In both cases, the scalar field evolves monotonically by rolling down the potential.

A different choice of $V(\phi)$ is represented by the SUGRA potential (Brax and Martin, 1999)

$$V(\Phi) = A\phi^{-\alpha}e^{\phi^2/2}\,, \tag{2.24}$$

which is a combination of the Ratra-Peebles and exponential potentials. The key feature of the SUGRA potential is the presence of a global minimum point for $\phi = \sqrt{\alpha}$ where the derivative of the potential $V(\phi)$ in equation 2.16 vanishes.

Consider a scalar field starting from its minimum with zero velocity, i.e. $\phi_i = \sqrt{\alpha}, \dot{\phi} = 0$. From equation 2.16, the acceleration of the scalar field reads

$$\ddot{\phi} = \sqrt{\frac{2}{3}}\beta_c\frac{\rho_c}{M_{Pl}}\,. \tag{2.25}$$

Therefore, in the presence of a coupling $\beta \neq 0$, the potential moves away from its equilibrium point ($\phi = \sqrt{\alpha}$) evolving towards the direction specified by the sign of the coupling β.

As explained in Baldi (2011), we will consider our model to start at rest in its global minimum at very early times as initial conditions due to the fact that in radiation dominated era any dynamical evolution of the scalar field could be efficiently damped by Hubble friction.

It is interesting to notice that in the absence of any coupling between CDM and DE, the scalar field remains at rest at its minimum point throughout the entire expansion history of the universe, acting as a cosmological constant Λ.

We can see an example of the evolution in redshift of a DE scalar field characterized by a SUGRA potential in figure 2.1 taken from Baldi (2011). Baldi (2011) employed a SUGRA potential with the scalar field starting at rest at its potential minimum, at very high redshifts, with a negative coupling $\beta_c = -0.15$. Therefore, we can see from eq. 2.25 that the initial acceleration of the scalar field $\ddot{\phi} \propto \beta_c$ is negative, leading the field to evolve towards the left part of the curve, i.e. the power-law side of the SUGRA potential. The

bounce takes place when the scalar field reaches its inversion point (labeled as ϕ_{inv} in figure 2.1) after which the field inverts its evolution rolling back towards its minimum point.

The case of positive coupling $\beta > 0$ would result in a different evolution of the field ϕ as its initial acceleration would be positive, leading to an evolution of the field towards the right part of its potential, i.e. the exponential side of the SUGRA potential.

While the shape of the SUGRA potential in the left part is described by a power law $\phi^{-\alpha}$ the right part is represented by a potential $e^{\phi^2/2}$. Therefore, Bouncing Coupled Dark Energy models (BCDE) with same amplitude of β but opposite sign result in significantly different evolutions due to the different shape of the potential, and so different bouncing point.

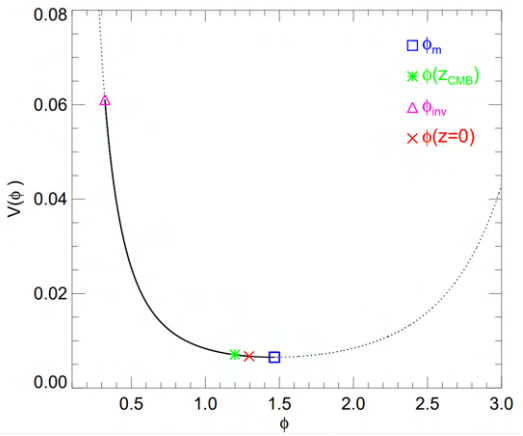

Figure 2.1: Trajectory of a DE scalar field ϕ along its self-interaction SUGRA potential shown in Baldi (2011). The model is characterized by a coupling coefficient $\beta_c = -0.15$, $\alpha = 2.15$, for this reason the potential starts from its minimum $\phi_m = \sqrt{\alpha} \simeq 1,47$ and evolves to the left-side part of the potential. The potential evolves until it reaches the inversion point ϕ_{inv} where it inverts its motion and rolls back to its minimum.

As one can see from the CDM continuity equation, eq. 2.17, the energy transfer between CDM and the DE scalar field is directly proportional to the factor $\beta_c\dot{\phi}$.

In case of a positive coupling $\beta_c > 0$, the scalar field velocity, before reaching the inversion point, is positive. This implies a positive factor $\beta_c\dot{\phi}$, leading to a decreasing CDM particle mass. Once the field reaches the inversion point, it reverses its direction of motion, changing the sign of $\dot{\phi}$, which in turn causes the CDM particle mass to increase.

In case of negative coupling $\beta < 0$, the sign of the initial field velocity $\dot{\phi}$ is negative, since the initial acceleration $\ddot{\phi}$ is also negative. Therefore, the factor $\beta\dot{\phi}$ is still positive, resulting again in a decreasing CDM mass in the early universe. Similarly to the $\beta > 0$ case, after the scalar field with $\beta < 0$ passes the inversion point, $\dot{\phi}$ changes sign, and the CDM mass begins to increase.

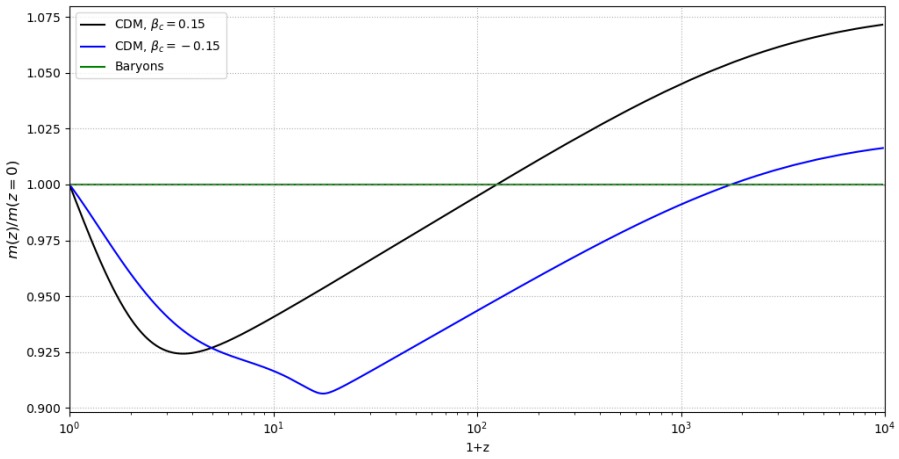

Figure 2.2: Mass evolution of CDM and baryons as function of redshift for different choice of coupling strength β_c in a SUGRA potential.

Figure 2.2 shows the evolution of the particle mass in units of $m(z = 0)$ for both CDM and baryonic particles.

2.4 Linear perturbations

Following the calculations shown in Amendola (2000, 2004), we can rewrite the background equations in the previous chapter as

$$x \equiv \frac{\phi'}{M_{\rm Pl}\sqrt{6}}\,, \quad y \equiv \frac{\sqrt{V(\phi)/3}}{M_{\rm Pl}H}\,, \quad r \equiv \frac{\sqrt{\rho_r/3}}{M_{\rm Pl}H}\,, \quad v \equiv \frac{\sqrt{\rho_b/3}}{M_{\rm Pl}H}\,. \tag{2.26}$$

where the prime represents a derivative with respect to the e-folding time $N \equiv ln(a)$. Using these new variables the density parameters $\Omega_\alpha = \rho_\alpha/(3H^2M_{Pl}^2)$ can be written as

$$\Omega_b = v^2, \quad \Omega_r = r^2, \quad \Omega_\phi = x^2 + y^2\,. \tag{2.27}$$

Consistently with the latest observations of Planck (Aghanim et al., 2020), we assume the Universe to be exactly flat, leading to $\Omega_c = 1-x^2-y^2-r^2-v^2$. With these assumptions the background equations can be expressed as

$$\begin{aligned}
x' &= \frac{x}{2}\left(3x^2 - 3y^2 + r^2 - 3\right) + \alpha y^2 + \beta_c(\phi)\left(1 - x^2 - y^2 - r^2 - v^2\right)\,, \\
y' &= \frac{y}{2}\left(3x^2 - 3y^2 + r^2 + 3\right) - \alpha xy\,, \\
r' &= \frac{r}{2}\left(3x^2 - 3y^2 + r^2 - 1\right)\,, \\
v' &= \frac{v}{2}\left(3x^2 - 3y^2 + r^2\right)\,, \\
H' &= -\frac{H}{2}\left(3x^2 - 3y^2 + r^2 + 3\right)\,.
\end{aligned} \tag{2.28}$$

The system of equations 2.28 describes the time evolution of the cosmic background in the presence of a coupling between CDM and DE.

Considering a perturbed metric in the form of longitudinal gauge (Amendola, 2004)

$$ds^2 = a^2(\tau)\big[-(1+2\Phi)d\tau^2 + (1-2\Phi)\delta_{ij}dx^i dx^j\big] \tag{2.29}$$

where τ is the conformal time and Φ the gravitational potential, we can write the conformal Hubble function as $\mathcal{H} \equiv (da/d\tau)/a = aH$. We can then define a set of perturbation variables as

$$\begin{aligned}
&\delta_c \equiv \delta\rho_c/\rho_c\,,\\
&\delta_b \equiv \delta\rho_b\rho_b\,,\\
&u_i \equiv a\,dx_i/(\mathcal{H}dt)\,,\\
&\nabla\cdot\mathbf{u_c} \equiv \theta_c\,,\\
&\nabla\cdot\mathbf{u_b} \equiv \theta_b\,,\\
&\varphi \equiv \delta\phi/(M_{Pl}\sqrt{6})\,.
\end{aligned} \tag{2.30}$$

Since we are interested in the evolution of matter density perturbations during matter domination, for simplicity we neglect the radiation density fluctuations. We also define the dark energy scalar mass m_ϕ^2 and its dimensionless version $\hat{m}_\phi^2$ (Amendola, 2000)

$$m_\phi^2 = \frac{d^2V(\phi)}{d\phi^2}, \quad \hat{m}_\phi^2 \equiv \frac{m_\phi^2}{H} = \frac{1}{H}\frac{d^2V(\phi)}{d\phi^2} = 2\alpha^2 y^2\,. \tag{2.31}$$

To represent a characteristic scale associated with the perturbation, we can define the parameter λ such that in Fourier space $\lambda = \mathcal{H}/k$, while in real space λ^{-2} corresponds to the operator $-\mathcal{H}^{-2}\nabla^2$.

Perturbing the Einstein equations and the conservation equations we obtain the following linear perturbation equations

$$\begin{aligned}
&\delta_c' = -\theta_c + 3\Phi' - 2\beta_c\varphi' - 2\beta_c'\varphi\,,\\
&\theta_c' = -\left(1 + \frac{\mathcal{H}'}{\mathcal{H}} - 2\beta_c x\right)\theta_c + \lambda^{-2}(\Phi - 2\beta_c\varphi)\,,\\
&\delta_b' = -\theta_b + 3\Phi'\,,\\
&\theta_b' = -\left(1 + \frac{\mathcal{H}'}{\mathcal{H}}\right)\theta_b + \lambda^{-2}\Phi\,,\\
&\varphi'' + \left(2 + \frac{\mathcal{H}'}{\mathcal{H}}\right)\varphi' + \left(\lambda^{-2} + \tilde{m}_\phi^2 - \frac{\Omega_c\beta_c'}{x}\right)\varphi\\
&\quad - 4\Phi' x - 2y^2\alpha\Phi = \beta_c\Omega_c(\delta_c + 2\Phi)\,.
\end{aligned} \tag{2.32}$$

The derivative of the coupling term β' contributes to the last equation of the system 2.32 as an effective mass term (Amendola, 2004)

$$\hat{m}_{\beta_c}^2 \equiv \frac{\Omega_c\beta_c'(\phi)}{x}\,. \tag{2.33}$$

Restricting ourselves to the Newtonian limit, $\lambda \ll 1$, the perturbation equations for baryon and CDM read (Baldi, 2010)

$$\begin{aligned}
\delta_c' &= -\theta_c - 2\beta_c'\varphi\,, \\
\theta_c' &= -\left(1 + \frac{\mathcal{H}'}{\mathcal{H}} - 2\beta_c x\right)\theta_c - \frac{3}{2}[\Omega_b\delta_b + \Omega_c\delta_c\Gamma_c]\,, \\
\delta_b' &= -\theta_b\,, \\
\theta_b' &= -\left(1 + \frac{\mathcal{H}'}{\mathcal{H}}\right)\theta_b - \frac{3}{2}[\Omega_b\delta_b + \Omega_c\delta_c]\,,
\end{aligned} \tag{2.34}$$

where

$$\Gamma_c \equiv 1 + \frac{4}{3}\frac{\beta_c^2(\phi)}{1+\lambda^2\hat{m}^2}\,. \tag{2.35}$$

The Newtonian limit in the last equation of the system 2.32, as shown in Amendola (2004), leads to $\phi \sim \lambda^2$, this suggest that the term β_c' in the first equation of 2.32 can be dropped as long as $\beta_c' \sim \mathcal{O}(1)$ and the same for $\lambda^2\hat{m}^2$, from which we get

$$\Gamma_c = 1 + \frac{4}{3}\beta_c^2(\phi)\,. \tag{2.36}$$

With these considerations, the perturbation equations 2.32 allow us to derive the dynamic equations for the density fluctuation as done in Baldi (2010)

$$\delta_c'' + \left(1 + \frac{\mathcal{H}'}{\mathcal{H}} - 2\beta_c x\right)\delta_c' - \frac{3}{2}\left[\Omega_b\delta_b + \Omega_c\delta_c\Gamma_c\right] = 0\,, \tag{2.37}$$

$$\delta_b'' + \left(1 + \frac{\mathcal{H}'}{\mathcal{H}}\right)\delta_b' - \frac{3}{2}\left[\Omega_b\delta_b + \Omega_c\delta_c\right] = 0\,, \tag{2.38}$$

and the vectorial acceleration equations in real space for baryon and CDM

$$\dot{\boldsymbol{v}}_c = -\tilde{H}\mathbf{v}_c - \boldsymbol{\nabla}\left[\sum_{i=c}\frac{\Gamma_c GM_i(\phi)}{r_i} + \sum_{j=b}\frac{GM_j}{r_j}\right]\,, \tag{2.39}$$

$$\dot{\boldsymbol{v}}_b = -Hv_c - \boldsymbol{\nabla}\left[\sum_{i=c}\frac{GM_i(\phi)}{r_i} + \sum_{j=b}\frac{GM_j}{r_j}\right]\,, \tag{2.40}$$

where $\tilde{H} \equiv H[1 - 2\beta_c(\phi)x]$ and $\boldsymbol{v}_b, \boldsymbol{v}_c$ are the peculiar velocities for baryon and CDM respectively.

As already shown by Baldi (2010), from equations 2.39 we can notice that the presence of a coupling between DE-CDM modifies the acceleration equation of CDM particles through three factor modifications.

Firstly, the $2\beta_c(\phi)x\boldsymbol{v}_c$ affects the Hubble expansion term as an extra friction. This extra friction term does not depend only on the coupling β_c but also on the sign of the scalar field velocity term $x \propto \dot{\phi}/H$. Therefore, the

background evolution of the scalar field has a direct impact on the CDM acceleration through the friction term.

Second, the mass of coupled particles, CDM in our case, is not a constant anymore but changes according to equation 2.20, leading to a different contribution to the gravitational potential.

Third, the gravitational acceleration of CDM particles includes an extra factor $\Gamma_c = 1 + \frac{4}{3}\beta_c^2$, which accounts for the fifth-force mediated by the scalar field.

The modifications introduced by the coupling between dark energy and cold dark matter have profound implications for both the background evolution and the growth of cosmic structures, potentially offering a pathway to alleviate some of the observational tensions in modern cosmology, particularly those related to the Hubble constant H_0 and the amplitude of matter fluctuations S_8. As demonstrated, the energy transfer between CDM and the DE scalar field, which depends on both the coupling strength β_c and the evolution of the scalar field, can alter the expansion history of the universe. This modification may help to reconcile discrepancies in H_0 by introducing a dynamical mechanism that adjusts the late-time expansion rate without violating early-universe constraints.

Moreover, the variable mass of coupled CDM particles and the fifth-force contribution ($\Gamma_c = 1 + \frac{4}{3}\beta_c^2$) modify the effective gravitational potential, influencing structure formation. Therefore, a well-tuned coupling could suppress the growth of large-scale structure at late times, potentially easing the S_8 tension between cosmic microwave background (CMB) measurements and low-redshift probes.

Given these effects, coupled DE-CDM models present a compelling framework for addressing key observational challenges. Their ability to simultaneously impact both the background expansion and perturbation growth makes them a rich and testable alternative to ΛCDM. For these reasons, further investigation of these models, particularly their phenomenological consequences and observational signatures, will be a crucial focus in the following chapters.

Chapter 3

Non-linear structure formation

As perturbations continue to grow over time, they eventually exit the linear regime, meaning that the linear approximation can no longer be used to obtain analytical solutions. The linearized equations of motion provide an excellent description of gravitational instability at very early times when density fluctuations are still small ($\delta \ll 1$). However, the linear regime of gravitational instability breaks down when δ becomes comparable to unity, signaling the transition into the non-linear regime.

In the non-linear regime, bound structures begin to form, and baryonic matter becomes dynamically significant due to hydrodynamical effects, star formation, and heating/cooling processes.

The most powerful tool available to study structure formation in the non-linear regime is numerical simulation, particularly N-body simulations.

N-body simulations represent the matter distribution using a discrete number of point-like tracers, referred to as "particles," and track their evolution numerically. Cosmological N-body simulations compute the time evolution of the matter distribution starting from initial conditions consistent with cosmological observations at high redshifts, within periodic, comoving simulation boxes.

3.1 Gravitational algorithms

Gravity is the fundamental force driving instability processes that lead to structure formation.

As a result, the computation of gravitational interactions is the primary focus of cosmological N-body codes. However, the long-range nature of gravity, combined with the high dynamic range required to accurately model structure formation, makes the precise and efficient calculation of gravitational forces particularly challenging.

In the ΛCDM paradigm, the Universe's matter density is dominated by dark matter, which is assumed to be composed of unknown, non-baryonic particles. Due to the vast number of particles involved, direct N-body modeling

of a galaxy or the Universe is computationally infeasible. Instead, a statistical approach using distribution functions is employed.

The state of an N-particle system (Springel, 2014) is described by the exact phase-space distribution function:

$$F(r, v, t) = \sum_{i=1}^{N} \delta(r - r_i(t))\delta(v - v_i(t)) \,, \tag{3.1}$$

which counts the number of particles at phase-space point (r, v) at time t. The one-particle distribution function is obtained by ensemble averaging over many realizations:

$$f_1(r, v, t) = \int Fp \, dr_1 dr_2 \ldots dr_N dv_1 dv_2 \ldots dv_N \,, \tag{3.2}$$

where p represents the probability distribution of the system's phase-space states.

For an uncorrelated system, the two-particle distribution function simplifies as

$$f_2(r, v, r', v', t) = f_1(r, v, t) f_1(r', v', t) \,. \tag{3.3}$$

This assumption holds in collisionless systems, such as dark matter and stars in galaxies, where gravitational interactions dominate over short-range collisions.

Since probability is conserved in phase-space, the system obeys Liouville's theorem:

$$\frac{\partial p}{\partial t} + \sum_i \left(v_i \frac{\partial p}{\partial r_i} + a_i \frac{\partial p}{\partial v_i} \right) = 0 \,. \tag{3.4}$$

From this, the Vlasov (collisionless Boltzmann) equation follows

$$\frac{\partial f}{\partial t} + v \cdot \nabla_r f + a \cdot \nabla_v f = 0 \,, \tag{3.5}$$

which describes the evolution of the phase-space distribution function in a collisionless system. The acceleration is given by the self-consistent gravitational potential

$$\nabla^2 \Phi = 4\pi G\rho, \quad \rho(r, t) = m \int f(r, v, t) dv \,. \tag{3.6}$$

Together, these equations form the Poisson-Vlasov system, governing the large-scale evolution of dark matter and stellar systems.

Since directly solving these equations is infeasible, N-body simulations approximate the system using macro-particles that sample phase space, enabling a computational approach to structure formation in cosmology.

The equations of motion of such a system of particles take the form

$$\begin{aligned} \ddot{\vec{x}}_i &= -\vec{\nabla}_i \phi(\vec{r}_i) \,, \\ \phi(\vec{r}) &= -G \sum_{j=1}^{N} \frac{m_j}{\left[(\vec{r} - \vec{r_j})^2 + \epsilon^2 \right]^{1/2}} \,, \end{aligned} \tag{3.7}$$

where ϵ is the softening length used to ensure the collisionless behavior of the system, avoiding large-angle scattering and the high numerical cost that would be needed to integrate the orbits with sufficient accuracy in singular potentials (Springel, 2014). The adoption of a softening length also implies the introduction of a smallest resolved length scale.

Adopting a direct summation scheme for each of the N equations, we have to calculate a sum of N partial forces, leading to a computational cost of the order $\mathcal{O}(N^2)$. Hence, despite being an exact calculation, it becomes prohibitive for large particles number N.

We need faster and less expensive calculation schemes that allow us to increase the number of particles. The most widely adopted methods are

- the Particle-mesh (PM) algorithm,
- the Hierarchical multipole methods ("Tree algorithm"),
- the Tree-PM method (which is the combination of the two).

3.1.1 PM algorithm

In the Particle-Mesh (PM) method, gravitational forces are computed using a grid-based approach, where particles are interpolated onto a mesh, and the potential is solved with Fourier methods.

Firstly, the discrete system of particles, each with a given position and mass, is converted to a continuous density field adopting a shape function, which describes the mass fraction assigned from a particle to a close mesh grid cell. Considering $\mathbf{x}_m$ the position of cell centers, $\mathbf{x}_i$ the position of a particle i, h the cell side-length, this step is performed by defining an assignment function W

$$W(\mathbf{x}_m - \mathbf{x}_i) = \int_{\mathbf{x}_m - \frac{h}{2}}^{\mathbf{x}_m + \frac{h}{2}} S(\mathbf{x}' - \mathbf{x}_i) d\mathbf{x}' = \int \Pi\left(\frac{\mathbf{x}' - \mathbf{x}_m}{h}\right) S(\mathbf{x}' - \mathbf{x}_i) d\mathbf{x}' \,,$$

which represents the fraction of mass of particle i assigned to cell m, where $S(x)$ is the shape function and $\Pi(x)$ is a top-hat filter defined as:

$$\Pi = \begin{cases} 1 & \text{for } |x| \leq \frac{1}{2} \\ 0 & \text{otherwise} \end{cases} \,.$$

In this way, the density assignment function W can be written as the convolution

$$W(\mathbf{x}) = \Pi\left(\frac{\mathbf{x}}{h}\right) \star S(\mathbf{x}) \,,$$

and the density field can be computed as

$$\rho(\mathbf{x}_m) = \frac{1}{h^3} \sum_{i=1}^{N} m_i W(\mathbf{x}_i - \mathbf{x}_m) \,.$$

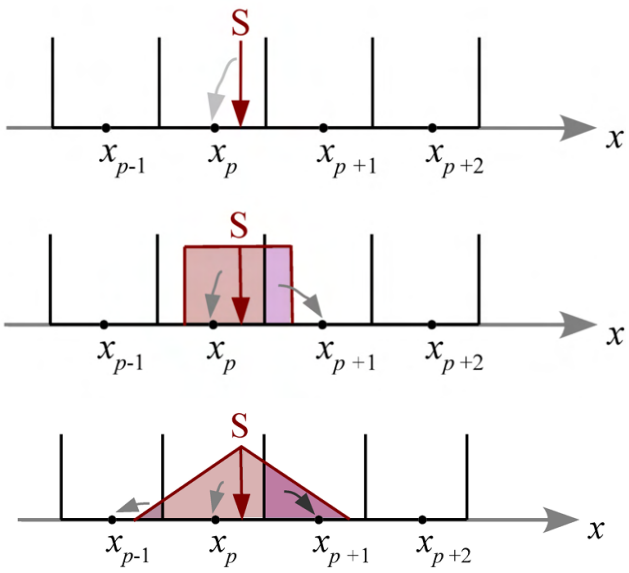

Figure 3.1: NGP (top), CIC(middle) and TSC(bottom) assignment schemes taken from Springel (2014). While for NGP the whole particle mass is assigned to one cell, for the CIC and TSC the mass contribution is divided among the close cells.

The density field depends on the specific choice of the shape function $S(\mathbf{x})$, here we will see some of the most commonly employed assignment schemes.

The simplest possible choice for a shape function is the Nearest Grid Point (NGP) scheme in which the shape function is represented by a Dirac δ function

$$S(\mathbf{x}) = \delta(\mathbf{x})\,. \tag{3.8}$$

In this way the particles contribute with their total mass to the closest grid cell (i.e. the cell where they are located). The resulting mass fraction W is

$$W(\mathbf{x_m} - \mathbf{x_i}) = \Pi\left(\frac{\mathbf{x_m} - \mathbf{x_i}}{h}\right). \tag{3.9}$$

Another possible choice is the Cloud-In-Cell (CIC) assignment described as

$$S(\mathbf{x}) = \frac{1}{3}\Pi\left(\frac{\mathbf{x}}{h}\right), \tag{3.10}$$

in which the mass of each particle is distributed over a cubical volume of the same size of the mesh cells. For the CIC assignment scheme, the assignment function becomes

$$W(\mathbf{x_m} - \mathbf{x_i}) = \int \Pi\left(\frac{\mathbf{x_m} - \mathbf{x}}{h}\right)\frac{1}{h^3}\Pi\left(\frac{\mathbf{x_m} - \mathbf{x_i}}{h}\right)d\mathbf{x}\,. \tag{3.11}$$

The number of cells involved in the CIC assignment depends on the number of dimensions of the simulation. In the 3 dimensional case the cells involved are $2^3 = 8$.

The next higher-order assignment scheme is represented by the Triangular Shaped Clouds (TSC) scheme. In this case the shape function is described by the following:

$$S(\mathbf{x}) = \frac{1}{h^3}\Pi\left(\frac{\mathbf{x}}{h}\right) \star \frac{1}{h^3}\Pi\left(\frac{\mathbf{x}}{h}\right), \tag{3.12}$$

which leads to the following assignment function

$$W(\mathbf{x_m} - \mathbf{x_i}) = \frac{1}{h^6}\int \Pi\left(\frac{\mathbf{x_m} - \mathbf{x}}{h}\right)\Pi\left(\frac{\mathbf{x} - \mathbf{x_i}}{h}\right)\Pi\left(\frac{\mathbf{x} - \mathbf{x}'}{h}\right)d\mathbf{x}d\mathbf{x}'\,. \tag{3.13}$$

As one can see in the bottom panel of figure 3.1, assuming a TSC assignment scheme with total base length of the triangle 2h, the particle mass is in general spread over 3 cells per dimension, thus over $3^3 = 27$ cells for 3D grids.

When interpolating particle masses onto a grid in Particle-Mesh (PM) simulations, the choice of the assignment scheme affects both accuracy and computational cost. NGP represents the simplest approach: while computationally efficient, this scheme produces discontinuous density and force fields that jump abruptly as particles cross cell boundaries. The resulting force law is piecewise constant, leading to noticeable artifacts in the simulation.

CIC provides a smoother alternative by distributing each particle's mass over the nearest grid cells (which are 2 in 1D, 4 in 2D, or 8 in 3D). This scheme generates continuous forces that vary piecewise linearly, offering significantly better behavior than NGP. However, the first derivative of the force still exhibits discontinuities.

TSC offers the highest quality interpolation among these three schemes, spreading each particle's mass over a wider neighborhood (3 cells in 1D, 9 in 2D, or 27 in 3D). This produces forces with continuous first derivatives, resulting in the smoothest representation of the density field. The trade-off comes in increased computational cost and memory requirements, particularly for large simulations.

After the density field is obtained, the algorithm moves to Fourier space to obtain the gravitational potential. Assuming a periodic density field in a cubic box of size L, the density field can be represented as a Fourier series

$$\rho(\mathbf{x}) = \sum_{\mathbf{k}} \rho_{\mathbf{k}} e^{i\mathbf{k}\mathbf{x}}\,, \tag{3.14}$$

where $k = \frac{2\pi}{L}(n_x, n_y, n_z)$ are the discrete wavevectors (with n_x, n_y, n_z integers) and ρ_k are the Fourier coefficients, representing the amplitude of each mode. The coefficients ρ_k are computed via the Fourier transform of the discretized density field

$$\rho_{\mathbf{k}} = \frac{1}{L^3}\int_V \rho(\mathbf{x}) e^{-i\mathbf{k}\mathbf{x}} d\mathbf{x}\,. \tag{3.15}$$

Once the density field is expressed in Fourier space, we can substitute the latter in the Poisson equation obtaining the following relation

$$\Phi_{\mathbf{k}} = -\frac{4\pi G}{\mathbf{k}^2}\rho_{\mathbf{k}}\,. \tag{3.16}$$

Equation 3.16 represents the Poisson equation in Fourier space in a periodic space. It represents a fundamental result as it states that the potential in Fourier space Φ_k can be easily obtained by dividing ρ_k by the square wavenumber k^2, making the solution computationally efficient.

Moving back to real space, through an inverse Fourier transform, the force field can finally be computed solving $\mathbf{f} = -\nabla\Phi$ with a finite difference method scheme.

Once the force field is computed on the PM grid, the force acting on each particle is assigned through a weighted average based on the density function W. Thus the total force $\mathbf{F}(\mathbf{x}_i)$ acting on a particle i is given by

$$\mathbf{F}(\mathbf{x}_i) = \sum_m W(\mathbf{x}_i - \mathbf{x}_m)\mathbf{f}_m\,, \tag{3.17}$$

where $\mathbf{f}_m$ is the force field in a given cell-grid m. To ensure momentum conservation, the $W(\mathbf{x})$ assignment function used during force computation must be the same as that used during mass assignment, otherwise a different assignment kernel could introduce spurious accelerations violating Newton's third law.

3.1.2 Tree algorithm

The Tree algorithm solves the N-body problem by recursively dividing the simulation domain into sub-domains (Tree nodes) with a hierarchical tree structure. This method approximates gravitational forces by hierarchically grouping distant particles and representing their collective influence through multipole expansions.

This reduces the required $N-1$ (per particle) partial forces computation for a direct-summation approach to an order of $O(\log N)$ computations.

The gravitational potential generated by the points inside a node is

$$\Phi(\mathbf{r}) = -G\sum_i \frac{m_i}{|\mathbf{r}-\mathbf{x}_i|}\,, \tag{3.18}$$

where $\mathbf{x}_i$ is the position of the i particle inside the node and $\mathbf{r}$ the position of the point where we want to compute the potential. This equation can be rewritten as

$$\Phi(\mathbf{r}) = -G\sum_i \frac{m_i}{|\mathbf{r}-\mathbf{s}+\mathbf{s}-\mathbf{x}_i|}\,, \tag{3.19}$$

considering $\mathbf{s}$ as the center-of-mass of the distant particle group. Expanding the denominator under the assumption $|\mathbf{x}_i - s| \ll |\mathbf{r} - \mathbf{s}|$

$$\frac{1}{|\mathbf{y} + \mathbf{s} - \mathbf{x}_i|} = \frac{1}{|\mathbf{y}|} - \frac{\mathbf{y} \cdot (\mathbf{s} - \mathbf{x}_i)}{|\mathbf{y}|^3} + \frac{1}{2} \frac{\mathbf{y}^T [3(\mathbf{s} - \mathbf{x}_i)(\mathbf{s} - \mathbf{x}_i)^T - (\mathbf{s} - \mathbf{x}_i)^2] \mathbf{y}}{|\mathbf{y}|^5} + \cdots \tag{3.20}$$

where $\mathbf{y} \equiv \mathbf{r} - \mathbf{s}$. Having carried out the expansion with respect to the center-of-mass $\mathbf{s}$ of the particle group, the dipole term $\frac{\mathbf{y} \cdot (\mathbf{s} - \mathbf{x}_i)}{|\mathbf{y}|^3}$ vanishes. The monopole is represented by the total mass $M = \sum_i m_i$, while writing the quadrupole tensor as

$$Q_{ij} = \sum_k m_k \left[3(\mathbf{s} - \mathbf{x}_k)_i (\mathbf{s} - \mathbf{x}_k)_j - \delta_{ij} (\mathbf{s} - \mathbf{x}_k)^2 \right] , \tag{3.21}$$

and neglecting higher order terms, the potential expansion becomes

$$\Phi(\mathbf{r}) = -G \left(\frac{M}{|\mathbf{y}|} + \frac{1}{2} \frac{\mathbf{y}^T \mathbf{Q}\, \mathbf{y}}{|\mathbf{y}|^5} \right) . \tag{3.22}$$

The acceleration of particles

$$a(\mathbf{x}) = -\nabla \Phi(\mathbf{x}) \tag{3.23}$$

can then be computed through differentiation. The monopole term yields:

$$-\nabla \left(\frac{GM}{|\mathbf{y}|} \right) = -\frac{GM}{|\mathbf{y}|^3} \mathbf{y} \tag{3.24}$$

while, for the quadrupole term, we obtain

$$-\nabla \left(\frac{G}{2} \frac{\mathbf{y}^T Q \mathbf{y}}{|\mathbf{y}|^5} \right) = -\frac{G}{2} \left(\frac{2Q\mathbf{y}}{|\mathbf{y}|^5} - \frac{5\mathbf{y}^T Q \mathbf{y}}{|\mathbf{y}|^7} \mathbf{y} \right) . \tag{3.25}$$

Combined together, the total acceleration can be computed as

$$a = -G \left(\frac{M}{|\mathbf{y}|^3} \mathbf{y} + \frac{Q\mathbf{y}}{|\mathbf{y}|^5} - \frac{5}{2} \frac{\mathbf{y}^T Q \mathbf{y}}{|\mathbf{y}|^7} \mathbf{y} \right) . \tag{3.26}$$

To compute the gravitational acceleration of a particle at position $\mathbf{x}$, the tree is walked starting from the root node (which contains all the particles) and dividing it into child nodes, each with half the side-length of the parent one. To determine whether to divide a given node into subnodes or evaluate its multipole expansion and stop walking along the corresponding branch, the code compares the angle subtended by the node with a pre-defined critical angle θ_c. Considering l the side-length of the node and r the distance, if

$$\frac{l}{r} < \theta_c \, ,$$

the gravitational contribution of particles within the considered node can be evaluated with a multipole expansion (so the node is not further divided). Changing the critical angle θ_c allows to control the accuracy of the force computation. When θ_c is small, more tree nodes must be opened and evaluated, reducing the residual force errors at the cost of increased computational effort. In the limiting case where $\theta_c \to 0$, the tree algorithm becomes equivalent to a direct summation method. Here, every particle-particle interaction is computed individually, eliminating approximation errors but incurring in the full $\mathcal{O}(N^2)$ computational cost.

3.1.3 Tree-PM

The primary advantage of the Particle Mesh (PM) method is its speed, as it reduces the computational cost per timestep from N^2 (for direct summations) to N.

However, the key disadvantage is the limited spatial resolution, constrained by the mesh size h. Consequently, any information at scales smaller than the mesh size is lost.

For the Tree algorithm, the spatial resolution is continuously adapted based on the clustering level. Furthermore, the accuracy of the force calculation can be tuned by modifying the tree opening angle, and the algorithm's speed does not strongly depend on the clustering level. However, the primary disadvantage arises in highly uniform matter distributions, as e.g. the matter density field at high redshifts. In such situations, the almost vanishing force on each particle is the result of the cancellation of many larger contributions. This needs substantial computational effort to achieve high accuracy in force calculations, making the process numerically expensive.

To combine the speed of the PM and overcome the latter disadvantage of the Tree, a combination of these two is often adopted. The basic concept is to split the potential in a short-range $\Phi_{\mathbf{k}}^{short}$ and a long-range component $\Phi_{\mathbf{k}}^{long}$ as

$$\Phi_{\mathbf{k}} = \Phi_{\mathbf{k}}^{long} + \Phi_{\mathbf{k}}^{short} \,. \tag{3.27}$$

The Tree method is used to evaluate the short-range component, where the Tree performs better, while the long-range is computed using the PM. The short-range component is multiplied by a smoothing function to suppress its contribution at long distances, the same is done to suppress short-range contributions for long-range component:

$$\begin{aligned} \Phi_{\mathbf{k}}^{long} &= \Phi_{\mathbf{k}} e^{\mathbf{k}^2 r_s^2} \,, \\ \Phi_{\mathbf{k}}^{short} &= \Phi_{\mathbf{k}} \left[1 - e^{-\mathbf{k}^2 r_s^2}\right] \,, \end{aligned} \tag{3.28}$$

where r_s is the spatial scale of the force-split. This force-shaping factor allows for the reduction of inaccuracies, such as force anisotropies arising from the mesh geometry, to arbitrarily small levels. Consequently, the long-range force

is accurately calculated by the PM scheme, even in the transition region between force components. Transforming back to real space equation 3.28, and assuming a single point of mass m in a box L with $r_s \ll L$, we get

$$\Phi^{short}(\mathbf{x}) = -G\frac{m}{r}erfc\left(\frac{r}{2r_s}\right), \tag{3.29}$$

where $erfc(x)$ represents the complementary error function defined as

$$erfc(x) = 1 - \frac{1}{\sqrt{\pi}}\int_{-x}^{x} e^{-t^2}dt^2\,. \tag{3.30}$$

This function is characterized by a smooth transition from 1 to 0 as x increases, ensuring a smooth cut-off of the short-range force at large distances. The short-range potential coincides with the Newtonian one up to truncation factor that rapidly turns off the force at distances of order r_s.

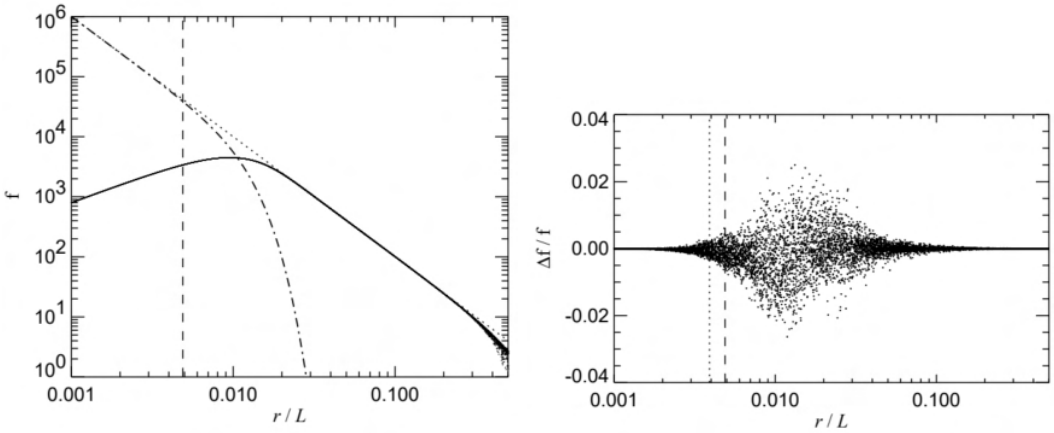

Figure 3.2: Force decomposition (left) and force error (right) in the Tree-PM scheme taken from Springel (2005). The position of the force-split scale r_s is marked by a dashed vertical line

As we will see in chapter 4, to incorporate the additional physics introduced by the Coupled Dark Energy models we aim to test, both the Tree and the PM algorithms must be modified. This is because a fundamental feature of Coupled Dark Energy models is the presence of a fifth force, which we implement by modifying the gravitational constant G. Consequently, both the Tree and the PM algorithms require adjustments, as the gravitational constant enters into the force calculation in both schemes.

3.2 Gadget-4

GADGET-4, (Springel et al., 2021), is a modern simulation code designed to model cosmic structure formation and galaxy evolution.

We decided to implement out modifications in Gadget-4 in this work, rather than its older versions, because it includes major advancements in high-precision large-scale structure simulations, along with improved modularity and flexibility.

Gadget-4 employs a TreePM method (see section 3.1.3) for gravitational forces, combining the high-resolution accuracy of a Tree algorithm with the efficiency of a long-range PM solver. The code operates in a Newtonian approximation and supports both periodic and non-periodic boundary conditions, making it suitable for cosmological simulations as well as isolated astrophysical systems.

A major advancement over its predecessor, GADGET-2 (Springel, 2005), GADGET-4 introduces significant improvements in force accuracy, time integration, and scalability. Key upgrades include:

- Modern, modular codebase (written in C++ with improved maintainability)
- Reduction of floating-point errors through the use of integer coordinates for particle positions
- Enhanced hydrodynamics with support for smoothed particle hydrodynamics (SPH)
- Optimized parallelization, allowing efficient runs on large supercomputing architectures

A significant advancement in GADGET-4 compared to its older versions is its shift from C to C++ as the primary programming language. While earlier versions relied on C for low-level control, the adoption of C++ enables modern object-oriented features, improving modularity and extensibility (Springel et al., 2021). This transition also facilitates more sophisticated memory management and parallelization techniques, which are crucial for large-scale cosmological simulations.

While these advancements enable more precise and efficient simulations, they also pose significant challenges for implementing extension modules developed for older versions. The fundamental changes in code structure, including the transition from C to C++ as code language and the consequent shift to an object-oriented design, prevent the direct porting of existing modules from previous versions (GADGET-2 and GADGET-3) designed for specialized physics (such as modified gravity or alternative dark energy models).

For this reason, the Coupled Dark Energy implementation already available in C-GADGET (a modified version of GADGET-3 code, as described in Baldi

et al. (2010)), cannot be trivially ported to GADGET-4. Adapting it requires substantial modifications to ensure compatibility with GADGET-4's new architecture.

To start a simulation in GADGET-4, a parameter file must be prepared, containing run-time parameters of the simulation setup such as initial conditions, output frequency, time integration settings, and numerical parameters for hydrodynamics and gravity solvers. This file dictates the fundamental properties of the simulation, including particle mass resolution, gravitational softening length, and cosmological parameters.

Additionally, a configuration script is required to set up the compilation environment. This script defines the necessary compilation flags such as type of boundary conditions employed (vacuum or periodic), physics included and so on. Notably, GADGET-4 allows users to enable comoving integration in this file. When activated, the simulation adopts comoving coordinates, simplifying cosmological simulations by factoring out the expansion of the universe.

The simulation outputs are stored at specified intervals, providing snapshots that contain the evolving cosmic structures, which can later be analyzed using post-processing tools.

GADGET-4 offers a LIGHTCONE output feature, which records particles at their exact positions and peculiar velocities when they intersect the backward lightcone during the simulation. This produces specialized output files, similar to snapshots but organized according to the lightcone crossing time. When activated through the configuration switch, users can specify maximum redshift and shell thickness parameters by setting the appropriate values in the parameter file. The LIGHTCONE_MASSMAPS option extends this functionality by generating mass shells specifically for weak lensing applications. It processes the lightcone particle data to create mass maps, which serve as essential input for weak lensing calculations, as we will see in Chapter 5.

GADGET-4 includes an advanced group finder algorithm to identify halos and substructures in simulation data. The algorithm combines two key methods:

- Friends-of-Friends (FoF): Links particles based on a user-defined linking length (typically a fraction of the mean interparticle separation) to identify halo candidates.

- SUBFIND: A substructure detection algorithm that decomposes FoF halos into gravitationally bound subhalos. SUBFIND identifies local density peaks and removes unbound particles, enabling the study of hierarchical structure formation.

The group finder operates on-the-fly during simulations or as a post-processing tool, supporting large datasets. These snapshots can be analyzed using post-processing tools such as Pylians3 (Villaescusa-Navarro, 2018), a powerful toolkit designed for cosmological simulations.

Pylians3 enables the computation of fundamental observables in large-scale structure studies, including density field, power spectrum, and Halo and Subhalo Properties. Figure 3.3 shows an example of how the density field evolves at different redshifts for our ΛCDM simulation, as extracted from the snapshot files using Pylians3.

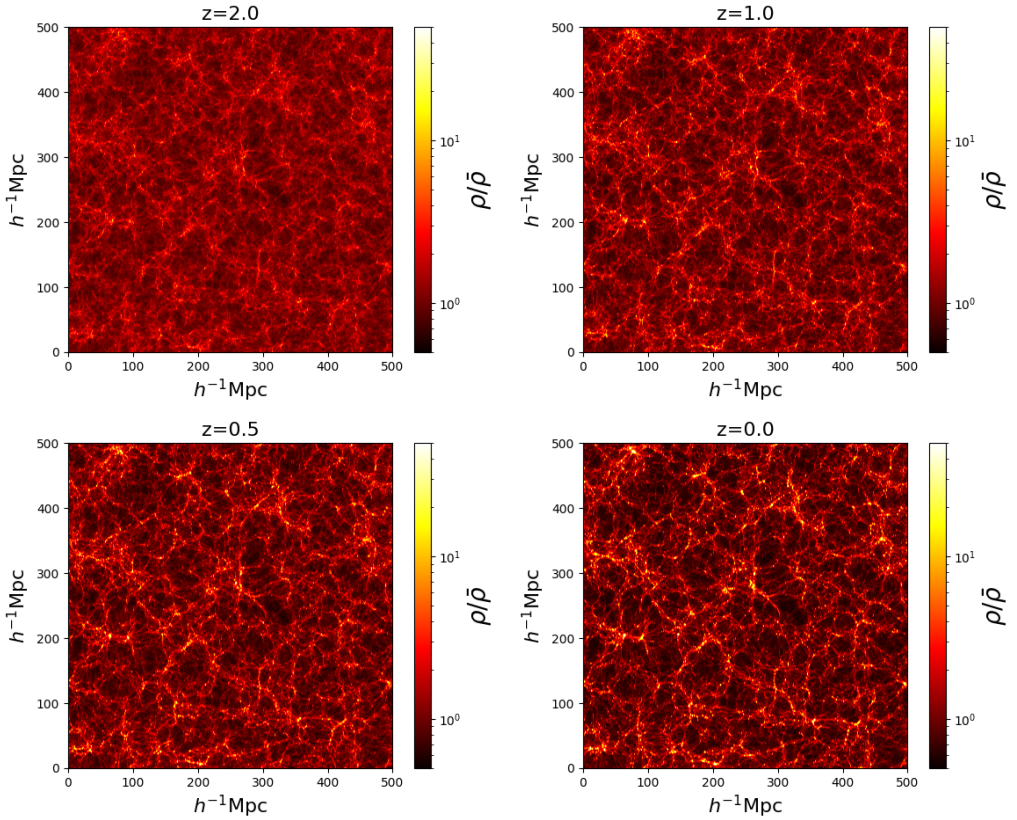

Figure 3.3: Density field in a slice of $500 \times 500\ Mpc/h$ and thickness $30\ Mpc/h$ extracted from our ΛCDM simulations at different redshift

Pylians computes the density contrast from simulation snapshot files by first selecting particles on a thin slab perpendicular to one axis to create a two-dimensional projection. The density field is computed by spreading particles masses onto a grid adopting a specified mass-assignment scheme (see section 3.1.1).

The local density in each grid cell is then compared to the average density across the entire volume to calculate the overdensity. This measures how much denser or emptier each region is compared to the cosmic average. We can appreciate from figure 3.3 how the density perturbations evolve across cosmic time, gradually forming the intricate cosmic web structure we observe at present time.

3.3 PANDA-GADGET-4

The aim of this thesis work is to investigate cosmological models beyond the standard ΛCDM framework. In particular, we are interested in alternative theories for cold dark matter (CDM) and the cosmological constant (Λ) that could potentially address the current observational challenges associated with the standard cosmological constant.

The `PANDA` (Parameterised dArk eNergy and moDified grAvity) extension of `GADGET-4` (Casalino & Baldi in prep.) introduces a parametrized implementation of dark energy and modified gravity models.

Unlike other methods that solve full field equations for specific theories, PANDA adopts a parameterized approach, including modifications of gravity by adding a dependence to time and space to the gravitational constant G, rather than treating it as a fixed constant. The main motivation behind this parameterized approach is its significantly lower computational cost compared to solving the coupled differential equations involving modified gravity fields.

In PANDA, Newton's constant G is replaced by a function $G_{eff}(t, \mathbf{x})$, dependent on time and space whose form is determined by the chosen MG or dark energy model. The main consistency constraint of the function is to obtain the gravitational constant when the gravity modification parameters mimic ΛCDM. This function G_{eff} enters both the Particle-Mesh (PM) and Tree-force calculations, ensuring self-consistent evolution of structure formation under the influence of beyond-ΛCDM physics.

PANDA's parametrized framework was designed for standard Dark Energy (DE) and Modified Gravity (MG) theories and could not simulate Interacting Dark Energy (IDE) models featuring non-universal coupling between dark energy and a specific matter species. In this work, we introduce a unified phenomenological approach that maps IDE onto an effective MG description. For instance, in coupled dark energy models, where dark energy interacts with dark matter, the scalar field's fluctuations can be recast as an effective modification of gravity.

In the case of Interactive Dark Energy models, the fluctuations of the scalar field can be written as a time-dependent coupling coefficient $\beta(t)$ times the gravitational potential. Since $\beta(t)$ is spatially homogeneous, it can be moved out of the gradient and the additional force on the particles reduces to the standard gravitational acceleration multiplied by some function of β.

This mapping, which we implemented in PANDA (as described in section 4), allows to simulate IDE models using the same parametrized framework developed for MG.

Currently, `C-GADGET` code (Baldi et al., 2010), a modified version of `GADGET-3` code, already includes an implementation of some IDE models. Our main goal is to extend this functionality to PANDA, which is built on the more advanced `GADGET-4` code. This decision is motivated by several reasons. First, `GADGET-4` offers significant improvements in computational efficiency, paral-

lelization, and numerical accuracy, making it better suited for the increasingly demanding simulations required by modern cosmology. Second, one of the main features of PANDA, already present in `C-GADGET`, is the possibility to read and implement in the simulation cosmological parameters, such as the Hubble function H and the dark energy parameter w_{DE}, from an external input table.

As we are going to see with greater focus in chapter 4, we can expand this function to implement the parameters needed to simulate a coupled dark energy cosmology, such as the coupling coefficient β, the particle mass variation coefficient Δm, the scalar field velocity $\dot{\phi}$. By doing so, we not only maintain consistency with existing implementations but also open the door to studying a wider range of interacting dark sector models. Finally, future observational surveys will require highly precise simulations to test alternative cosmologies against real data. `GADGET-4`'s improved performance and scalability make it the ideal platform for these challenges, ensuring that coupled dark energy models can be explored with the necessary detail and statistical precision. In particular the `LIGHTCONE` output available in `GADGET-4` makes these simulations efficiently comparable to observations from wide-field galaxy surveys as the lightcone data directly replicates the observational geometry of surveys. This capability makes PANDA a highly efficient tool for connecting theoretical predictions with forthcoming observational constraints on interacting dark energy models, further reinforcing our motivation to implement the Coupled Dark Energy framework from `C-GADGET` into `PANDA`.

Chapter 4

Numerical Implementation in PANDA-Gadget-4

The presence of a coupling between a DE scalar field ϕ and different cosmological species introduces some additional physical processes as described in Section 2.2. To extend the study of the evolution of cosmic structure formation for a coupled dark energy model into the non-linear regime, which requires numerical simulations, the `PANDA-GADGET-4` code has to be modified.

In this chapter, we present the modifications implemented in the PANDA version of `GADGET-4` to incorporate the physical processes associated with coupled dark energy models. These modifications, as described in chapter 2, focus on three main aspects :

- the particle mass variation induced by the coupling (equation 2.20),
- the extra friction term (equation 2.39),
- the fifth force contribution to particles gravitational acceleration (equation 2.39).

Additionally, we detail the setup process for generating the initial conditions consistent with coupled dark energy models, including the construction of input tables containing the relevant cosmological functions. This ensures that the simulations reflect the theoretical framework accurately from the beginning of the evolution. Finally, we present a validation test designed to verify the correctness and stability of our modifications. These tests compare the outputs of the modified code against known results performed in Baldi (2012). Once the code's accuracy is established, we describe the final simulations used to explore the impact of coupled dark energy on cosmic structure formation in the non-linear regime.

4.1 Input Table

To perform the calculations required by the new implementation, the code relies on a set of time-dependent variables. These are provided via an input table file containing:

- $H(a)$: the Hubble function,
- $\beta_c(a)$: the coupling coefficient for cold-dark-matter particles,
- $\beta_b(a)$: the coupling coefficient for baryonic particles, which is set to zero for the models under consideration,
- $\Delta m_c(a)$: the mass-variation coefficient for cold-dark-matter particles,
- $\Delta m_b(a)$: the mass-variation coefficient for baryonic particles, which is identically unity for the models under consideration,
- $\dot{\phi}$: the time derivative of the dark energy scalar field.

All of the above quantities are computed by a separate code that integrates the background equations (see Eq. 2.21) for a specific coupled dark energy model and generates the corresponding input tables (as described in chapter 5.1).

This design choice of keeping the background and linear perturbations integration external to `PANDA-Gadget` was made to avoid overloading the simulation code with additional time-consuming calculations.

At the beginning of each simulation run, our new implementation reads this input table to initialize all necessary variables. The option to use an external input table can be enabled in the configuration file, and the respective file-path in the parameter file. This design allows for flexibility in testing different models while keeping the main simulation code efficient. In order to smoothly evaluate these quantities at any time-step during the simulation, and provide accurate results even between the discrete set of points provided in the input table, i wrote new functions that employs cubic spline interpolation from the GNU Scientific Library (GSL (Galassi et al., 2002)).

4.2 Mass Variation

In section 2.2 we showed how the presence of a coupling between a Dark Energy scalar field and a given coupled matter species leads to an energy exchange which is dictated by a factor $\beta\dot{\phi}$ in equation 2.17. As a consequence, the mass of the coupled particle species is no longer constant but changes according to equation 2.20.

As we described in chapter 3.3, the main goal of this work is to include a treatment for coupled dark energy cosmology, already available in `C-GADGET`,

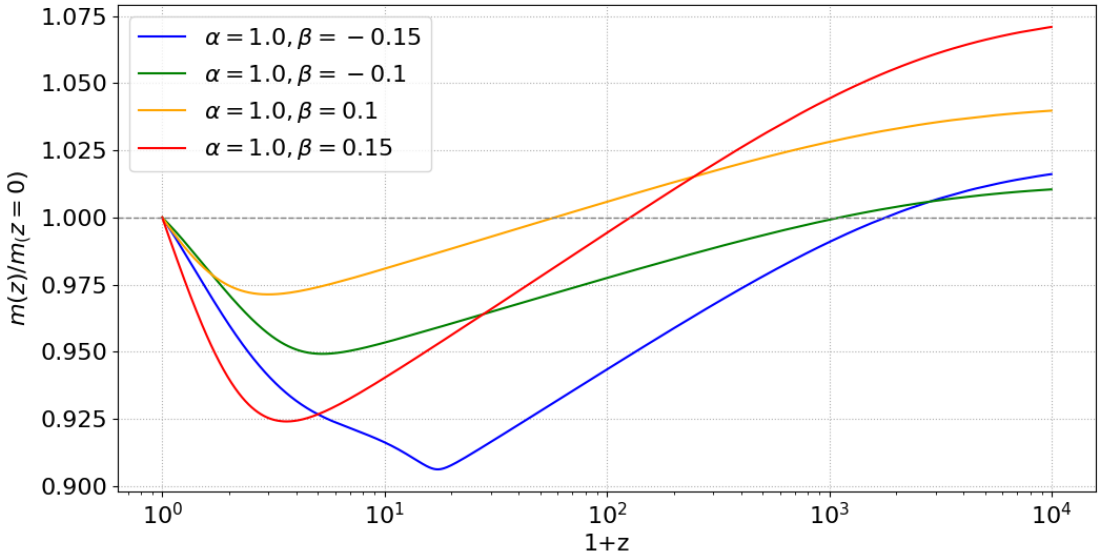

Figure 4.1: Evolution with redshift of the mass-variation coefficient of CDM particles for a coupled dark energy model featuring the same potential slope $\alpha = 1$ and different coupling strength β.

to the `PANDA` version of `GADGET-4`, extending the possibility of treating IDE models with the more sophisticated `GADGET-4` N-body code. For this reason, similar to `C-GADGET` (Baldi et al., 2010), the mass variation is implemented in `PANDA-Gadget` using a factor Δm computed from equation 2.20 as

$$\Delta m(a) = e^{-\sqrt{\frac{2}{3}}\int_a^1 \frac{\beta}{M_{Pl}}\frac{d\phi}{da}da} \,. \tag{4.1}$$

The code initially saves the original particle mass as m_0, i.e. the mass at present day, then at each timestep the particle mass is updated by multiplying the original mass by the time-dependent Δm factor, obtaining

$$\tilde{m}(a) = m_0 \cdot \Delta m(a) \,, \tag{4.2}$$

where $\tilde{m}(a)$ is the updated mass.

The coefficients $\Delta m(a)$ are obtained by numerically integrating the system of background equations 2.21, as we will explain in section 5.1, and are provided to the new `PANDA-Gadget` implementation as part of the input table, as described in section 4.1.

4.3 Cosmological extra velocity-dependent acceleration

An additional modification in the `PANDA-Gadget` code involves the velocity-dependent term present in equation 2.39, which, as shown in Baldi et al.

(2010), leads to the following relation

$$\tilde{H} = H\left(1 - \frac{\beta}{M_{Pl}}\frac{\dot{\phi}}{H}\right). \tag{4.3}$$

We can write the Hubble contribution to the particle acceleration as

$$\dot{v}_i = -H\left(1 - \frac{\beta}{M_{Pl}}\frac{\dot{\phi}}{H}\right)v_i\,. \tag{4.4}$$

As shown in chapter 3.2, in standard cosmological simulations, `Gadget4` does not compute the term $H\boldsymbol{v}$ due to the fact that the adoption of comoving coordinates removes it from the acceleration equation.

Here we address $\boldsymbol{r}, \boldsymbol{x}$ as the physical and comoving coordinates respectively, for which the following relation holds

$$\boldsymbol{r} = a(t)\boldsymbol{x} \quad \dot{\boldsymbol{r}} = H\boldsymbol{r} + \boldsymbol{v}_p\,, \tag{4.5}$$

with $\boldsymbol{v}_p \equiv a(t)\dot{\boldsymbol{x}}$ the peculiar velocity.

`Gadget`, however, instead of using the peculiar velocity $\boldsymbol{v}_p$ employs the variable $\boldsymbol{p} \equiv a^2(t)\dot{\boldsymbol{x}}$. In this way

$$\dot{\boldsymbol{v}}_p = \frac{1}{a}\dot{\boldsymbol{p}} - \frac{H}{a}\boldsymbol{p}\,, \tag{4.6}$$

and applying this relation to equation 4.4 we obtain that the extra acceleration due to this effect can be written as((Baldi et al., 2010)):

$$\dot{\boldsymbol{p}}_i = \beta_\alpha(\phi)\frac{\dot{\phi}}{M_{Pl}}\boldsymbol{p}_i\,, \tag{4.7}$$

where i represent the particle index, β_α represent the coupling strength of a given species α.

In case of zero-coupling $\beta_\alpha = 0$ the extra velocity-dependent term vanishes, resulting in a standard Newtonian acceleration in comoving coordinates.

For a coupled dark energy cosmological scenario, instead, the extra term $\beta_\alpha\frac{\dot{\phi}}{M_{Pl}}a\boldsymbol{p}_i$ has to be added to the Newtonian acceleration of each particle.

As already pointed out in Baldi et al. (2010), this extra term does not depend on any matter distribution but represents a purely cosmological drag that would be present even in the absence of any gravitational attraction.

As with mass variation (Section 4.2), this friction term depends on the factor $\beta\dot{\phi}$, meaning that its sign can change over time according to the evolution of the scalar field ϕ.

In this study, we consider a DE scalar field described by a SUGRA self-interacting potential, which starts from its minimum with $\dot{\phi} = 0$ (see Chapter 2).

In this scenario, the initial sign of the factor $\beta\dot{\phi}$ is positive for both positive and negative values of β (Section 2.3), resulting in a net acceleration of particles in the direction of their motion.

When the scalar field eventually reaches its inversion point, the scalar field velocity $\dot{\phi}$ changes sign, leading to $\beta\dot{\phi} < 0$.

At this point, the extra term in Equation 4.7 accelerates the particles in the opposite direction of their motion, effectively slowing them down.

As a result, this velocity-dependent term acts like a drag force in the early universe and as a frictional force at later times allowing to modulate the growth of structures in different epochs of the cosmic evolution.

4.4 Tree-PM Algorithm

One of the most crucial features in a coupled dark energy scenario is the modified gravitational interaction between particles. In this context, the gravitational interaction between two particles, labeled i and j, is described by a modified gravitational constant represented by:

$$\tilde{G} = G_N \cdot \left(1 + \frac{4}{3}\beta_i\beta_j\right), \tag{4.8}$$

where G_N is the standard Newtonian gravitational constant in the ΛCDM model and β_i , β_j are the coupling strength of particles i, j respectively (as we derived in section 2.4).

If either of the two interacting particles is uncoupled ($\beta = 0$), the extra force vanishes, and the gravitational interaction reduces to the standard Newtonian case as described in ΛCDM cosmology.

To reproduce this behavior in the numerical simulations, the code must be able to distinguish between different particle species during gravitational acceleration calculation, in order to assign the appropriate coupling coefficient β for each interaction.

As explained in the previous chapter, in the `Gadget-4` code the gravitational interaction is computed by means of a Tree-PM algorithm. Consequently, both the tree and the PM algorithms must be modified to consistently implement the gravitational dynamics of a coupled dark energy model.

4.4.1 Tree algorithm modifications

According to what discussed in chapter 3.1.2, in a standard Tree algorithm when the angular dimension of a given node is below the critical opening angle, the node is not further dived but its gravitational contribution is evaluated by multipole expansion. In standard `GADGET-4` each node carries information on the position of its center of mass and its total mass. This works fine in an uncoupled cosmological model because all particles interact with the same

gravitational constant. However, in the case of a species-dependent coupling among particles, the code needs to assign a different gravitational constant based on the interacting species. Therefore, the new implementation needs each particle to bring information on its own type and, in addition to the total mass and the total center of mass position, each node has to carry information about the center of mass position and total mass of each particle species separately.

To this end we modified the particle structure that contains all the particle information used by the code during the tree-walk, adding the information on the particle type. For the node, we included in the node structure also the information on the center of mass of each particle type which is evaluated at each time-step.

In this way, when computing the tree contribution to the particle acceleration, the new implementation is able to distinguish among different particle types, assigning the right coupling for each scenario

$$\dot{\mathbf{p}}_i = \frac{1}{a}\sum_{j\neq i}\frac{\tilde{G_{ij}} m_j \mathbf{x}_{ij}}{|\mathbf{x}_{ij}|^3} = \frac{1}{a}\sum_{j\neq i}\frac{(1+\frac{4}{3}\beta_i\beta_j) G m_j \mathbf{x}_{ij}}{|\mathbf{x}_{ij}|^3}\,. \tag{4.9}$$

Again, we followed the same approach as in `C-GADGET` implementation (Baldi et al., 2010), extending it to the PANDA version of `GADGET-4`.

4.4.2 PM algorithm modifications

Recalling what discussed in section 3.1.3, in a Tree-PM algorithm the long-range part of the gravitational force is computed evaluating the density distribution on a cubic grid and passing to Fourier space in order to calculate the force on the grid. First, the mass of each particle is spread out over nearby grid cells, adopting a mass-assignment scheme to create a smooth density field. Next, this density is converted into Fourier space, where the gravitational potential can be computed easily with equation 3.16. Once the potential is found, it is transformed back into real space, the forces on the grid are calculated and interpolated back to the individual particle positions.

Considering that the gravitational interaction of each particle species depends on its coupling coefficient β, the PM procedure is repeated as many times as there are coupled particles with different coupling functions.

At each repetition of the PM the code selects only one particle type (the one matching the type selected by the given repetition) computing the gravitational force grid only of one particle type at time. The total force is then built by adding the contribution of different partial force grids, one for each coupling type, each multiplied by the factor $\frac{4}{3}\beta_i\beta_j$ as

$$\dot{\mathbf{p}}_i = \left(1 + \sum_j + \frac{4}{3}\beta_i\beta_j\right)\dot{\mathbf{p}}_i^0\,, \tag{4.10}$$

where the sum on j account for all the different grids, β_j is the coupling of particles contained in the j grid, $\dot{\mathbf{p}}_i^0$ represents the pm-acceleration for a particle of type i of the standard `GADGET-4` code which is computed as we explained in section 3.1.1.

4.5 Initial Conditions

The setup of initial conditions in a cosmological N-body simulation requires defining the initial positions and velocities of all particles within the simulation volume at the starting redshift z_i of the simulation. Typically, this initialization follows a random-phase realization of the power spectrum corresponding to the chosen cosmological model, based on the Zel'dovich approximation (Zel'dovich, 1970). The power spectrum normalization is determined to match the expected σ_8, the root-mean-square fluctuations computed with a top-hat filter with radius $R = 8\,h^{-1}Mpc$, at a reference redshift, commonly taken as z = 0.

In this work, we adopt the same power spectrum for both CDM and baryon particles and for all models under investigation, discarding possible distortions of the transfer function due to early effects of the coupling. This approach implicitly assumes that the coupling between dark energy (DE) and cold dark matter (CDM) does not modify the shape of the initial matter power spectrum. As such, we neglect any early-time effects of the coupling on the statistical properties of the density field. This approximation is generally justified, since in all models considered, the coupling effects remain small at high redshifts.

For all the simulations that we will employ in this work we generate initial conditions at $z_i = 99$ using N-GenIC code (Springel, 2015) to displace an initial *glass* distribution (White, 1994). First, we set the amplitude of the displacements at z_{CMB} to the same value for all models, ensuring consistency with CMB observations. We then rescale these displacements by the linear growth factor D_+, evaluated for each specific model between z_{CMB} and $z_i = 99$, to correctly set the initial power spectrum amplitude at the simulation's starting redshift. In this way, only the ΛCDM model will match the reference σ_8 value at $z = 0$, while the alternative (BCDE) models will deviate due to their distinct growth histories.

The power spectrum at the initial redshift of the simulation is computed using CAMB (Code for Anisotropies in the Microwave Background, (Lewis et al., 2000)) through a python script assuming a ΛCDM cosmology.

The cosmological parameters used for CAMB and for the final simulations are the one from Planck-2018 data release (Aghanim et al., 2020) and listed in table 5.1.

Once particles positions have been assigned, velocities are computed in Fourier space according to the linear perturbation theory relation $v(k, a) \propto$

$\frac{dlnD_+}{dlna}$ defined by the growth rate function for each model (Baldi, 2012).

4.6 Code Validation

In this chapter we have described the implementations applied to the `PANDA-GADGET-4` code to enable the simulation of a Coupled Dark Energy model. We now proceed with validating the code before analyzing the models of interest. To assess the accuracy of our implementation, we select some models present in the CoDECS project (*COupled Dark Energy Cosmological Simulations*), presented in Baldi (2012). We simulate these models using our new implementation in `PANDA-GADGET-4`, adopting different boxsize particle numbers compared to those used in Baldi (2012), and compare the results with the same models, run with the same parameters, simulated using the already validated `C-GADGET` code. Despite the presence of baryonic particles these simulations do not include hydrodynamics and are, therefore, purely collisionless N-body runs. In particular, we are going to test the EXP003 model which is described by

- an exponential potential $V(\phi) = Ae^{-\alpha\phi}$,
- with a slope $\alpha = 0.08$,
- constant $\beta_b = 0$, $\beta_c = 0.15$,
- potential normalization $A = 0.0218$,

resulting in cosmological parameters consistent with WMAP7 (Komatsu et al., 2011).

Firstly we generate the initial conditions using N-GenIC code (Springel, 2015), following the procedure described in section 4.5, and using the input tables obtained by integrating the background equations 2.21, as detailed in4.1, for the EXP003 models. Then we run the simulations with both `C-GADGET` and our newly implemented version of `PANDA-GADGET`, using the same initial conditions and input tables.

The simulations have been carried out using 2×256^3 particles in a comoving box of $240\,h^{-1}Mpc$.

In order to compare the results between `C-GADGET` and `PANDA`, we compute the nonlinear power spectrum of the matter distribution (CDM and baryons) from the respective snapshot files. This is done using the `Pylians3` Python library (Villaescusa-Navarro, 2018), which we use to extract the power spectrum from the simulation data. Starting from the snapshot file, we determine the density field on a grid employing a CIC assignment scheme, as described in section 3.1.1. Having computed the density grid we are able to evaluate the power spectrum as a function of the wavenumber k with the procedure described in section 1.9.

The maximum wavenumber that can be accurately resolved by the grid is defined by the Nyquist frequency $k_{Ny} = \frac{\pi N}{L}$, which for a number of 256^3 grid cells in a $240\,h^{-1}Mpc$ Boxsize corresponds to $k_{Ny} \sim 3.4\,h\,Mpc^{-1}$.

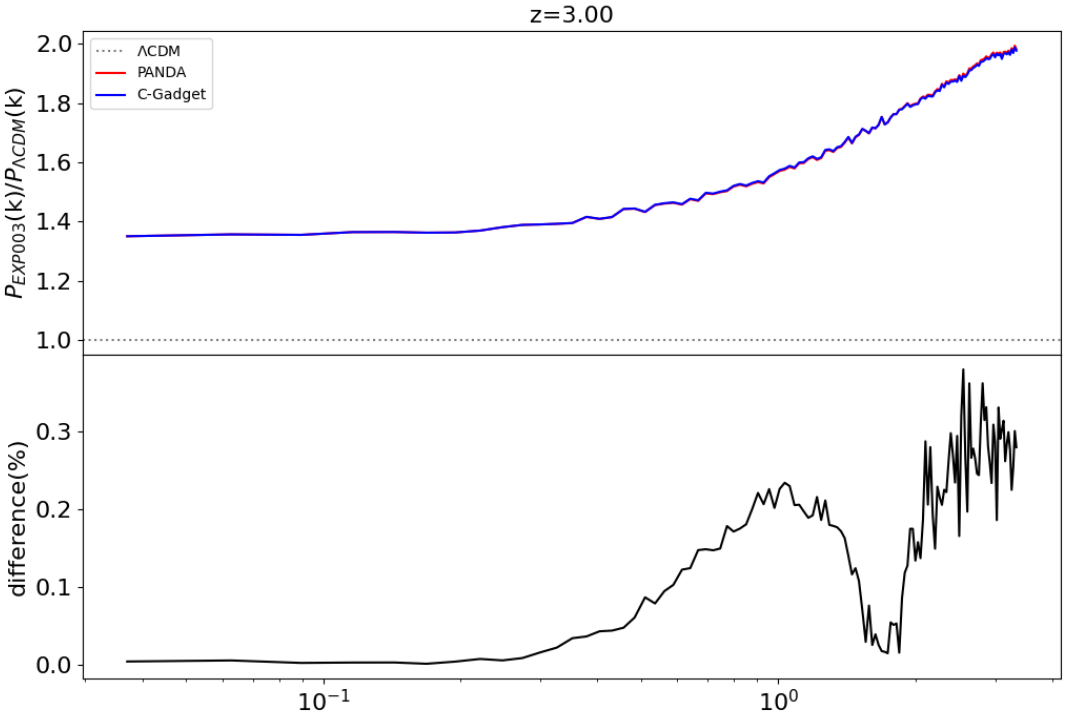

Figure 4.2: *Upper panel*: Power spectrum ratio of the EXP003 model with respect to ΛCDM, for our modified `PANDA` code vs. `C-Gadget` code for z=3. *Bottom panel*: Percentage difference between `PANDA` and `C-Gadget` power spectrum ratio.

The figures 4.2, 4.3, and 4.4 show the power spectrum of the EXP003 model, compared to the fiducial ΛCDM model. These results were obtained from simulations run using both C-GADGET and our modified PANDA version of the GADGET-4 code at redshifts $z = 3$, 1, and 0, respectively.

In the upper panels of these figures, the ratio of the EXP003 power spectrum to that of ΛCDM is shown for both PANDA and C-GADGET. The lower panels display the percentage difference between PANDA and C-Gadget power spectrum ratio.

As shown, the deviation of our PANDA implementation relative to the previously validated C-GADGET code (Baldi et al., 2010) does not exceed the 1% level, indicating good agreement between the two codes.

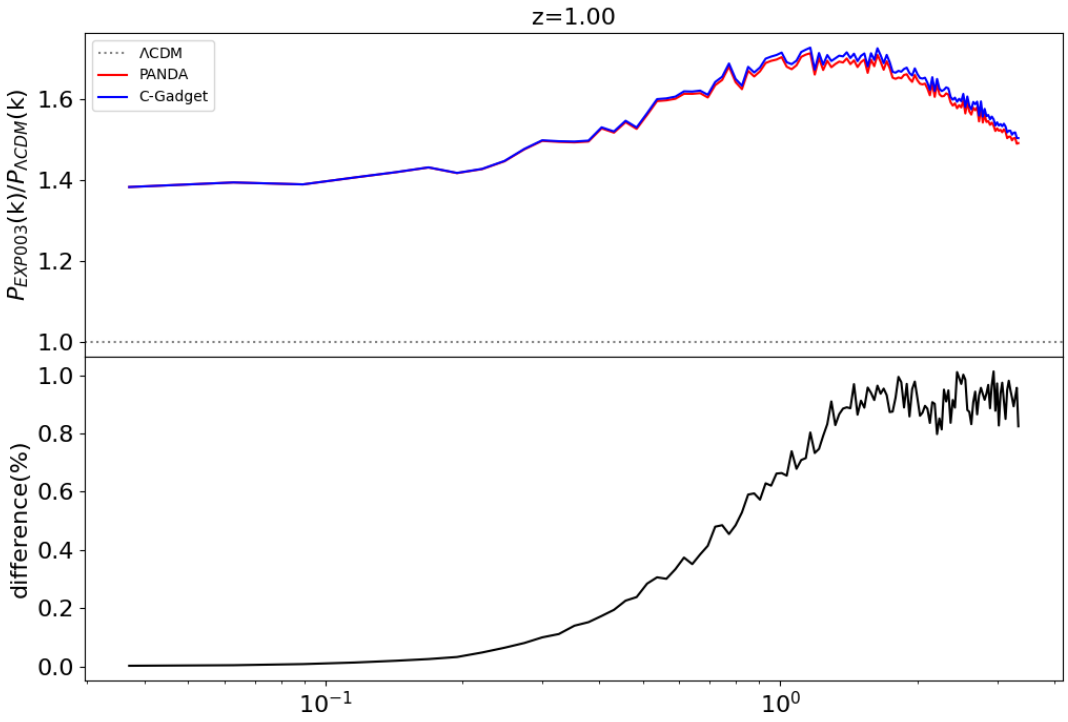

Figure 4.3: *Upper panel*: Power spectrum ratio of the EXP003 model with respect to ΛCDM, for our modified `PANDA` code vs. `C-Gadget` code for z=1. *Bottom panel*: Percentage difference between `Panda` and `C-Gadget` power spectrum ratio.

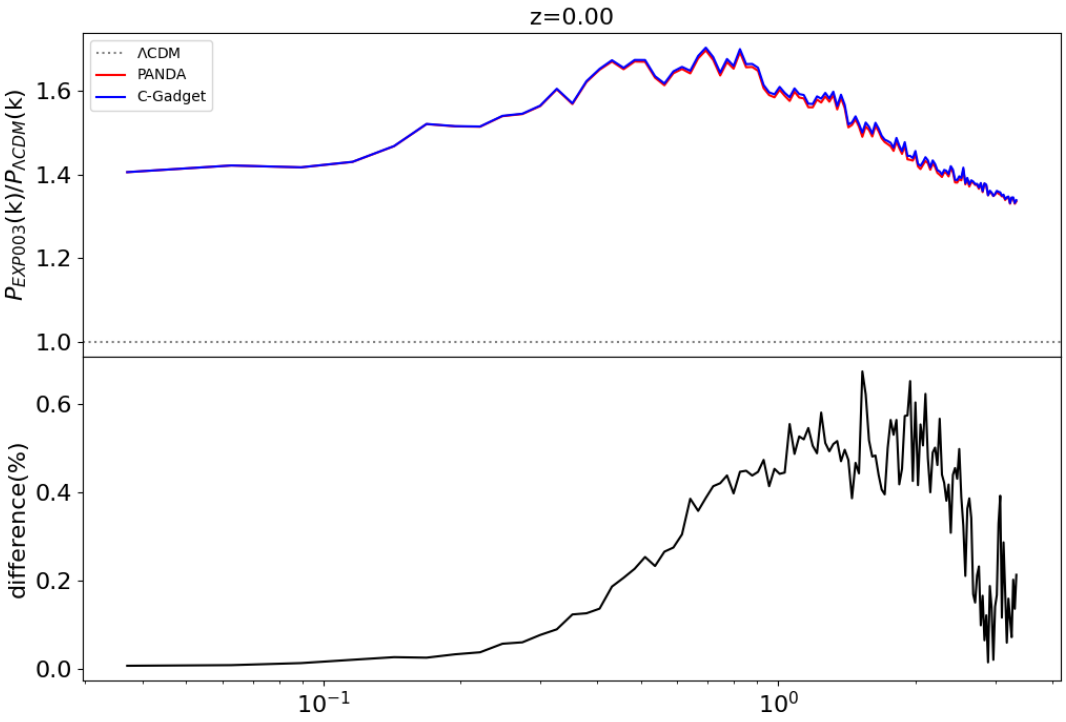

Figure 4.4: *Upper panel*: Power spectrum ratio of the EXP003 model with respect to ΛCDM, for our modified PANDA code vs. C-Gadget code for z=0. *Bottom panel*: Percentage difference between Panda and C-Gadget power spectrum ratio.

Chapter 5

Background and structure formation observables from simulated BCDE models

In this chapter, we present a comprehensive study of BCDE models, combining background and linear perturbations analysis with cosmological simulations to investigate their impact on the large-scale structure of the Universe. The investigation is divided into two main parts: first, in section 5.1, we examine the background evolution and linear perturbations of these models to assess their viability and phenomenology at large scales; second, in section 5.3, we analyze their nonlinear effects through numerical simulations.

As described in previous chapters, the presence of a coupling β introduces distinctive physical effects, including a velocity-dependent friction term, an effective fifth force and a mass evolution of coupled particles. Using the numerical code introduced in section 4.1, we integrate the complete system of background equations (eqs. 2.21) and linear perturbation equations (eqs. 2.37, 2.38). The results of this integration are presented in section 5.1, where we analyze how different parameter combinations (α, β_c) affect both the Hubble function and the matter growth factor $D_+(a)$, with particular attention to their potential to alleviate current cosmological tensions.

These models are then simulated with our modified version of the `PANDA-Gadget4` code, which includes the necessary modifications to account for the BCDE scenario (as described in chapter 4). This allows us to extend the study of BCDE cosmology into the non-linear regime of structure formation.

Finally, section 5.3 presents the results of these simulations. By analyzing matter statistics (the Power Spectrum), halo statistics (such as the Halo Mass Function) and weak lensing predictions, we quantify how BCDE models deviate from the standard ΛCDM paradigm.

It is important to remember that BCDE models represents just one particular example of the broader class of IDE models that can be simulated with our newly developed implementation in `PANDA-GADGET-4`. This panoramic

approach not only tests the theoretical consistency of BCDE but also demonstrates the flexibility of our framework in studying generic coupled dark energy scenarios. The pipeline, combining background and perturbation analysis, nonlinear simulations with our new version of `PANDA`, and weak lensing predictions with `DORIAN`, provides a viable methodology to constrain a wide range of IDE models with current and future cosmological surveys

5.1 Analysis of Dark Energy Models

As we discussed in section 2.4, the background evolution of the scalar field ϕ and the presence of a coupling between DE and other matter components directly affect the Hubble expansion rate H, the strength of the gravitational interaction, and the mass of particles coupled with the DE scalar field.

In this work, we focus on the study of BCDE models, characterized by a SUGRA self-interacting potential $V(\phi) = A\phi^{-\alpha}e^{\phi^2/2}$ and a constant coupling coefficient β_c. As described in section 2.3, we assume that the coupling between baryonic matter and DE scalar field is identically zero. We will investigate the model for various combinations of the coupling strength β_c and the self-interaction potential slope α.

We explored such dark energy models by employing a code which numerically integrates the background and linear perturbations equations of a BCDE model, with a SUGRA potential and thus with a global minimum in $\phi_m = \sqrt{\alpha}$. The models of interest were subsequently simulated using the coupled dark energy implementation of the `PANDA-Gadget4` N-body code (see chapter 4).

For the reference ΛCDM model, we consider cosmological parameters in agreement with the results of Planck-2018 (Aghanim et al., 2020) which are listed in table 5.1

Parameter	Value
H_0	67.36
Ω_b	0.0493
Ω_c	0.2645
Ω_{DE}	0.6847
σ_8	0.811
n_s	0.9649
z_{eq}	3402

Table 5.1: Cosmological parameters at z=0 listed in Aghanim et al. (2020)

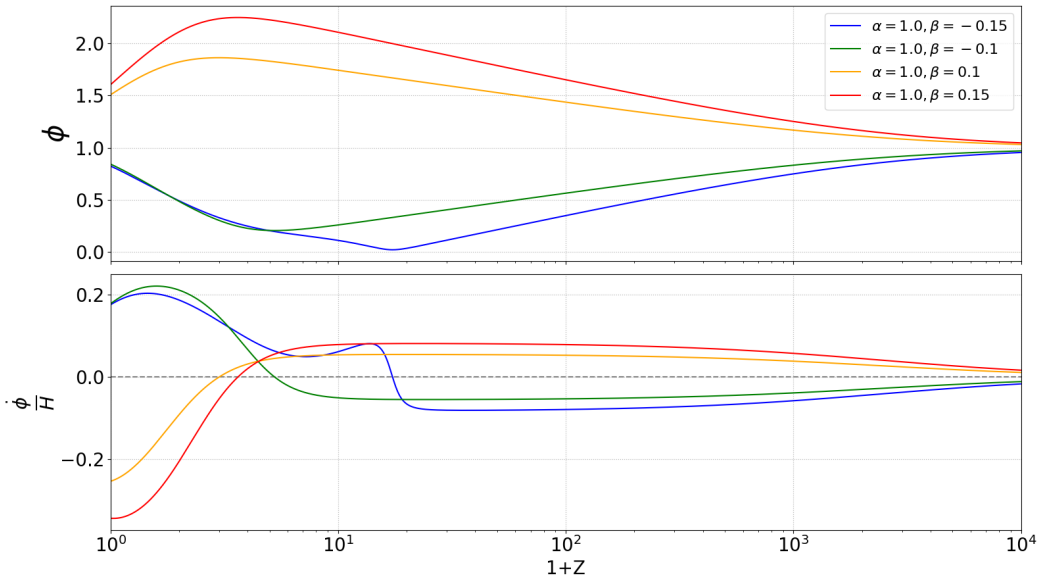

Figure 5.1: Evolution of the scalar field ϕ (*Top panel*) and the scalar field velocity $\dot{\phi}$ (*Bottom panel*) as a function of redshift for different Bouncing Dark Energy models with the same slope $a = 1$ and different values of the coupling β_c. The scalar field velocity is per unit of $\sqrt{6}M_{Pl}$, consistently with the definition of x in equation 2.26

.

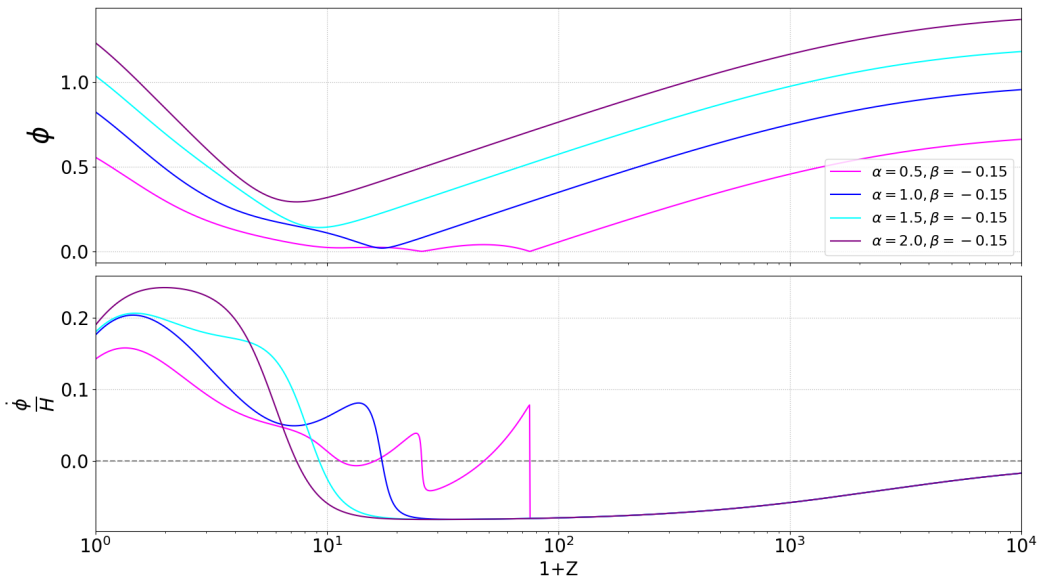

Figure 5.2: Evolution of the scalar field ϕ (*Top panel*) and the scalar field velocity $\dot{\phi}$ (*Bottom panel*) as a function of redshift for different Bouncing Dark Energy models with the same coupling $\beta = -0.15$ and different values of the slope α. The scalar field velocity is per unit of $\sqrt{6}M_{Pl}$, consistently with the definition of x in equation 2.26

.

In figure 5.1 we show the evolution of the scalar field ϕ and its velocity $\dot{\phi}$ as a function of redshift for different choices of the coupling strength β_c. All these models start from the same minimum point $\phi_m = \sqrt{\alpha} = 1$, then, as soon as the CDM density ρ_c becomes significant, the scalar field starts to accelerate according to equation 2.25. The value of the coupling strength β_c has a strong impact on the evolution of the scalar field. For models with $\beta_c > 0$, the positive coupling pushes the field away from its initial position ϕ_m in the direction of larger field values, i.e. toward the exponential side of the SUGRA potential. Conversely, for $\beta_c < 0$, the field moves toward smaller field values in the direction of the power-law side of the potential.

Figure 5.2, instead, displays the evolution of the scalar field ϕ and its velocity $\dot{\phi}$ for models with negative coupling strength $\beta_c = -0.15$ and different values of the slope α. First, we can notice that the starting point ϕ_m, corresponding to the minimum value of the self-interaction potential, for models with $\alpha = 2.0$ is higher with respect to previous models, as for $\alpha = 2.0$ $\phi_m = \sqrt{\alpha} \simeq 1.41$

Since the field moves away from its local minimum point ϕ_m, the scalar velocity term $3H\dot{\phi}$ and the potential derivative $\frac{dV}{d\phi}$ grows larger, slowing the field evolution until it eventually stops and inverts its motion towards the minimum point. This peculiar evolution of a coupled SUGRA scalar field has an important impact on the growth of density perturbations, as we will show in section 5.3.

It is interesting to note that, unlike other models where the scalar field velocity increases after the inversion point until reaching a maximum at late times, the models with $\beta = -0.15$ $\alpha = 0.5$, 1.0 exhibits a different behavior. For the $\alpha = 1.0$ case, the scalar field velocity begin to decrease shortly after the inversion point, before resuming to grow toward the global peak. This results in a characteristic small bump in the velocity evolution prior to reaching the maximum. Even more interesting is the behavior of the $\alpha = 0.05$ model, which, differently to other models, exhibits multiple bounces, before the scalar field starts to roll back toward the minimum point. These multiple bounces arise when the low values of α allowa the scalar field to approach $\phi = 0$ before being bounced back. Such behavior results in a scalar field inverting its motion multiple times before starting to finally roll back towards its equilibrium point.

By comparing the evolution of the particles mass variation, in figure 5.3, with the scalar field velocity $\dot{\phi}$ for each model, we clearly observe that the minimum of the mass variation occurs precisely when the BCDE model crosses $\dot{\phi} = 0$, i.e., at the inversion points.

This behavior can be explained by considering the dynamics of momentum conservation. When the mass decreases (i.e., when $\beta\dot{\phi} > 0$ at early times), momentum conservation imposes an additional acceleration in the direction of the particles motion. This corresponds to the extra anti-friction term, which will be discussed in Section 4.3. Conversely, after the inversion point, when the mass begins to increase and $\beta\dot{\phi} < 0$, momentum conservation leads to

an additional acceleration that opposes the particles motion, leading to an effective friction.

To investigate the background evolution and structure formation in the linear regime of such BCDE models, we numerically integrate the set of dynamic equations described in section 2.3.

$$\ddot{\phi} + 3H\dot{\phi} + \frac{dV}{d\phi} = \sqrt{\frac{2}{3}}\beta_c \frac{\rho_c}{M_{Pl}}\,, \tag{5.1}$$

$$\dot{\rho}_c + 3H\rho_c = -\sqrt{\frac{2}{3}}\beta_c \frac{\rho_c \dot{\phi}}{M_{Pl}}\,, \tag{5.2}$$

$$\dot{\rho}_b + 3H\rho_b = 0\,, \tag{5.3}$$

$$\dot{\rho}_r + 3H\rho_r = 0\,, \tag{5.4}$$

$$3H^2 = \frac{1}{M_{Pl}^2}(\rho_c + \rho_b + \rho_r + \rho_\phi)\,, \tag{5.5}$$

along with the perturbations equations discussed in section 2.4

$$\ddot{\delta}_c = -2H\left[1 - \beta_c \frac{\dot{\phi}}{H\sqrt{6}}\right]\dot{\delta}_c + 4\pi G\left[\rho_b\delta_b + \rho_c\delta_c\Gamma_c\right]\,, \tag{5.6}$$

$$\ddot{\delta}_b = -2H\dot{\delta}_b + 4\pi G\left[\rho_b\delta_b + \rho_c\delta_c\right]\,. \tag{5.7}$$

The integration is performed in two stages to ensure consistency with the present-day cosmological observations. In the first stage, we perform a backward integration from the present epoch (z = 0) to high redshifts, within the ΛCDM framework. This step determines the high-redshift values of the cosmological variables that correspond to the desired present-day parameters within the reference ΛCDM model.

Using the high-redshift values obtained from the first stage as initial conditions, we perform a forward integration for all the interacting dark energy models. This provides a complete evolutionary history of all relevant quantities, which we record at fixed time intervals The output includes both background quantities and perturbation variables. The input tables we introduced in section 4.1 are generated in this stage. The necessity for a first backward integration stage arises from the fact that the initial values depend sensitively on the specific present-day parameters. In this way the preliminary backward integration ensure that the initial conditions for the forward integration are compatible with the present day observations, before proceeding with the second forward integration.

To compare the different behavior of each model in the growth of perturbations, we normalize the growth factor, presented in the lower panel of figure 5.4, to the same value of ΛCDM at $z_{CMB} \simeq 1100$.

In the upper panel of figure 5.4 we show the evolution of the Hubble function ratio to the ΛCDM reference, for models with different couplings β_c,

as a function of redshift. We first note that the Hubble function is enhanced by up to a factor ~ 1.2 compared to the standard ΛCDM at $z = 0$, while rapidly decreases below the ΛCDM level at higher redshift. This particular behavior may help mitigating the Hubble tension seen in chapter 1.11.2 as H transitions from a larger than ΛCDM value at low redshifts to lower values at higher redshifts.

Simultaneously, as illustrated in the lower panel of figure 5.4, the growth factor initially increases with respect to the standard ΛCDM model at early times, but then reaches a turning point and begins to decrease sharply. This leads to a growth factor that, at $z = 0$, is more than 10% lower than in the ΛCDM case for $\beta_c = 0.15$.

In figure 5.5, models with $\alpha = 2.0$ exhibit a slightly stronger increase in H_0 and a more pronounced decrease in the growth factor ratio at $z = 0$, compared to the $\alpha = 1.0$, $\beta = -0.15$ case, though still not as extreme as the $\beta = 0.15$ scenario.

Therefore, these models predict a higher Hubble function at $z = 0$ while simultaneously exhibiting a lower growth factor at low redshifts.

These results are particularly intriguing because they highlight how BCDE models, with an appropriate choice of the α and β parameters, may simultaneously alleviate both the Hubble tension and the S_8 tension.

Now we will see the effect of a BCDE scenario on the evolution of the density parameters Ω.

The evolution, as function of redshift, of density parameter Ω for matter, radiation, and DE is shown in figures 5.6, 5.7.

We can notice that the equivalence between matter component Ω_m and DE Ω_{DE} is shifted towards earlier times with respect to the ΛCDM case (dashed line). This can be expected if one considers the mass transfer between coupled particles, CDM in our case, and DE scalar field described in eq. 2.20 which leads to a decreasing CDM particle mass in favor of the DE field. Of course this effect depends on the the factor $\beta_c\dot{\phi}$ as described in 2.20.

For both positive and negative couplings β_c the factor $\beta\dot{\phi}$ is initially positive, leading, for both cases, to an earlier matter-DE equivalence.

While the dark matter–dark energy (DM–DE) equivalence is shifted toward earlier times, the radiation–DM equivalence is not and remains approximately at the same redshift as in the ΛCDM case, thereby not spoiling observations at high redshifts.

There are a few reasons for this. First, as shown in Section 2.2, photons are uncoupled from the DE scalar field, so their energy density evolves as in standard ΛCDM cosmology. However, since cold dark matter (CDM) is coupled to DE, one might expect a shift in the radiation–matter equivalence due to the mass loss of CDM particles. In our work, however, we consider relatively weak coupling strengths ($\beta \leq |0.15|$). Moreover, the equivalence occurs at early times ($z_{\rm eq} \sim 3400$), when the effects of the coupling are not yet significant. As a result, the radiation–DM equivalence remains largely

unaffected.

In this section, we have investigated the cosmological evolution of Bouncing Coupled Dark Energy models, introduced in Chapter 2, focusing on their behavior within the background and the linear regime. By analyzing the background expansion and the growth of linear perturbations, we have identified key features of these models, such as their ability to simultaneously impact the Hubble parameter H and the growth factor, potentially offering a resolution to both the Hubble and S_8 tensions discussed in section 1.11.2.

However, the linear analysis presented here is limited to large cosmological scales, where perturbations remain small. To extend our investigation into the non-linear regime, where structure formation occurs, we will simulate these models using our modified version of the `PANDA-Gadget4` N-body code, described in Chapter 4. This enhanced version, includes a self-consistent implementation of several interacting DE models, including the BCDE scenario discussed in this chapter, that we will use as a testbed for our new N-body implementation.

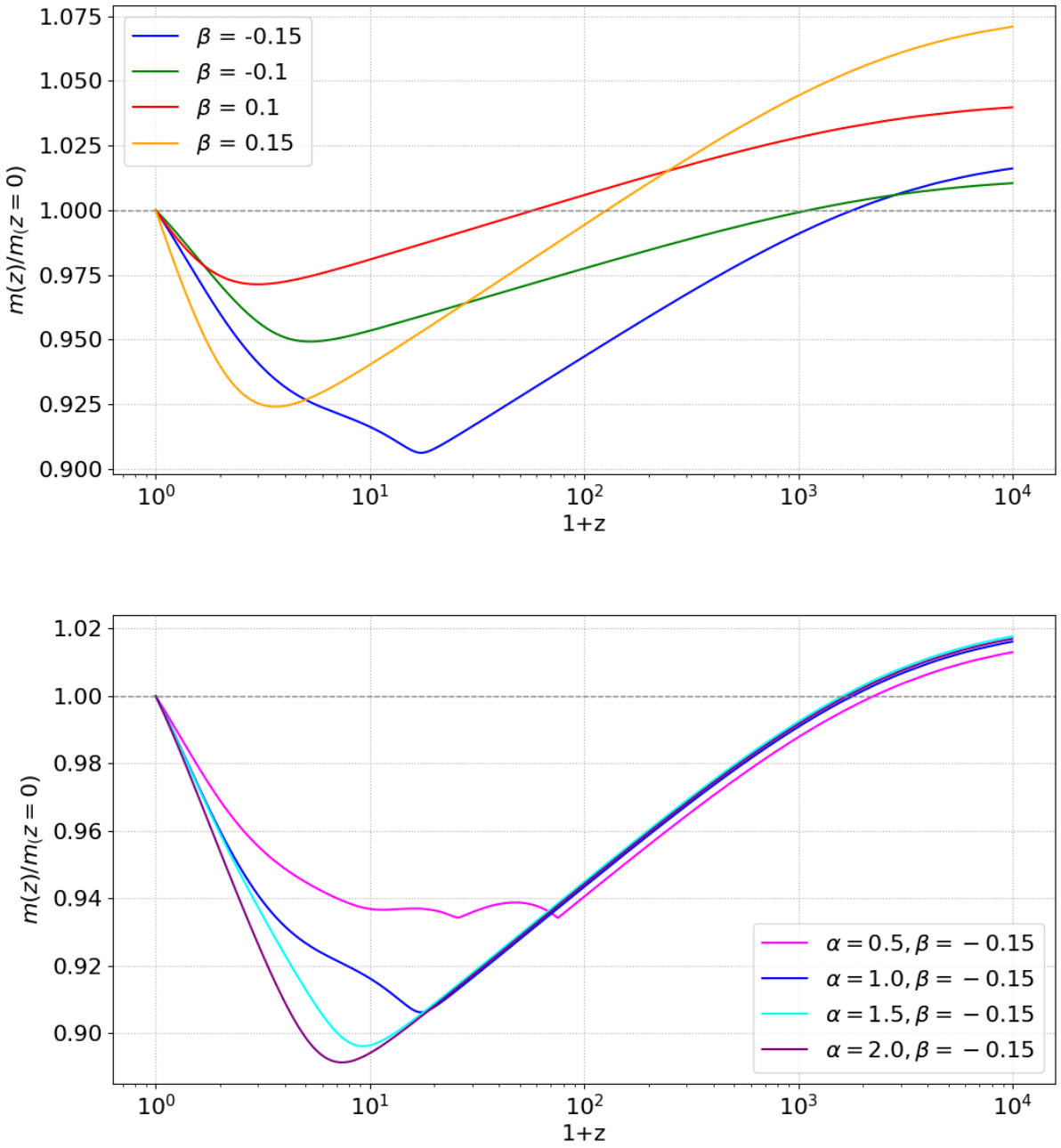

Figure 5.3: Evolution of the particle mass variation as function of redshift for BCDE models with the same slope $\alpha = 1.0$ and different values of the coupling β_c (*Upper panel*) and for BCDE models with the same negative coupling $\beta = -0.15$ and different values of the slope α (*Bottom panel*).

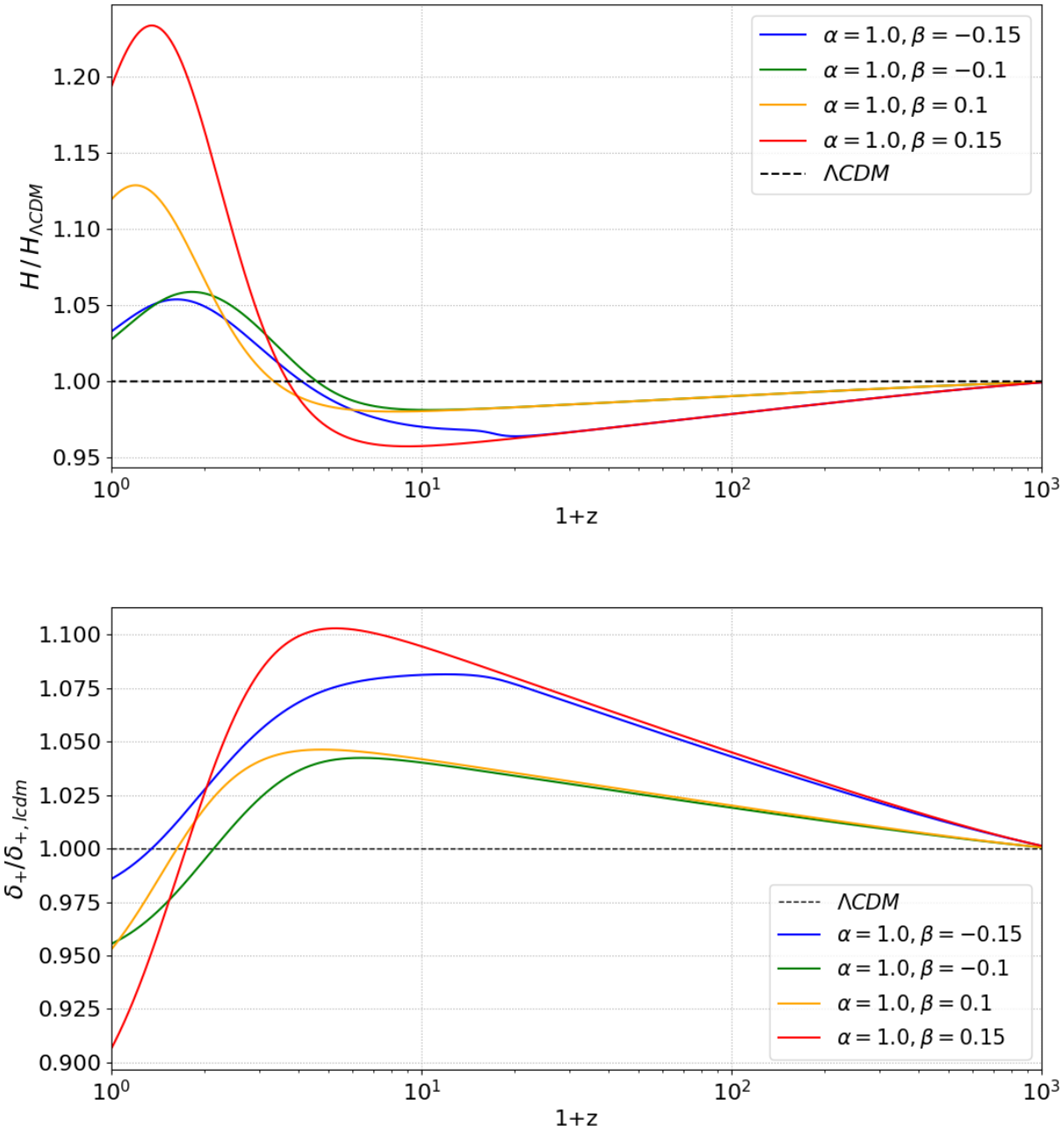

Figure 5.4: Evolution of the Hubble function H (upper panel) and growth factor δ_+ (bottom panel) as function of redshift of Bouncing Dark energy models, with the same $\alpha = 1$, compared to standard ΛCDM model.

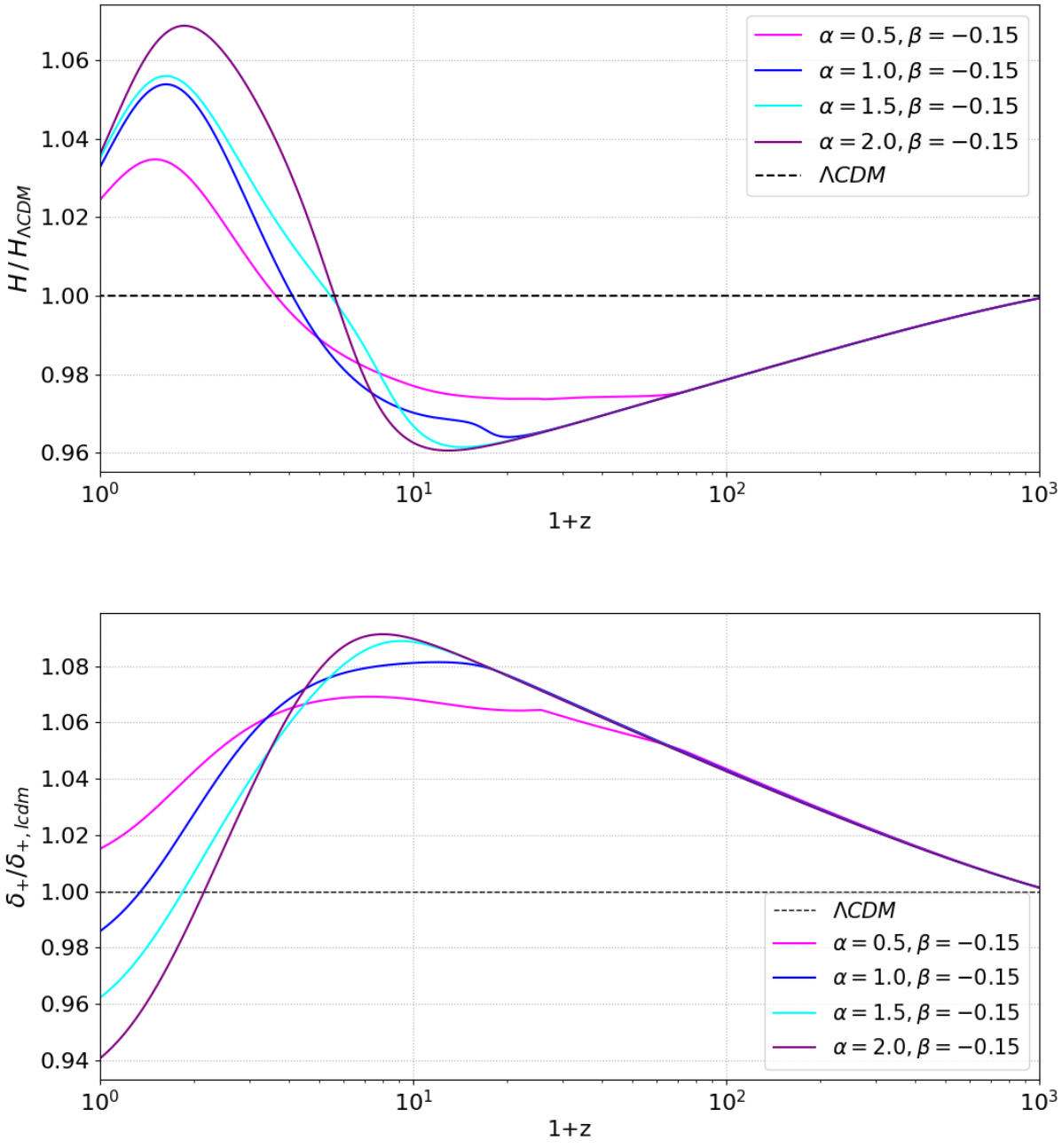

Figure 5.5: Evolution of the Hubble function H (upper panel) and growth factor δ_+ (bottom panel) as function of redshift of Bouncing Dark energy models, with the negative β, compared to standard ΛCDM model.

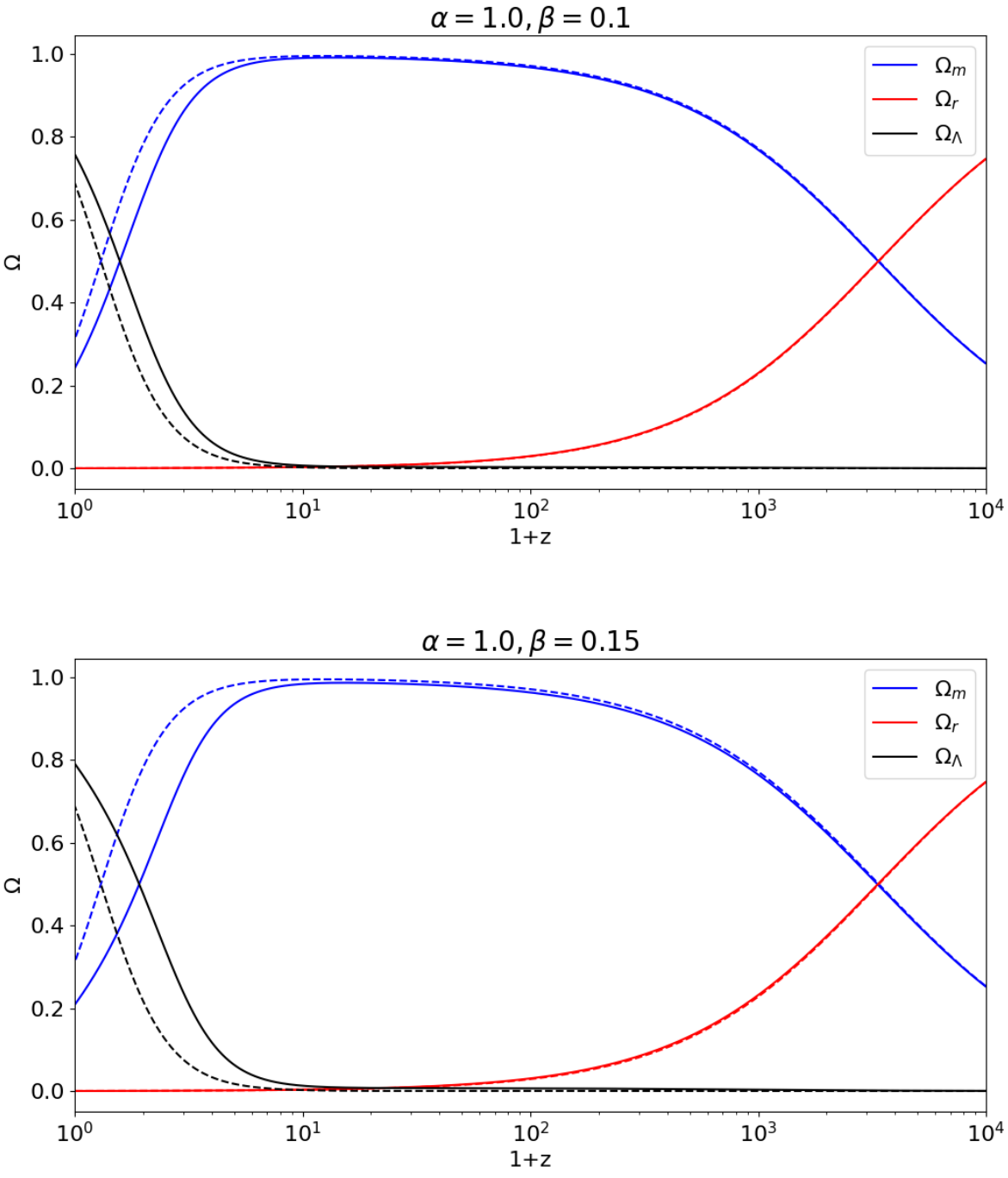

Figure 5.6: Evolution of density parameters $\Omega_r, \Omega_m, \Omega_{DE}$ as function of redshift of bouncing coupled dark energy models (solid lines) with positive coupling compared to ΛCDM standard model (dashed lines)

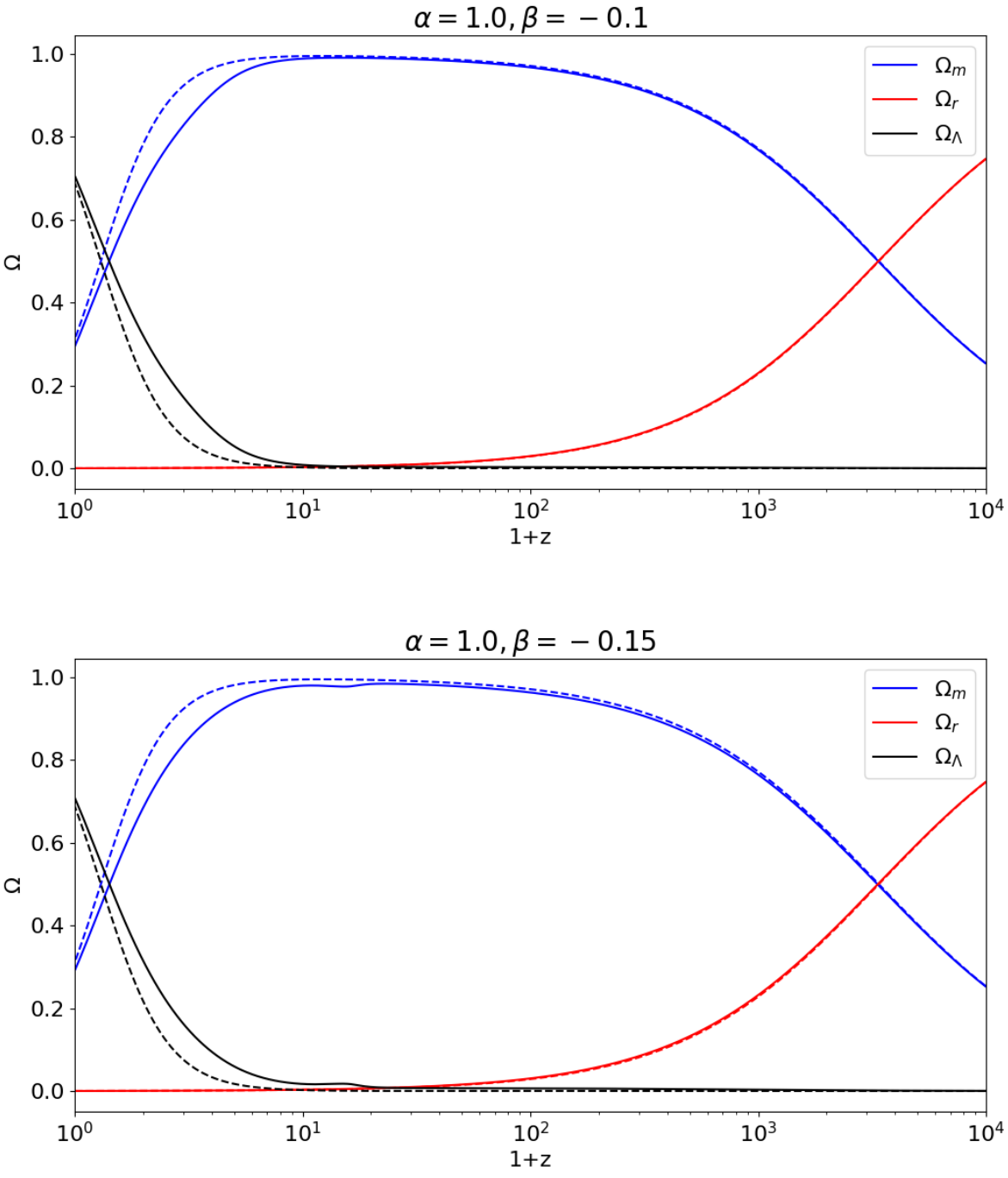

Figure 5.7: Evolution of density parameters $\Omega_r, \Omega_m, \Omega_{DE}$ as function of redshift of bouncing coupled dark energy models (solid lines) with negative coupling compared to ΛCDM standard model (dashed lines)

5.2 Simulations

From the study conducted in section 5.1, we selected six distinct BCDE models, as listed in Table 5.2. These models were chosen to systematically investigate how the coupling strength β and the potential slope α influence structure formation, particularly in the non-linear regime.

The four models with $\alpha = 1.0$ (A1BM15, A1BM1, A1BP1, A1BP15) and the two models with $\alpha = 2.0$ (A2BM15, A2BM1) extend the analysis of section 5.1 into the non-linear regime, using numerical simulations to probe features like halo mass functions, matter clustering, and weak lensing observables.

Model	α	β_c	β_b
ΛCDM	0.0	0.0	0.0
A1BM15	1.0	-0.15	0.0
A1BM1	1.0	-0.1	0.0
A1BP1	1.0	0.1	0.0
A1BP15	1.0	0.15	0.0
A2BM15	2.0	-0.15	0.0
A2BM1	2.0	-0.1	0.0

Table 5.2: List of cosmological BCDE models considered in this work, including the ΛCDM fiducial model used as a reference.

The A1 models ($\alpha = 1.0$) isolate the role of β_c, with simulations revealing how positive vs. negative couplings alter halo formation or the power spectrum. The A2 models ($\alpha = 2.0$) test whether a steeper potential slope exacerbates or mitigates these effects.

All the simulations have a box size of $500\,Mpc/h$ aside and contain 512^3 CDM and baryon particles for a total particle number of $2 \times 512^3 \sim 3 \times 10^8$. The mass resolution at $z = 0$ for these simulations is $m_c = 6.77 \times 10^{10} M\odot/h$ for CDM and $m_b = 1.27 \times 10^{10} M\odot/h$ for baryons. For these simulations we also modified the `GADGET-4` code by disabling the hydrodinamics calculations for the particles. This ensures that, despite their presence, the simulations remain purely collisionless N-body runs, focusing solely on gravitational interactions. As pointed out inBaldi (2012), the inclusion of baryonic particles is essential for accurately modeling structure formation in coupled dark energy (cDE) scenarios. Since baryons and CDM follow different dynamical equations in these models, with baryons remaining uncoupled to the dark energy field, omitting baryons would artificially amplify the coupling's impact on structure formation, leading to biased results. By retaining collisionless baryons, we not only maintain physical consistency but may also capture distinctive features in the relative distribution of CDM and baryons.

5.3 Non-linear structure formation in BCDE

In this section, we present the results of the cosmological simulations of the models listed in 5.2, focusing on the impact of Bouncing Coupled Dark Energy (BCDE) models on large-scale structure formation. With the help of publicly-available Python libraries like `Pylians3` (Villaescusa-Navarro, 2018) for power spectrum and halos analysis and the newly developed `DORIAN` library (Ferlito et al., 2025) for weak lensing, we explore the nonlinear evolution of matter perturbations, halo abundance, and gravitational lensing signatures in these alternative cosmologies.

Our investigation centers on the distinctive features introduced by the coupling between dark energy and cold dark matter (CDM), such as the velocity-dependent friction term and the fifth force emerging in BCDE scenarios. By comparing these models to the fiducial ΛCDM paradigm, we quantify deviations in the matter power spectrum, halo mass function, and weak lensing observables across multiple redshifts. The results highlight how the BCDE scenario influences structure formation, offering insights into the late-time evolution.

5.3.1 Matter power spectrum

The power spectrum we present here is computed from simulation data stored in `GADGET-4` snapshot files. These files contain the complete state of the simulated system at specific output times, including particle positions, velocities, and other relevant quantities. Each snapshot consists of one or more files in a structured binary format, typically HDF5, which allows for efficient storage and retrieval of large datasets.

The snapshot files begin with a header that stores global information such as the total number of particles, the simulation time or scale factor, cosmological parameters, and the box size. Following the header, the particle data is organized into blocks, each containing specific information as coordinates, velocities and particle IDs.

We can compute the matter power spectrum from `GADGET-4` simulation snapshots using the `Pylians3` library (Villaescusa-Navarro, 2018). The process begins by reading the snapshot data using `Pylians`' readgadget module to extract the header information, including the box size in Mpc/h, the total number of particles, their masses in $M_\odot/h$, and cosmological parameters like Ω_m, Ω_Λ, and the Hubble parameter h.

Next, we construct the density field by distributing the particles onto a 3D grid by adopting a CIC mass-assignment scheme, as described in chapter 3.

The density field is then normalized to compute the overdensity, defined as the density contrast relative to the mean density.

Once the density field is prepared, we compute the power spectrum us-

ing `Pylians`' Pk library. This involves taking the Fourier transform of the overdensity field and measuring the average squared amplitude of the Fourier modes as a function of wavenumber k.

Coherently with studies conducted in Baldi (2012), the models we investigate share a common normalization of linear perturbations at the redshift of the CMB. This choice results in different amplitudes of density perturbations at $z = 0$, since each model evolves differently for $z < z_{CMB}$.

As already discussed in Chapter 2.3, one of the consequences of introducing a coupling between the dark energy (DE) scalar field and cold dark matter (CDM) is the emergence of an additional velocity-dependent term that acts as a friction-like force. This term is proportional to $\beta\dot{\phi}$.

In particular, for the BCDE models we investigate, this friction term acts as an effective drag in the early universe, accelerating CDM particles along their direction of motion. However, once the scalar field reaches the inversion point, the sign of $\dot{\phi}$ changes, and the extra term begins to slow down structure formation, as discussed in section 5.1.

We now examine the effects of the coupling between the DE scalar field and CDM on the nonlinear matter power spectrum for the BCDE models introduced in section 5.2. In particular we start with the $A1$ models which share a common slope of $\alpha = 1.0$ and feature coupling coefficients $\beta = -0.15,\ -0.1,\ 0.1,\ 0.15$.

Each of these models features a different inversion point, leading to distinct times at which the scalar field undergoes its bounce. As a result, the transition from enhancement to suppression of structure formation occurs at different epochs for each model.

Figures 5.8, 5.9, 5.10, 5.11 show the ratio of the nonlinear matter power spectrum of each Bouncing Coupled Dark Energy model to the fiducial ΛCDM cosmology at redshift $z = 2, 1, 0.5, 0$ respectively.

Figures 5.12, 5.13, 5.14, 5.15 show instead the power spectrum ratio of models A2, featuring a potential slope $\alpha = 2.0$, with respect to the A1BM15 model, with $\alpha = 1, \beta_c = -0.15$.

As one can notice from these plots, the linear power spectrum ratio decreases significantly from $z = 2$ to $z = 0$, reflecting the late-time evolution of these models after passing the inversion point, when the clustering of matter is suppressed.

This effect is most pronounced in the A1BP15 model, where the linear amplitude of the power spectrum drops from 1.18 times the ΛCDM value at $z = 2$ to 0.8 at $z = 0$.

Conversely, the non-linear power spectrum, at scales $k \gtrsim 0.5\,h/\mathrm{Mpc}$, displays a strong increase of amplitude with time with respect to the ΛCDM scenario.

In particular, at $z = 0$, the model A1BP15 presents the lowest value of linear power spectrum ($\sim 20\%$ lower than ΛCDM) with a steep increase in the non-linear regime (up to $\sim 20\%$ more than ΛCDM) almost reaching the

value of A1BM15 model.

The A1BM15 model, instead, presents a non-linear power spectrum much closer to ΛCDM (less than 3% different) while, in the non-linear regime, it grows up to $\simeq 28\%$ more than standard ΛCDM.

Models with lower amplitude of the coupling strength, A1BP1 and A1BM1, end up with an almost identical shape of power spectrum, passing from $\sim 10\%$ less than ΛCDM in the linear regime to $\sim 10\%$ more in the non-linear one.

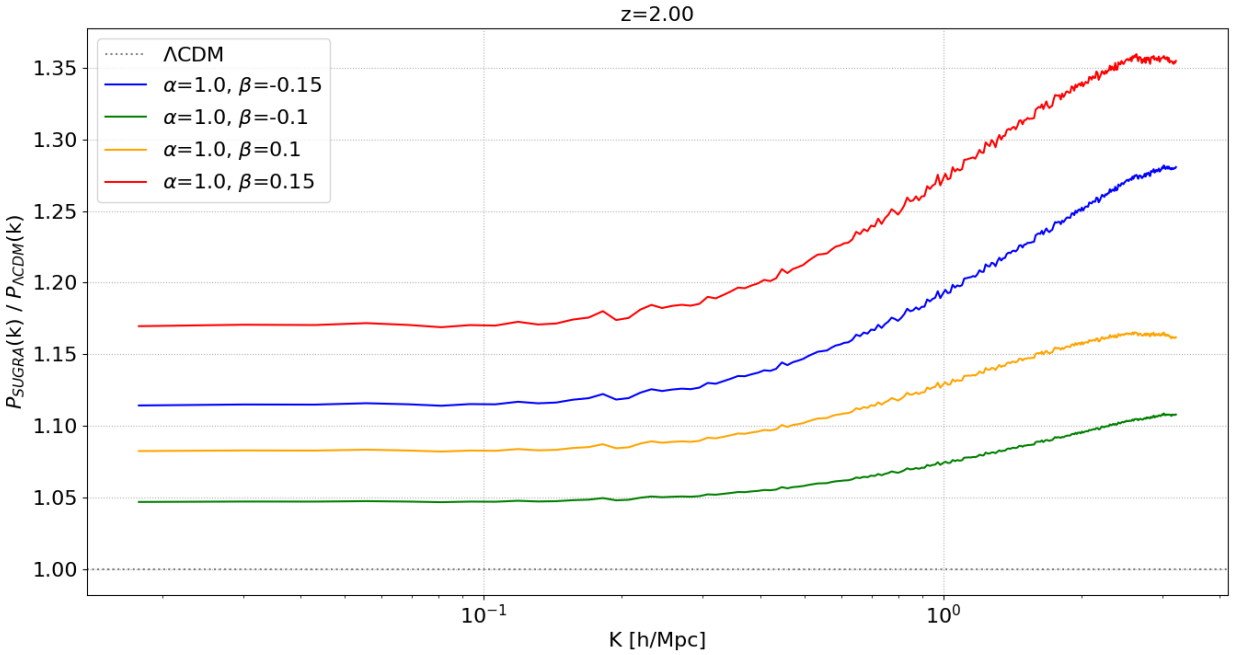

Figure 5.8: Ratio of the non linear matter power spectrum of BCDE models to the ΛCDM cosmology at redshift $z = 2$

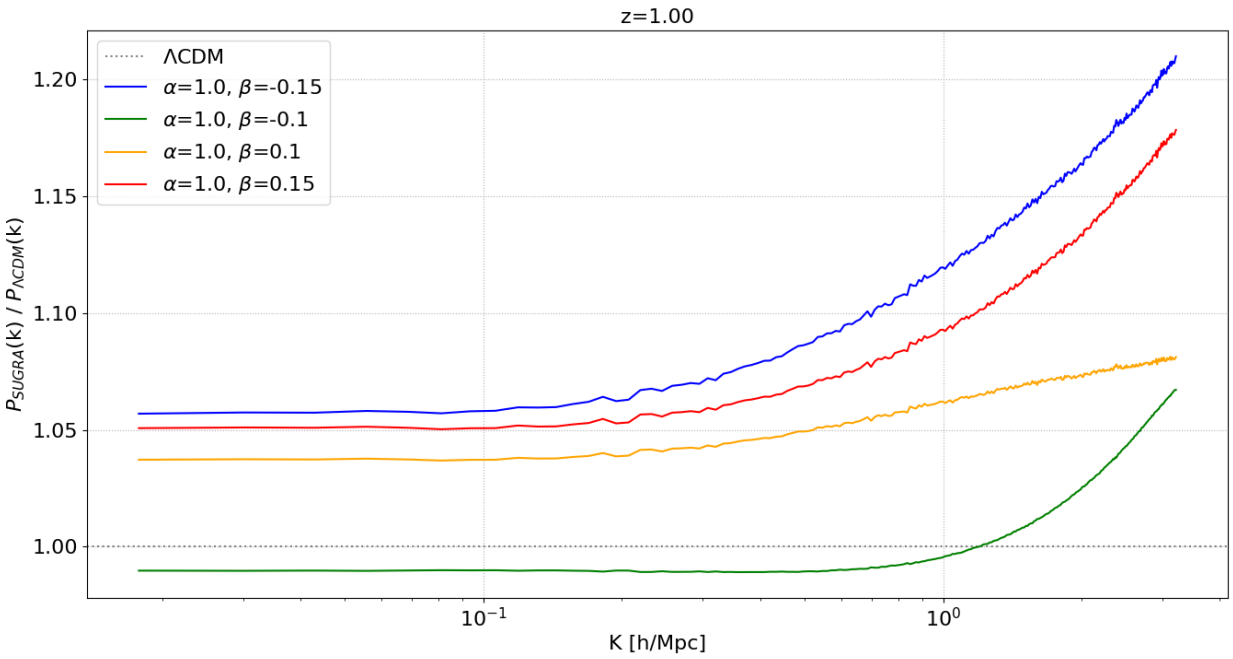

Figure 5.9: Ratio of the non linear matter power spectrum of BCDE models to the ΛCDM cosmology at redshift $z = 1$

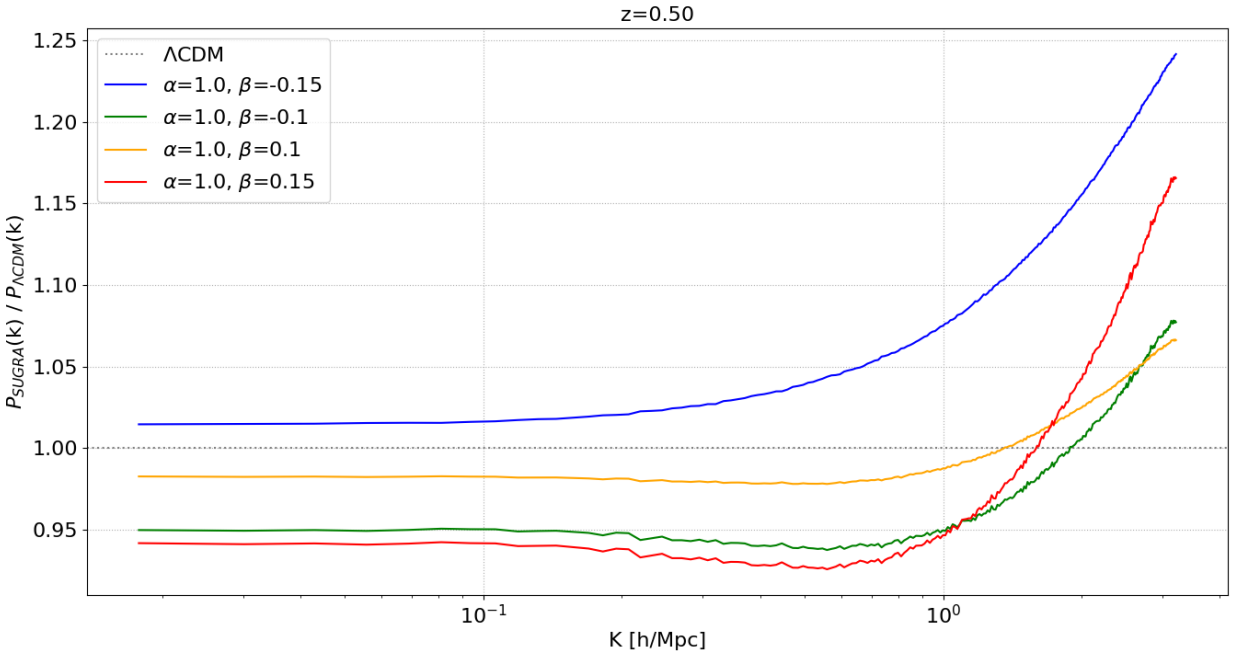

Figure 5.10: Ratio of the non linear matter power spectrum of BCDE models to the ΛCDM cosmology at redshift $z = 0.5$

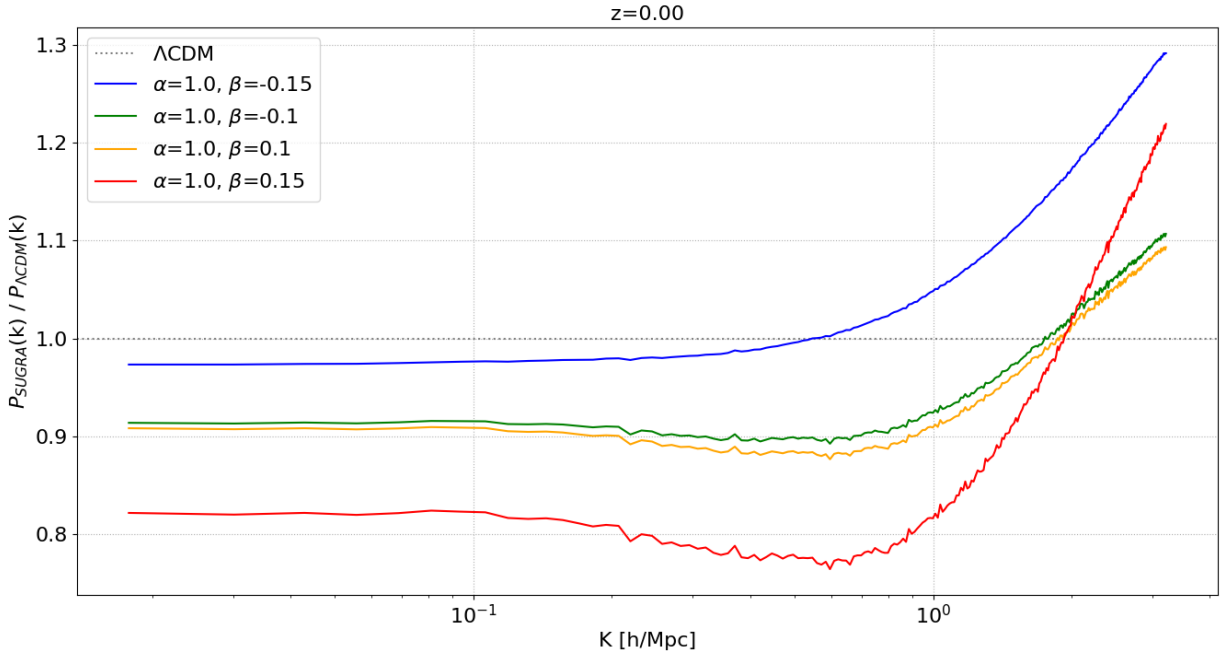

Figure 5.11: Ratio of the non linear matter power spectrum of BCDE models to the ΛCDM cosmology at redshift $z = 0$

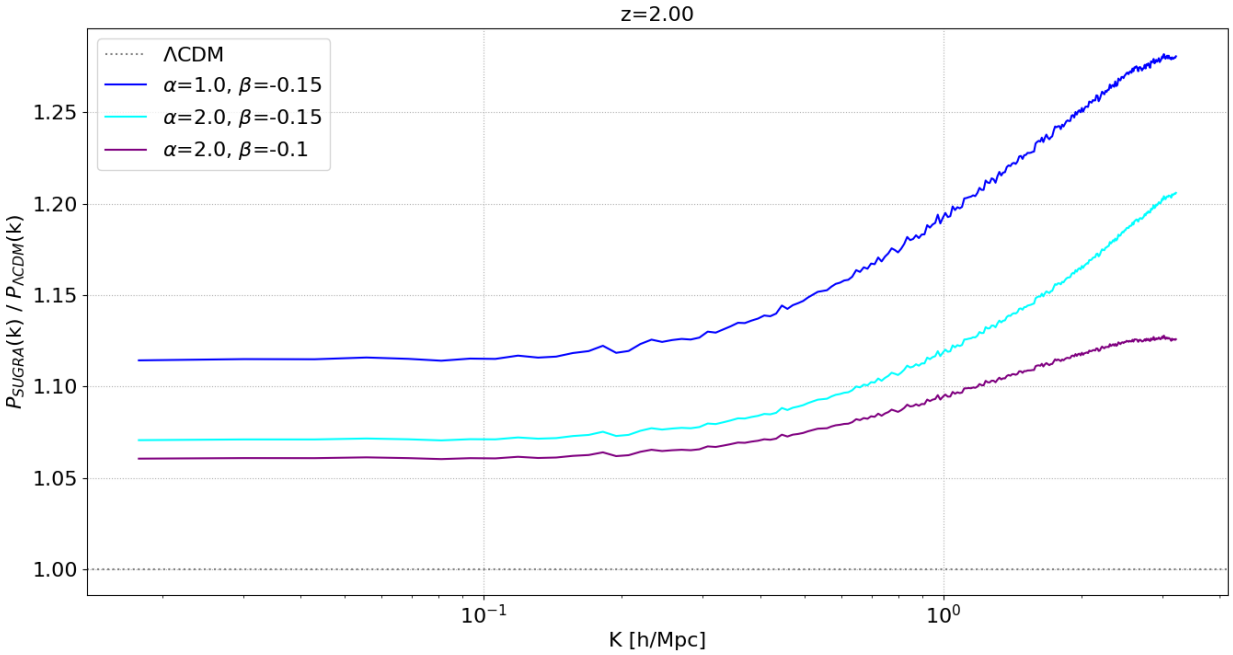

Figure 5.12: Ratio of the non linear matter power spectrum of BCDE models to the ΛCDM cosmology at redshift $z = 2$

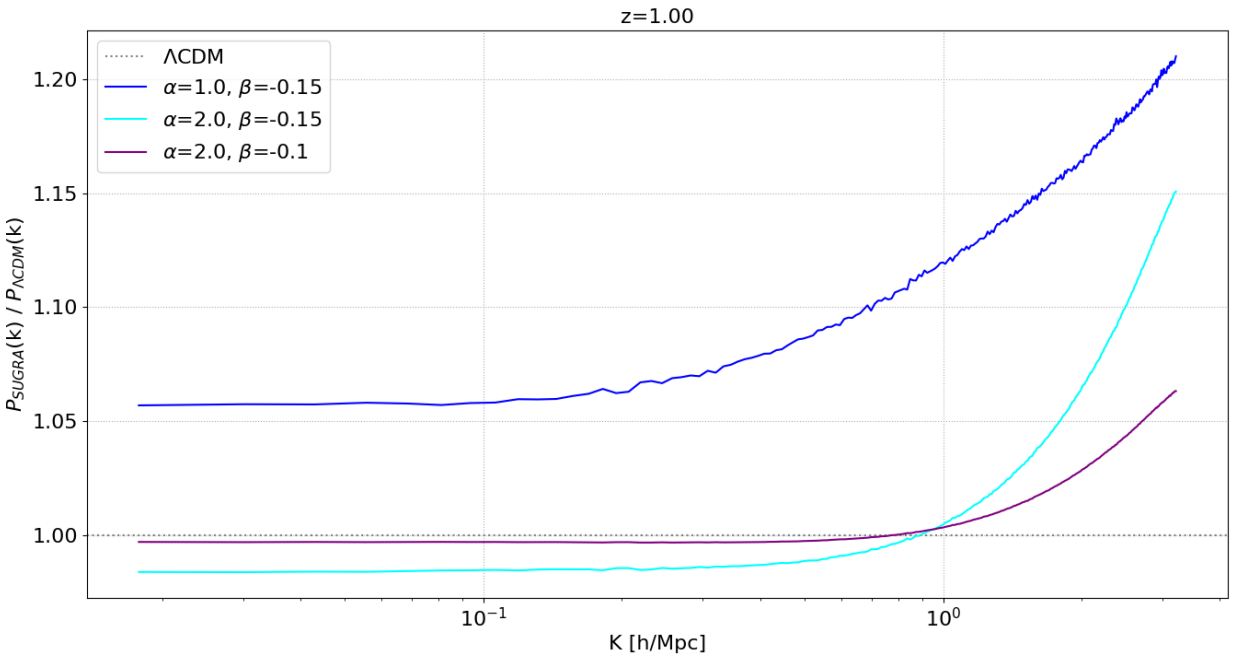

Figure 5.13: Ratio of the non linear matter power spectrum of BCDE models to the ΛCDM cosmology at redshift $z = 1$

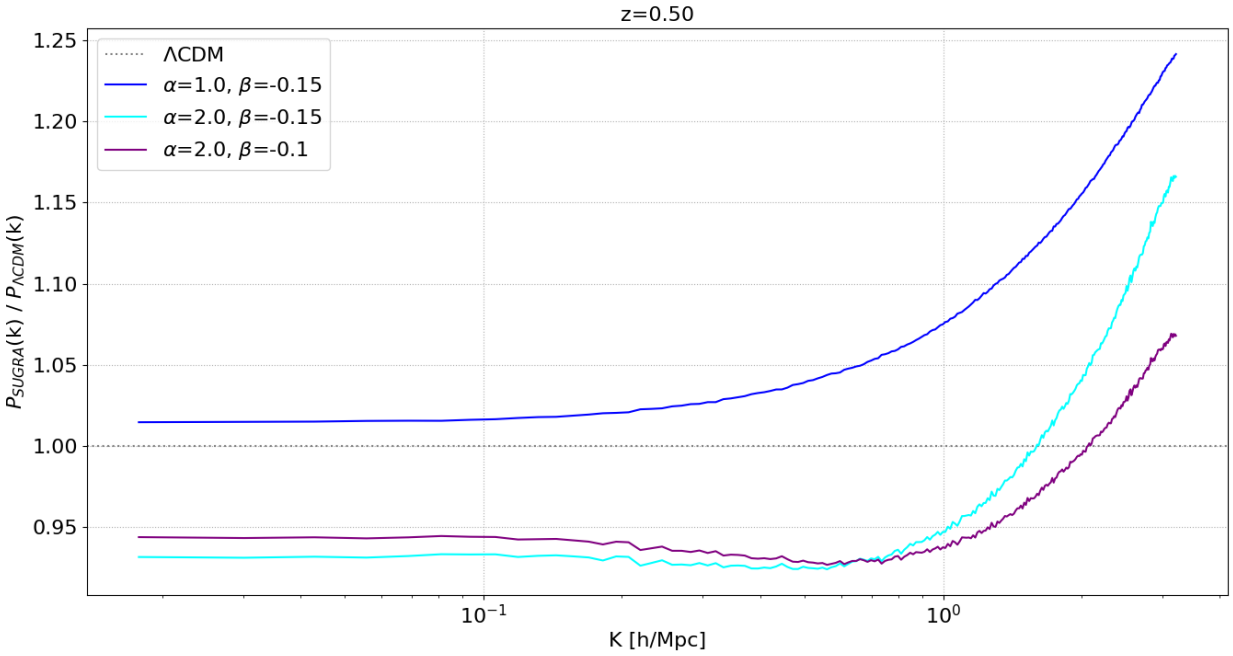

Figure 5.14: Ratio of the non linear matter power spectrum of BCDE models to the ΛCDM cosmology at redshift $z = 0.5$

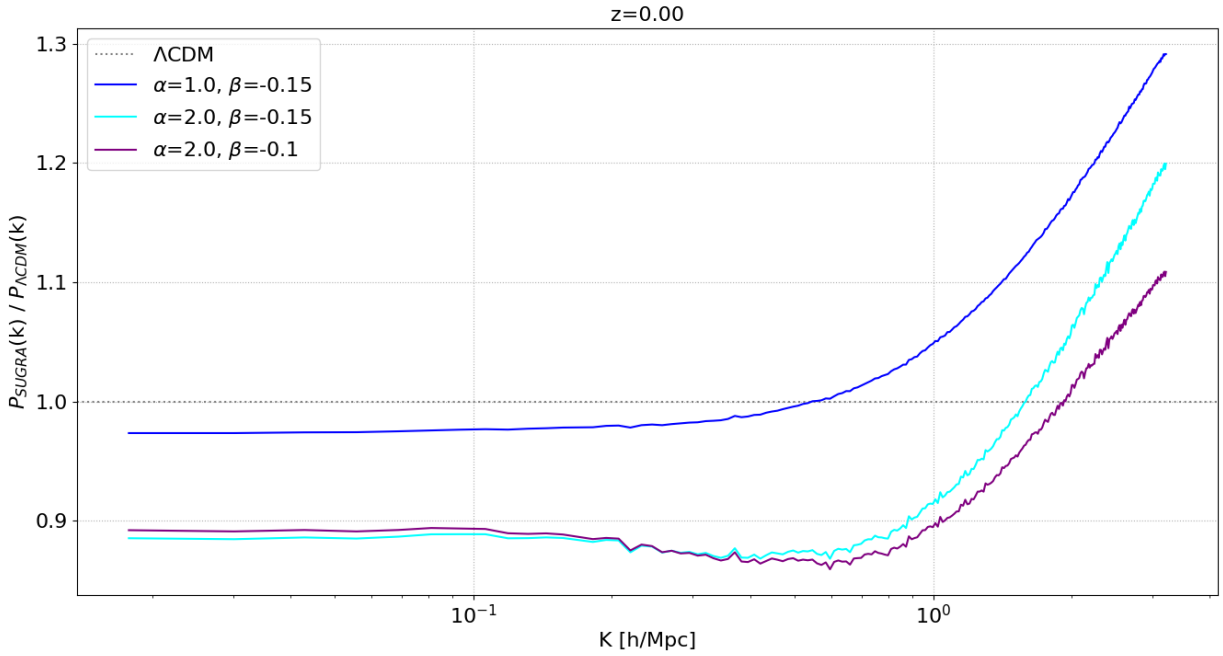

Figure 5.15: Ratio of the non linear matter power spectrum of BCDE models to the ΛCDM cosmology at redshift $z = 0$

5.3.2 Halo mass function

Another powerful probe of cosmological structure formation is the halo mass function (HMF), which quantifies the number density of dark matter halos as a function of their mass and redshift. The HMF reflects the cumulative impact of cosmological dynamics on the nonlinear growth of structure, making it a sensitive tool for testing deviations from the standard ΛCDM model, especially in scenarios involving dynamical or interacting dark energy. In this section, we investigate the HMFs predicted by bouncing dark energy models and compare them with the standard ΛCDM cosmology. The analysis focuses on halo abundance statistics extracted from N-body simulations, where halos are identified using the Friends-of-Friends (`FoF`) algorithm (Davis et al., 1985). We employ the `FoF` algorithm with a linking length $b = 0.2 \times \bar{d}$, where $\bar{d}$ is the mean inter-particle separation. This method groups together particles that are closer than this distance threshold, capturing the structure of gravitationally bound halos. Together with `FoF` we also apply `SUBFIND` algorithm which decomposes each halo into gravitationally bound subhalos. The `SUBFIND` algorithm identifies gravitationally bound substructures (subhalos) within dark matter halos by first computing the local density at each particle's position. It then isolates locally overdense regions and applies an unbinding procedure to retain only particles that are self-bound. For the main subhalo , the mass enclosed within a radius where the density exceeds 200 times the critical density (M_{200}) can be calculated by summing the bound particles within this threshold, providing a physically meaningful measure of the subhalo's virial mass.

In our simulations, Cold Dark Matter (CDM) particles are used as primary tracers of structure. Baryonic particles, which are not directly coupled to the dark energy sector, are assigned to halos by associating each particle with the FoF group of its nearest CDM neighbor.

Once the catalogs are generated, we compute the differential HMF using the `Pylians` library. The mass range is divided into 50 logarithmic bins spanning 2×10^{12} to $10^{15} M_{\odot}$, and we count the number of halos in each bin.

To standardize mass definitions, we compute M_{200} for each halo, defined by the following relation:

$$M_{\Delta c} = \frac{4}{3}\pi R_{\Delta c}^3 \Delta_c \rho_c \,. \tag{5.8}$$

This is the mass enclosed within a sphere where the mean density equals 200 times the critical density ρ_c of the Universe. This spherical overdensity mass is often preferred for observational comparisons and is consistent with the conventions used in halo catalogs across various simulation efforts.

Once we have obtained the differential HMF (halos number per unit mass and volume), we compute the cumulative mass function by integrating the

differential HMF over the mass

$$N(>M) = \int_M^\infty \frac{dn}{dM} dM \tag{5.9}$$

So now the cumulative HMF, $N(>M)$, represents the number density of halos with masses above a given value.

In figures 5.16, 5.17, 5.18, 5.19 we can see the cumulative mass function compared to the fiducial ΛCDM model at different redshifts. The bottom panel in each figure displays the ratio of the number counts with respect to the ΛCDM case.

As one can see from these figures, the BCDE models with a positive coupling, $\beta = 0.1, 0.15$, exhibit a significantly lower number of halos compared to the ΛCDM model.

In particular, for the A1BP15 model, this effect displays a strong mass dependence, starting with approximately 30% fewer halos at low masses at $z = 2.5$, and reaching up to a 70% reduction for higher-mass halos.

At lower redshifts, the mass dependence becomes more pronounced. By $z = 0$, the number of halos is about 20% lower for halos with masses around $2{\cdot}10^{12}\, M_\odot/h$, and nearly 90% lower for halos with masses around $6{\cdot}10^{14}\, M_\odot/h$.

On the other hand, models with a negative coupling, $\beta = -0.15, -0.1$, show a halo number density more consistent with the fiducial ΛCDM model across all redshifts, with only a slight reduction of up to about 20% at $z = 0$ for the $\beta = -0.1$ model.

The A2BM15 and A2BM1 models offer a less extreme scenario than A1BP15, with a number density of light halos close to ΛCDM and a reduction of heavy halos slightly steeper than the models featuring the same coupling coefficient but with $\alpha = 1.0$.

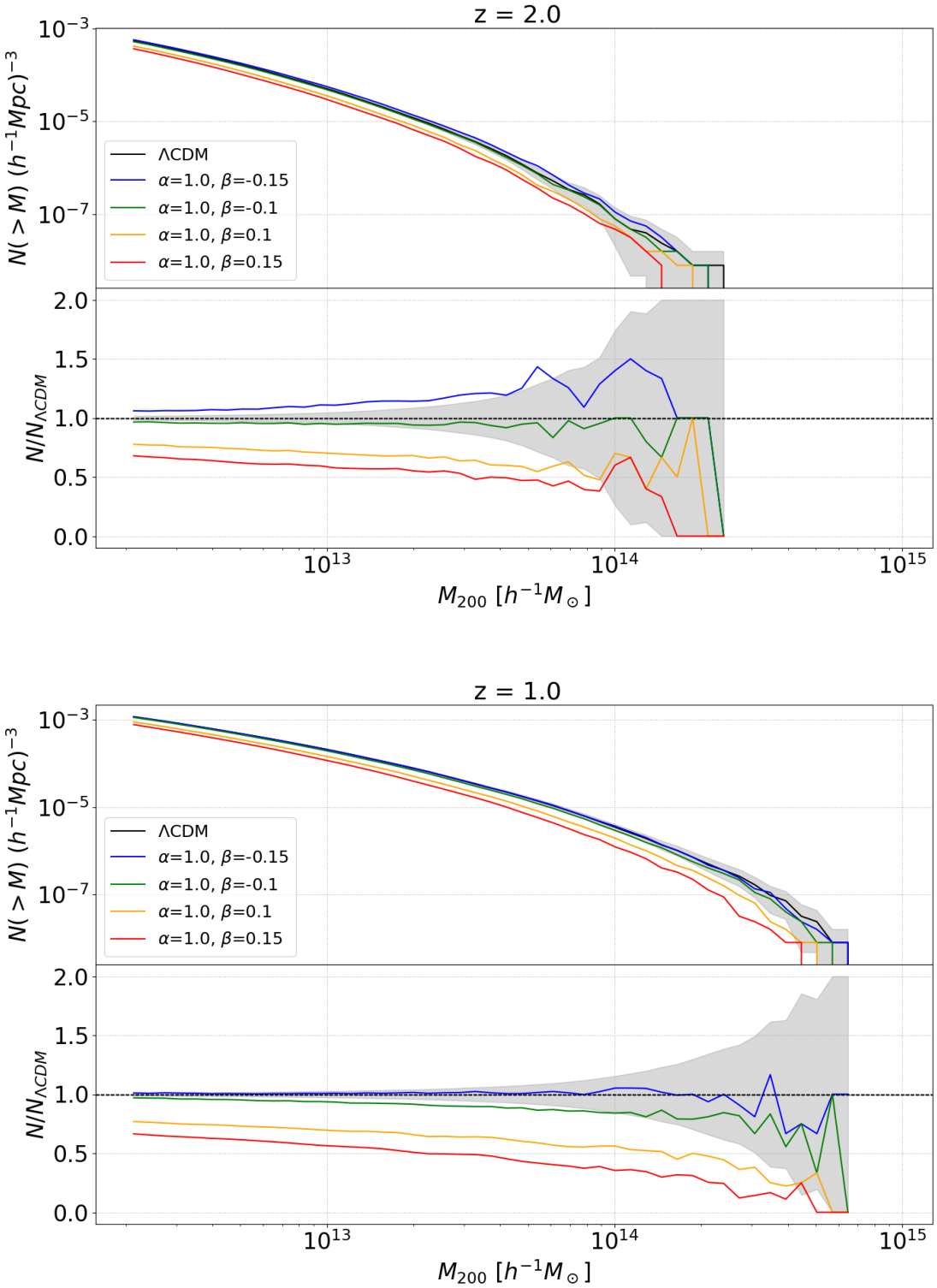

Figure 5.16: Cumulative Halo Mass Function (*upper panel*) and ratio to ΛCDM cosmology (*bottom panel*) for BCDE models with same $\alpha = 1.0$ and different values of the coupling β. The gray area around the ΛCDM represent the Poissonian errors based on the number counts of ΛCDM halos in each mass bin.

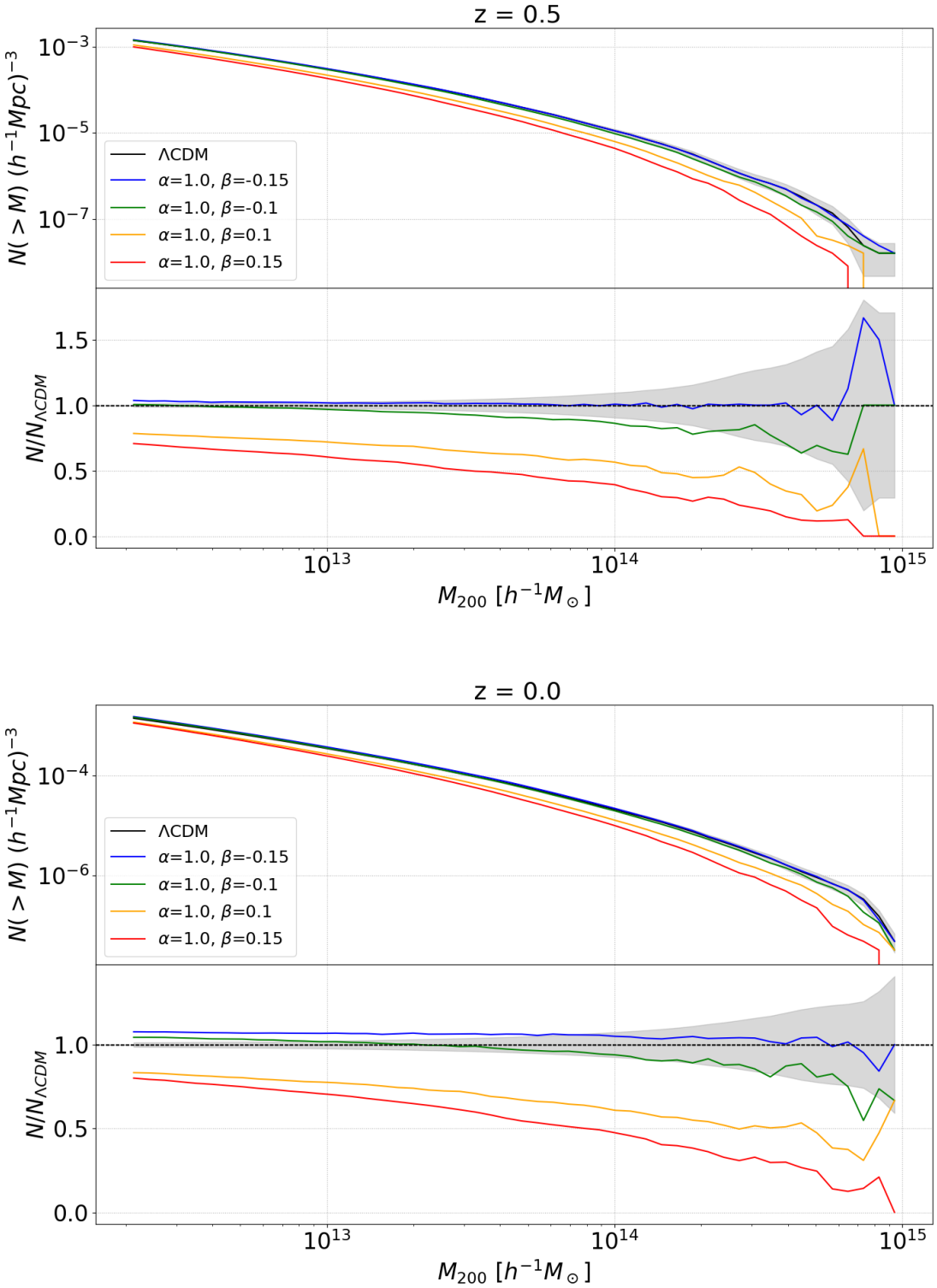

Figure 5.17: Cumulative Halo Mass Function (*upper panel*) and ratio to ΛCDM cosmology (*bottom panel*) for BCDE models with same $\alpha = 1.0$ and different values of the coupling β_c. The gray area around the ΛCDM represent the Poissonian errors based on the number counts of ΛCDM halos in each mass bin.

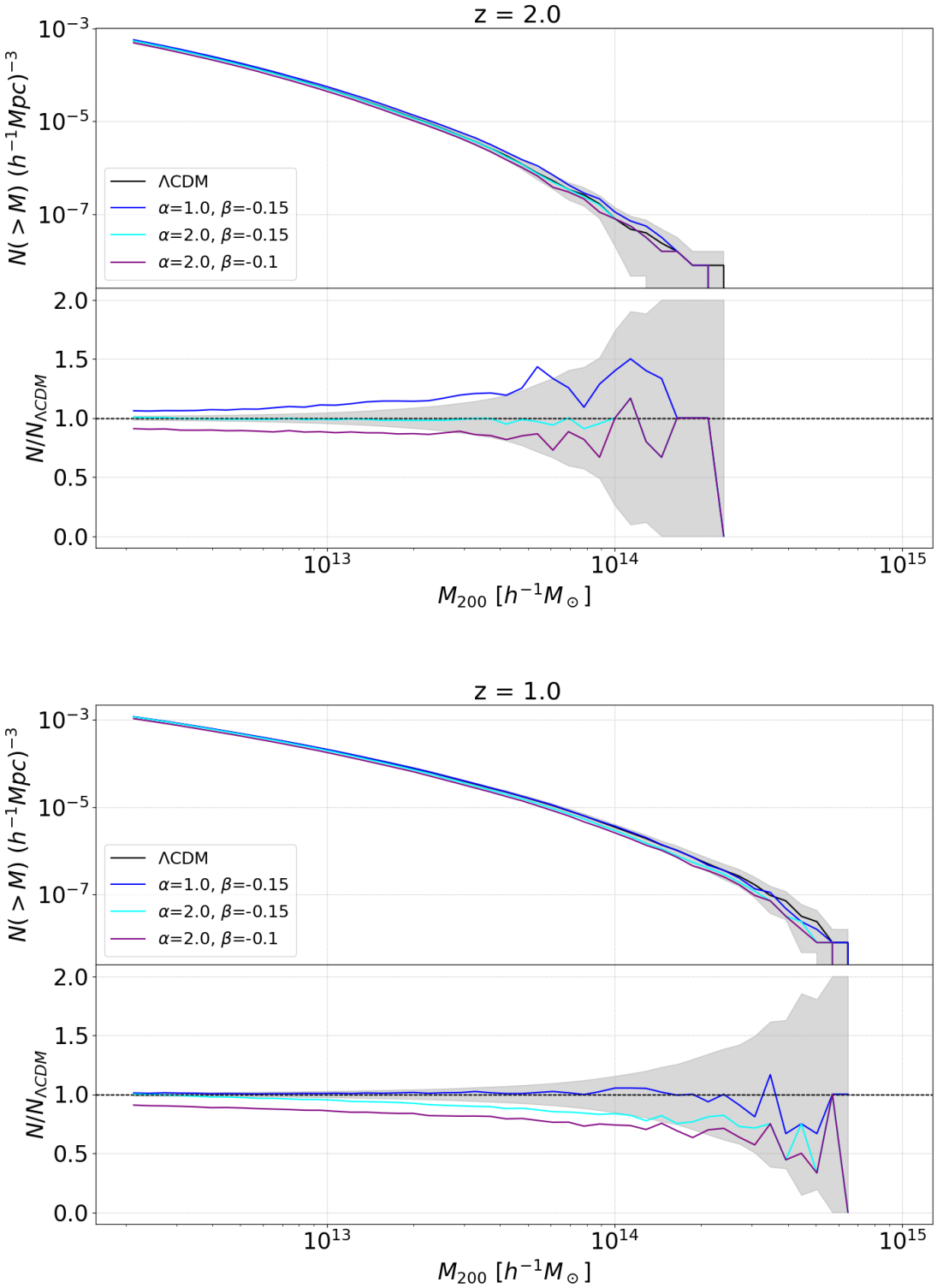

Figure 5.18: Cumulative Halo Mass Function (*upper panel*) and ratio to ΛCDM cosmology (*bottom panel*) for BCDE models with negative coupling $\beta_c < 0$ and different values of the slope α. The gray area around the ΛCDM represent the Poissonian errors based on the number counts of ΛCDM halos in each mass bin.

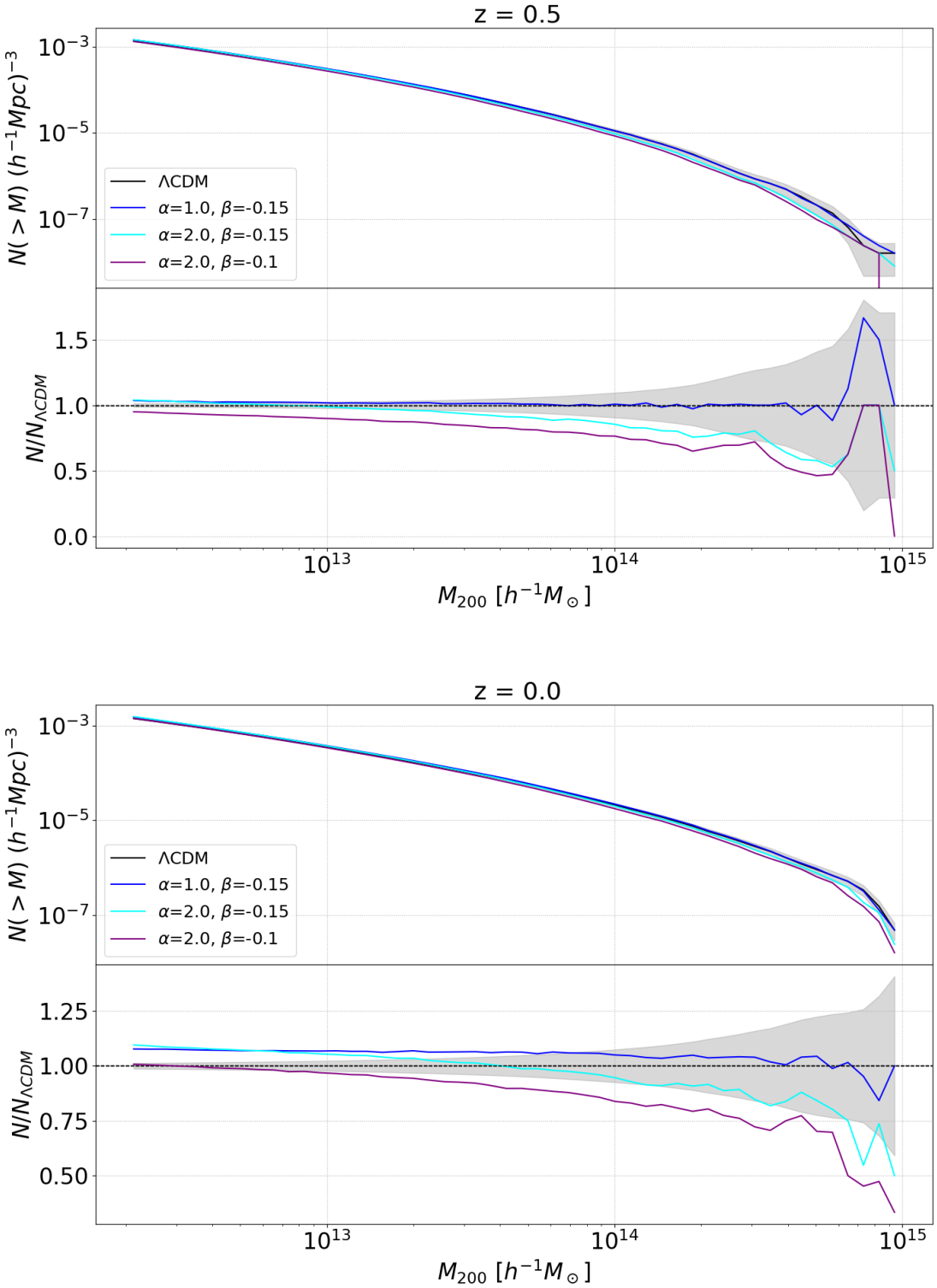

Figure 5.19: Cumulative Halo Mass Function (*upper panel*) and ratio to ΛCDM cosmology (*bottom panel*) for BCDE models with negative coupling $\beta_c < 0$ and different values of the slope α. The gray area around the ΛCDM represent the Poissonian errors based on the number counts of ΛCDM halos in each bin of mass.

5.3.3 Weak Lensing

Based on the theoretical framework of gravitational lensing described in section 1.10, we now investigate the impact of our BCDE models on the Weak Lensing observables from the fully non-linear mass distribution obtained from our N-body simulations. This analysis uses lensed sources at a given redshift to study the matter distribution between the sources and the observer, including both visible and dark matter.

For this analysis, we employ DORIAN (Ferlito et al., 2025), a newly developed Python library designed to perform full-sky ray tracing on `GADGET-4` mass-shell outputs. DORIAN uses as input the mass-shell output generated by `GADGET-4` when the `LIGHTCONE-OUTPUT` option is enabled in the corresponding configuration file. We have therefore preliminarily checked that such option does work properly also for our modified PANDA version of the code. This ensures that particles are recorded as they cross the backward lightcone, organizing them into mass-shell outputs with user-defined thicknesses. The maximum redshift of the lightcone and the shell thickness are specified in the `GADGET` parameter file. For our simulations, we adopted the following lightcone parameters:

- LightConeMassMapsNside = 4096
- LightConeMassMapThickness = 50 Mpc/h
- LightConeMassMapMaxRedshift = 2.5

The $N_{\rm side}$ parameter defines the angular resolution of the HEALPix pixelization. In this work, we employed $N_{\rm side} = 4096$, leading to maps with $12 \times N_{\rm side}^2 \simeq 2 \times 10^8$ equal-area pixels, corresponding to an angular resolution of ~ 0.86 arcmin. The maximum redshift selected, $z = 2.5$, requires repeating the comoving simulation boxes multiple times during the ray-tracing procedure. As we will discuss later, these box-replications can lead to geometric artifacts in the deflection angle and convergence maps.

In the weak lensing regime, the distortion matrix A encapsulates the effects of convergence (κ) and shear (γ), as derived in section 1.10:

$$A = \begin{pmatrix} 1 - \kappa - \gamma_1 & -\gamma_2 \\ -\gamma_2 & 1 - \kappa + \gamma_1 \end{pmatrix}, \tag{5.10}$$

where we assumed the rotation component to be negligible.

As detailed in (Ferlito et al., 2025), `DORIAN` constructs the distortion matrix from `GADGET-4` mass-maps by employing the multiple-lens-plane approximation to trace light rays through a series of concentric mass shells, accounting for the deflection caused by the matter distribution. The distortion matrix, which describes the image deformation, is computed iteratively by combining the contributions from each lens plane. The matrix includes convergence and

shear terms, derived from the lensing potential and its derivatives, evaluated using spherical harmonics for computational efficiency.

By iteratively tracing light rays through these planes and accounting for their deflections, DORIAN computes the distortion matrix A_{ij} capturing the full weak lensing effects beyond the Born approximation (described in section 1.10).

In its most basic implementation, DORIAN assumes a ΛCDM model when computing the comoving distance to the lensed source from the input redshift. However, in our BCDE models, the Hubble parameter $H(z)$ differs from ΛCDM, as we discussed in section 5.1, leading to different comoving distances at the same redshift with respect to the ΛCDM. To address this, we modified DORIAN's raytracing function to accept the comoving distance of the specified lensed source as an additional input. This ensures consistency with the cosmology of our models and avoids inaccuracies introduced by the ΛCDM assumption.

From the distortion matrix, we extract fundamental weak lensing quantities such as:

- the convergence (κ), which measures the magnification of background sources,
- the deflection angle (α), which quantifies the bending of light rays due to gravitational potential gradients.

Figures 5.20 show the full-sky convergence map for our fiducial ΛCDM model considering the lensed source at three different redshift: $z = 0.5$, 1.0, 2.5.

The presence of vertical and diagonal bands in these convergence maps is a manifestation of the box replication effect (Chen and Yu, 2024), a known artifact arising from the finite size of the simulation box. Due to the relatively small box size employed in our simulations, $500\,Mpc/h$, the light-cone construction requires multiple replications of the box along the line of sight, particularly at higher redshifts. This repetition introduces artificial periodic structures, visible as bands in the convergence maps. The effect is even more pronounced in deflection angle maps as this quantity is directly proportional to the gradient of the gravitational potential. Thus, if box replication introduces sharp discontinuities or strong gradients in the underlying mass distribution, these effects would be more directly and linearly reflected in quantities that depend on first derivatives (like deflection) rather than second derivatives (like convergence).

To better distinguish the evolution of convergence κ as a function of redshift, we plot the same convergence map of figure 5.20 but zoomed on a square region with 20° angular size.

As expected, the convergence values increase with source redshift, reflecting the greater integrated mass distribution encountered by photons traveling over larger comoving distances (Bartelmann and Schneider, 2001; Kilbinger,

2015). This behavior is explained by the fact that the effective convergence κ is a weighted projection of the matter density contrast along the line of sight. The maps at $z = 2.5$, therefore, exhibit stronger fluctuations compared to those at lower redshift, as they probe a larger fraction of the universe's matter distribution.

To analyze the impact of the late-time evolution in a BCDE scenario on weak lensing observables, in figure 5.22 we show the convergence maps difference of our BCDE models with respect to the ΛCDM case, as $\kappa_{\Lambda CDM} - \kappa_{BCDE}$. These plots highlight how the ΛCDM convergence is generally stronger compared to BCDE models, aligning with the theoretical expectations for the BCDE model, where late-time perturbations evolve more slowly due to the presence of a friction term and the particle-mass variation that leads to lower values of Ω_M. This behaviour may alleviate the S_8 tension that is primarly appearing through weak lensing observations (Heymans et al., 2021; Burger et al., 2023). The friction term in the BCDE model acts as a damping mechanism, slowing down the growth of matter perturbations compared to ΛCDM. In addition, the late-time mass variation leads to less massive particles, resulting in a lower Ω_M at low redshifts. As a result, at late times, the density contrast in the BCDE model is lower. Since the effective convergence κ is a weighted projection of the density contrast along the line of sight (Kilbinger, 2015; Ferlito et al., 2025), the slower growth of perturbations in BCDE naturally leads to a lower convergence signal.

Figure 5.23 shows the full-sky deflection map of the fiducial ΛCDM model considering the lensed source at three different redshift: $z = 0.5$, 1.0, 2.5. As discussed above, the artificial patterns visible in these plots are caused by the high number of box replications used to construct the full lightcone.

However, although this high number of replications affects the convergence and deflection maps, it mainly impacts the largest angular scales, and does not compromise the quality of our constraints (Takahashi et al., 2017). While box replication introduces artificial structures and an excess of power at large scales, its impact on the overall quality of cosmological constraints is mitigated by the dilution effect over larger sky coverages (Chen and Yu, 2024).

Therefore, although this effect can lead to an excess of power at large scales, it becomes negligible at smaller scales.

As done for the convergence κ, we show the deflection map focusing on a square region with an angular size of 20° for the ΛCDM cosmology (figure 5.24), along with its difference relative to the BCDE models (figure 5.25).

The deflection angles in BCDE models are systematically lower than in ΛCDM, particularly for the A1BP15 case, indicating weaker gravitational potential gradients due to suppressed structure growth from dark energy interactions. The A1BP15 model exhibits significantly reduced deflections that become more pronounced at higher source redshifts, while the A1BM15 model shows minimal deviation from ΛCDM, with nearly identical deflection angles at lower redshifts.

Before analyzing the impact of BCDE cosmology on the observable angular power spectrum, we assess the reliability of our pipeline by comparing the angular power spectrum of our ΛCDM simulation, produced with our newly implemented version of `PANDA-Gadget4`, against the theoretical ΛCDM predictions. To compute the theoretical ΛCDM angular power spectrum, we employ the `CCL` python library (Core Cosmology Library, (Chisari et al., 2019)) adopting the cosmological parameters listed in table 5.1. First, we define a galaxy sample by specifying a redshift distribution centered on the redshift of the lensed source, which for this test we assume $z_{source} = 1.0$. Then, we create weak lensing tracers to model the distortion of galaxy shapes by large-scale structure. These tracers incorporate the redshift distribution of source galaxies. The angular power spectrum is then calculated from the correlation of these tracers. Figure 5.26 show the comparison between the ΛCDM angular power spectrum computed with DORIAN from our simulations outputs (solid line) and the theoretical prediction evaluated with CCL library (dashed lines). As we can observe our ΛCDM weak lensing power spectrum shows good agreement with theoretical predictions at large scales, while at smaller scales it exhibits a power excess of $\sim 10\%$ respect to the theoretical prediction. This excess can be attributed to several resolution-related effects. First, the finite pixel resolution of the convergence maps (with $N\text{side} = 4096$) limits the ability to accurately capture small-scale fluctuations. Second, the mass resolution of the simulation, based on 2×512^3 particles (for dark matter and baryons), constrains the accurate representation of the nonlinear matter distribution, particularly in dense regions. Finally, the shot noise associated with the limited number of particles contributes to the excess power at high multipoles. Addressing these limitations, for instance by increasing the simulation resolution and employing higher $N\text{side}$ values, may significantly help reduce the discrepancy and improve the accuracy of the weak lensing signal in the nonlinear regime.

Figure 5.27 presents the convergence angular power spectrum for our models, computed with DORIAN and binned into 80 equally spaced logarithmic bins in the range $\ell \in [1, 1.3 \times 10^4]$. Given that we produced our mass maps with $N\text{side} = 4096$, the maximum multipole ℓ_{max} is set by default to $\ell_{max} = 3 \times N\text{side} - 1 = 1.3 \times 10^4$, consistent with the HEALPix convention.

We can notice how, for $z \leq 2.5$, almost all the BCDE models exhibit a convergence angular power spectrum lower than the ΛCDM value. Only the A1BM15 model shows an angular power spectrum slightly higher than ΛCDM at small scales ($\ell > 10^3$), for lensed sources at $z = 0.5$. This aligns with theoretical expectations, as the late-time evolution of our BCDE models is characterized by suppressed structure growth due to the combined effect of friction term and late-time mass variation, introduced by the BCDE cosmology (see section 5.1). In particular, the A1BP15 model exhibits a linear amplitude of the angular power spectrum $\sim 60\%$ lower compared to ΛCDM. As a general trend, we also observe how the non-linear tails of the angular

power spectra in these models increase with respect to the ΛCDM counterpart for lower source redshifts.

In figure 5.28 we show the Probability Density Function (PDF) of convergence field κ for BCDE models compared to ΛCDM. The BCDE models consistently exhibit a higher probability, with respect to ΛCDM, for κ values near zero, while it decreases below ΛCDM in both the high-κ and low-κ tails of the distribution. This indicates that the BCDE models produce fewer extreme density fluctuations (as the κ is the weighted projection of the density contrast along the line of sight), leading to a more concentrated distribution of convergence values around the mean. For lensed sources at $z = 2.5$, the A1BP15 model exhibits a higher probability for κ in the range $-0.035 \lesssim \kappa \lesssim 0.025$, reaching a peak enhancement of 25% compared to ΛCDM. This effect becomes even more pronounced at $z = 0.5$, where the range of enhanced probability narrows to $-0.01 \lesssim \kappa \lesssim 0.01$, and the probability within this range reaches a peak increase of 50% relative to the ΛCDM scenario. The narrowing of the PDF reflects a reduction in both high-density peaks (massive structures) and low-density voids, as the friction term in BCDE cosmology dampens the overall clustering of matter at late times.

Finally, figures 5.29, 5.30 and 5.31 display the peaks and minima counts of the convergence field κ, for the selected BCDE models, at lensed source redshift $z = 0.5$, 1.0 and 2.5, respectively. For the peaks counts, we observe that while A1BP15 model predicts an excess of low-κ peaks ($\kappa \lesssim 0.025$) at $z = 2.5$, other models, such as A1BM15, show the opposite trend. In particular A1BM15 exhibits a peaks-deficit in a range $0 \lesssim \kappa \lesssim 0.07$ and an increased peaks-count at more extreme κ values.

The minima counts exhibit a more distinct difference between BCDE models featuring different sign of the coupling strength β. In fact, $\beta > 0$ models show a minima distribution shifted toward larger κ value and a narrower distribution with a minima count up to 2 times the ΛCDM count for the A1BP15 model at $z = 0.5$. For the A1BP15 model, at $z = 0.5$, minima count is higher than ΛCDM, in the range $-0.01 \lesssim \kappa \lesssim 0$, while it widens at larger redshifts. This strong enhancement of shallow minima (corresponding to mildly underdense regions) is accompanied by a reduction of deeper minima ($\kappa < -0.01$). Again, we can relate this effect to the suppressed growth of non-linear density perturbations at late times. In contrast, $\beta < 0$ models show a behavior much closer to the ΛCDM scenario.

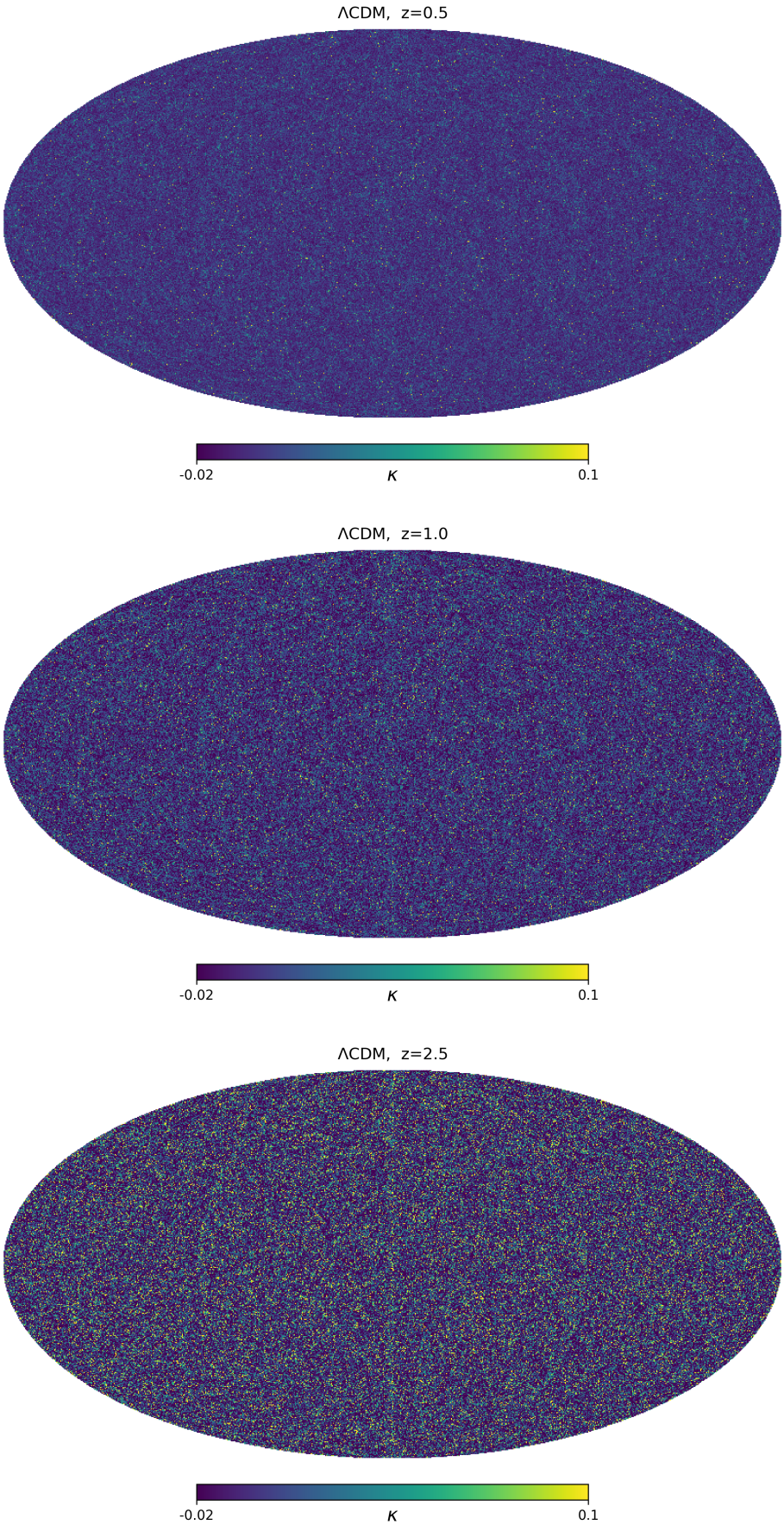

Figure 5.20: ΛCDM convergence map at different redshifts: z = 0.5 (top), z = 1.0 (middle), and z = 2.5 (bottom)

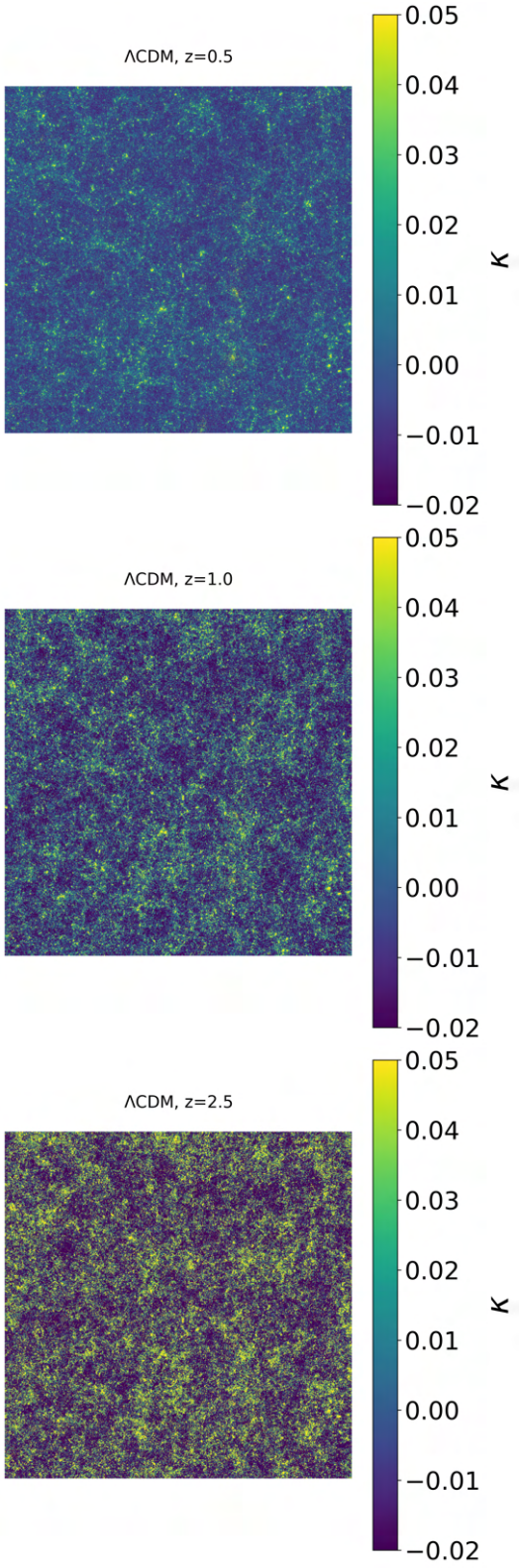

Figure 5.21: ΛCDM convergence maps zoomed over a region with angular size = 20°

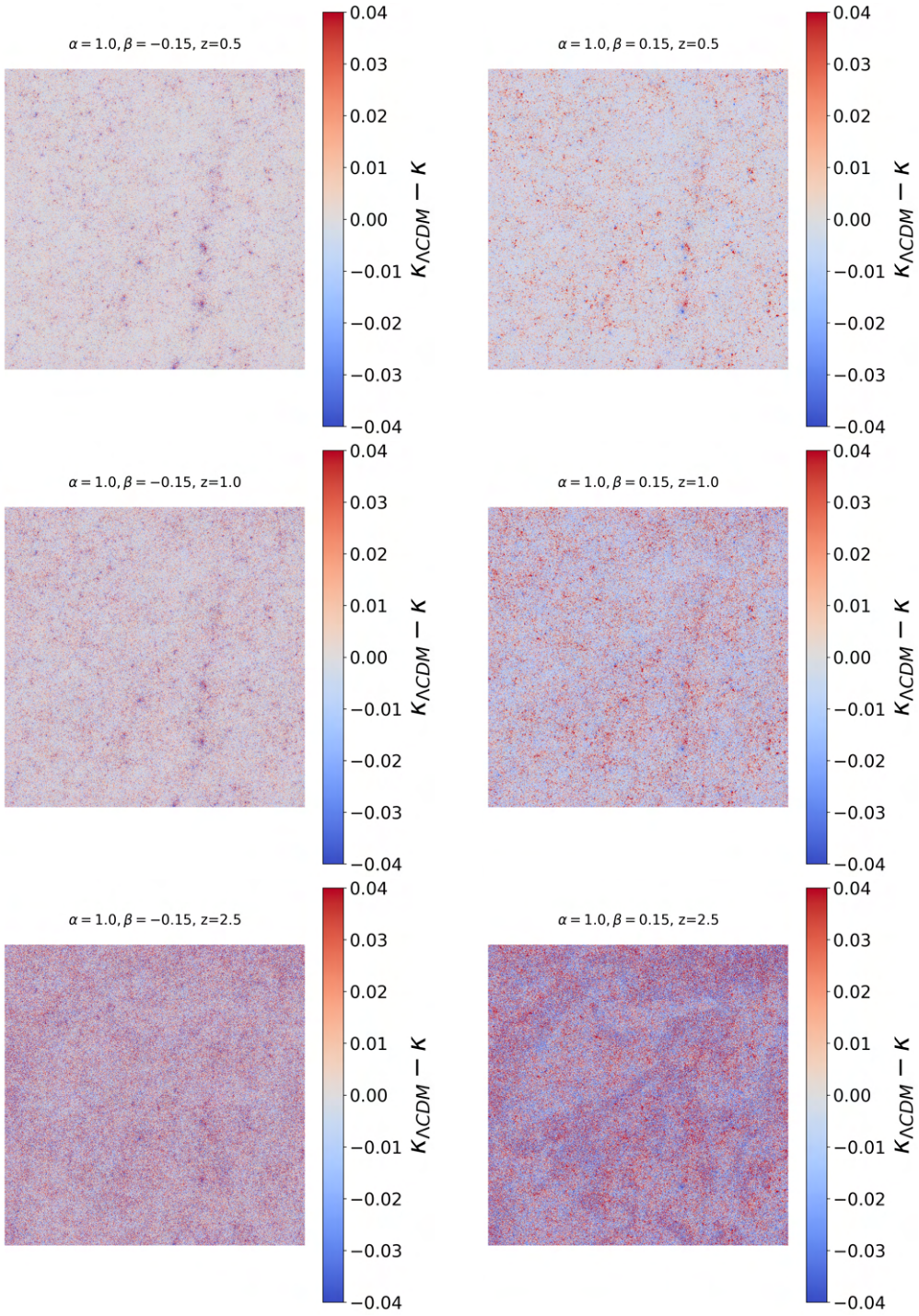

Figure 5.22: Convergence difference between ΛCDM and $\beta = \pm 0.15$

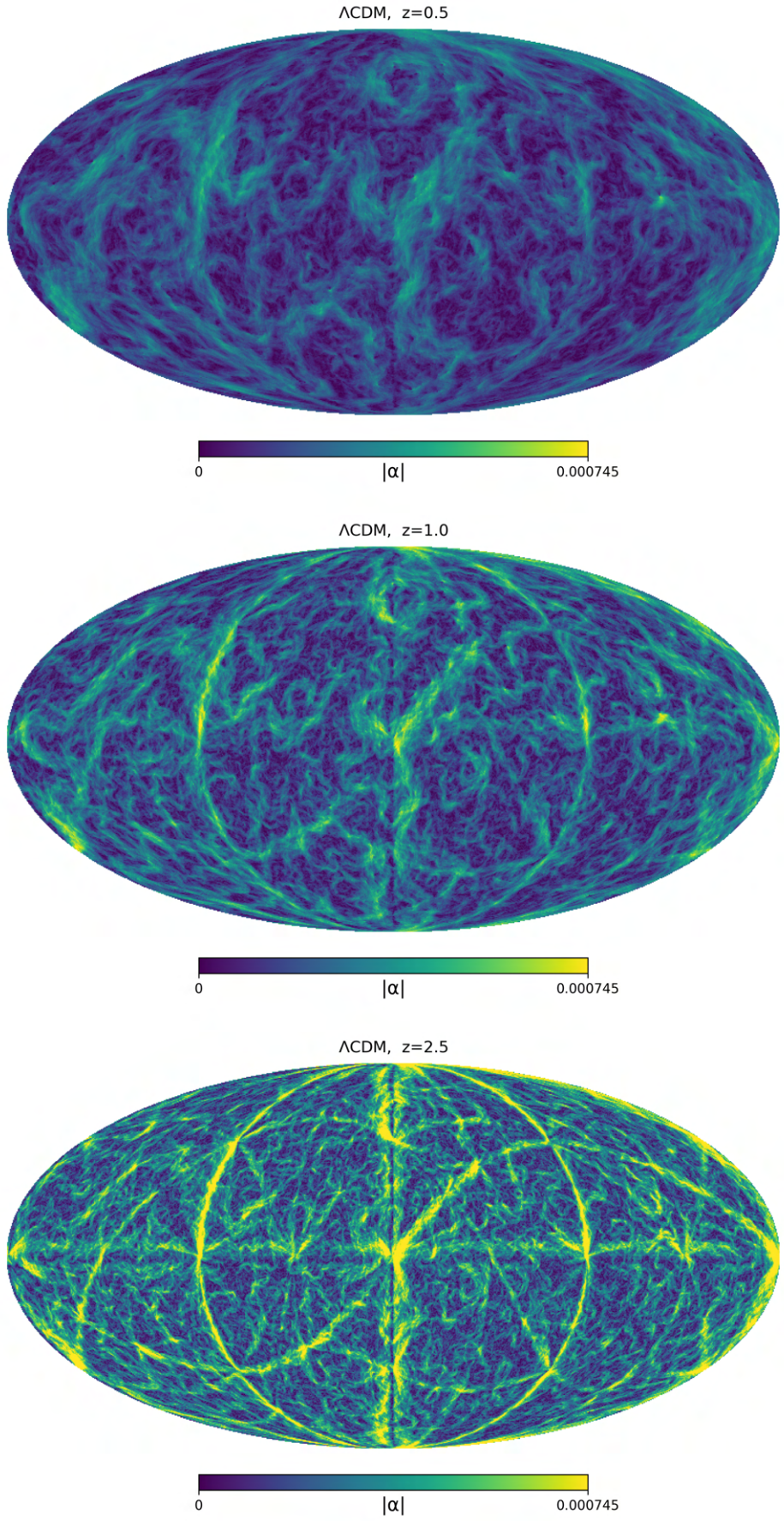

Figure 5.23: ΛCDM deflection map at different redshifts: z = 0.5 (top), z = 1.0 (middle), and z = 2.5 (bottom)

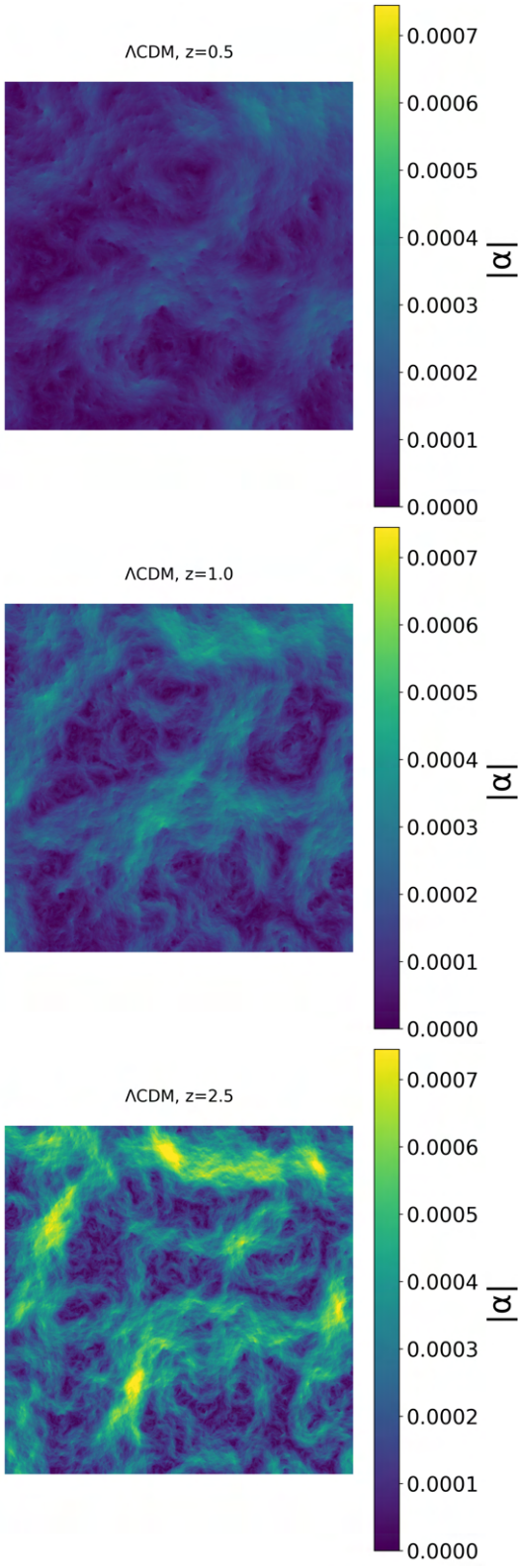

Figure 5.24: ΛCDM deflection maps zoomed over a region with angular size = 20°

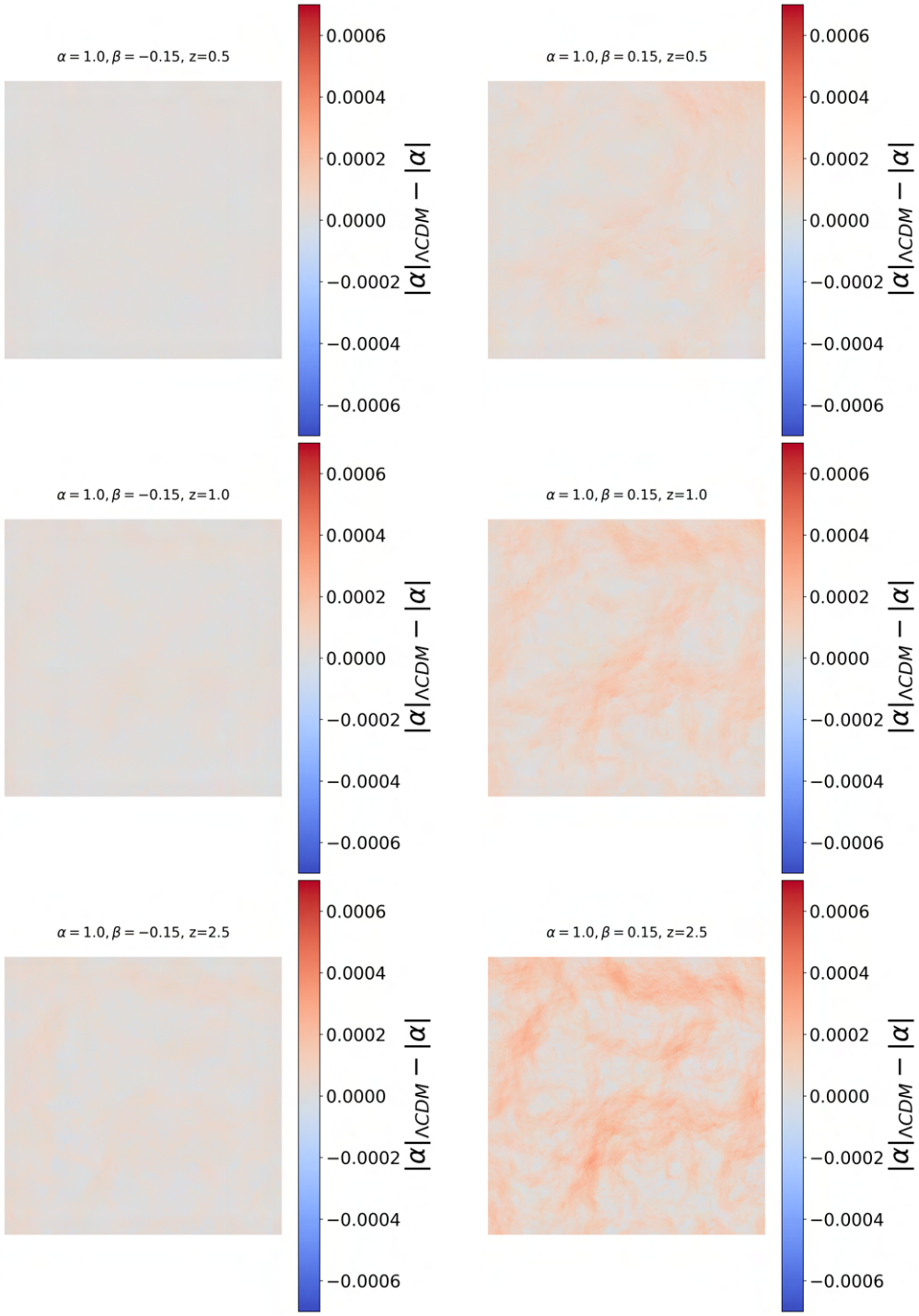

Figure 5.25: Deflection difference between ΛCDM and $\beta = \pm 0.15$

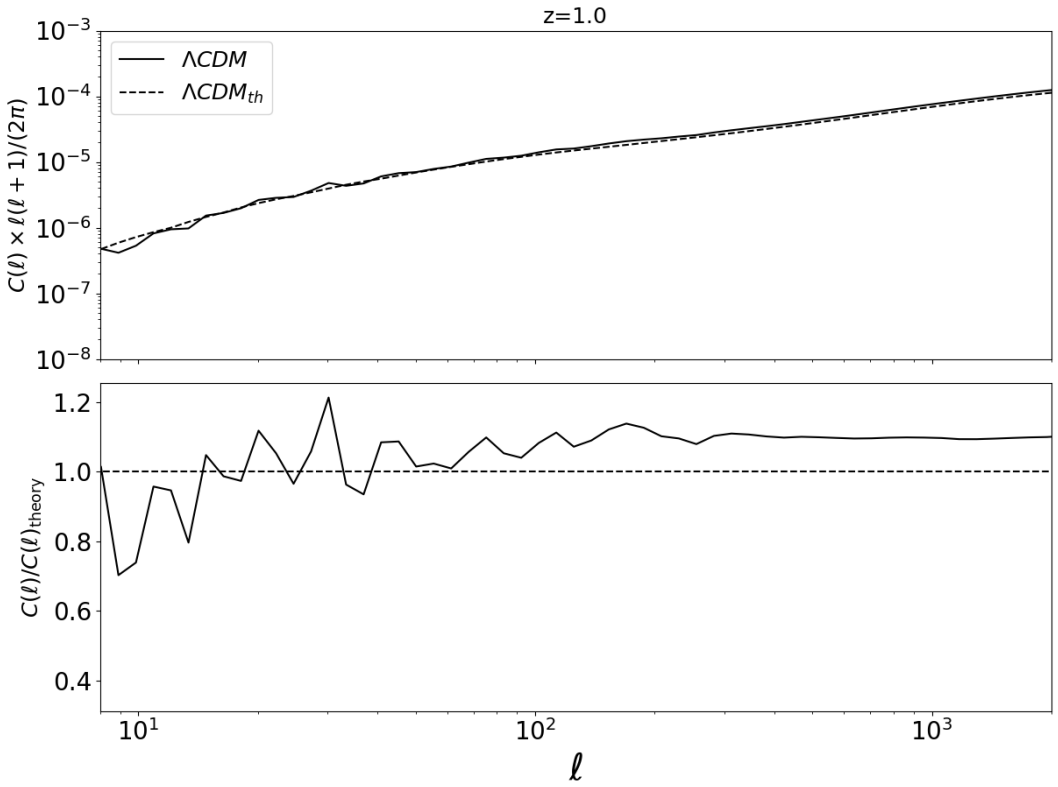

Figure 5.26: Comparison between the ΛCDM angular power spectrum from our simulations computed with `DORIAN` (solid line) and the theoretical prediction evaluated using `CCL` library (Chisari et al., 2019).

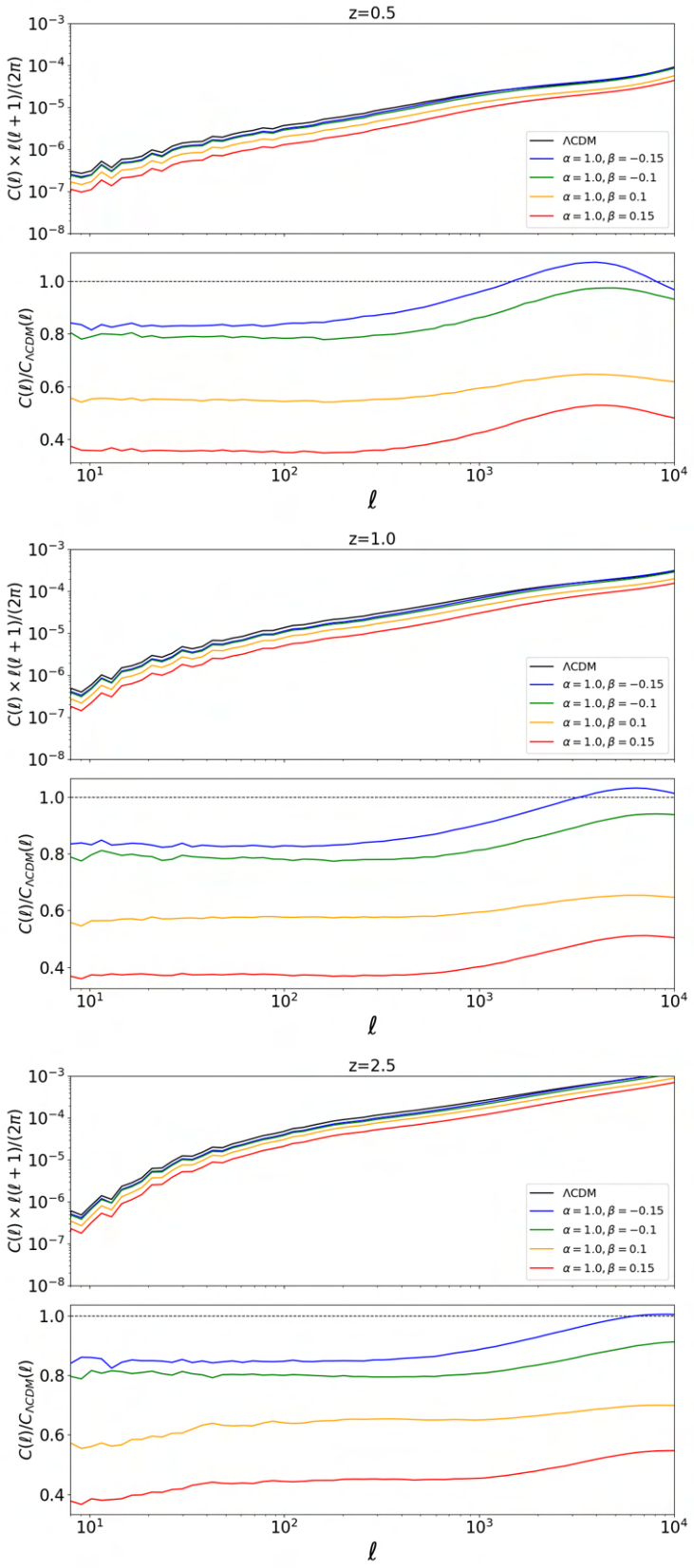

Figure 5.27: Angular power spectrum of the convergence field κ (*upper panel*) and ratio to ΛCDM model (*bottom panel*) for different source redshift.

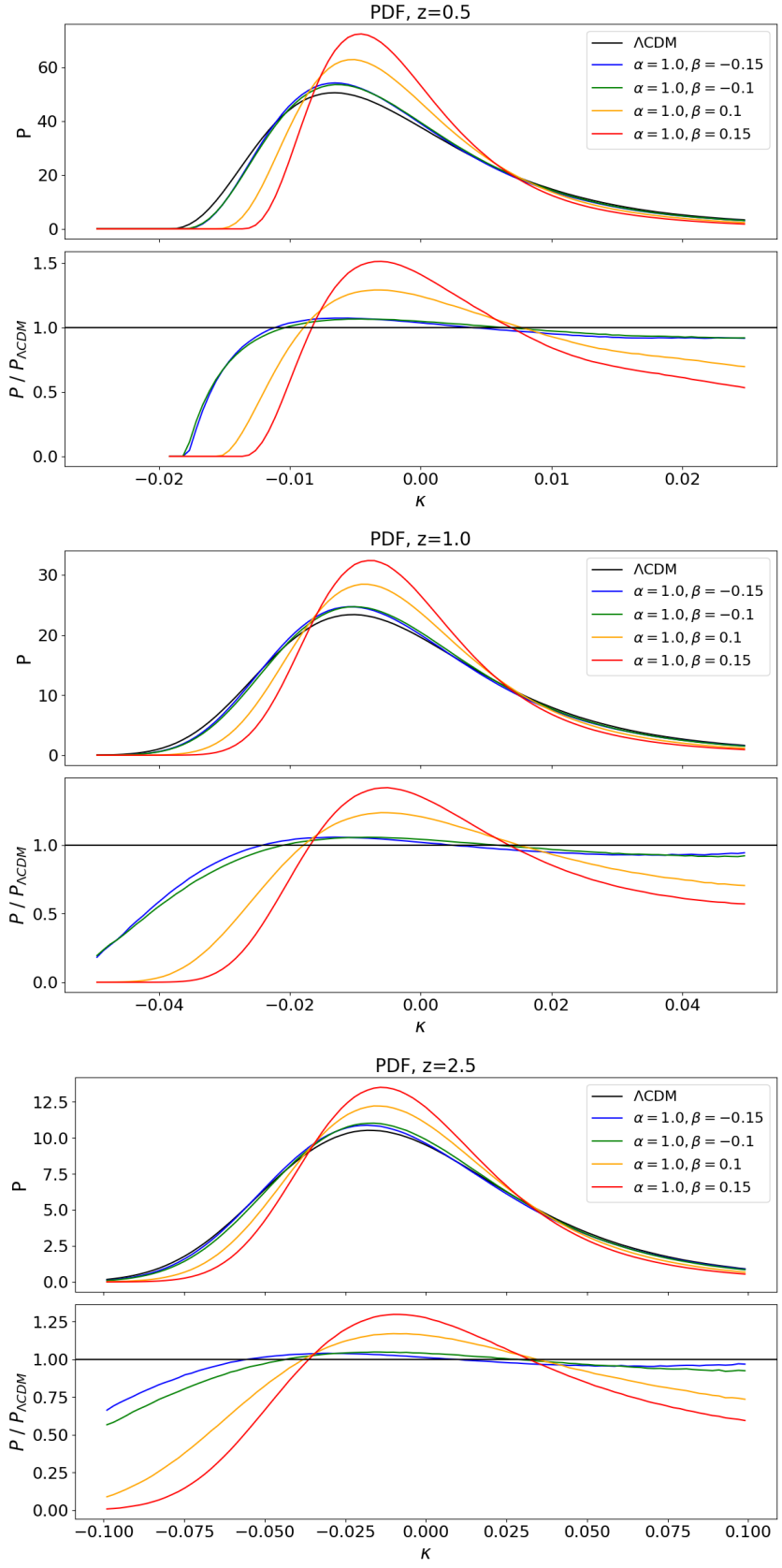

Figure 5.28: PDF of convergence κ for different BCDE models (*upper panel*), and PDF ratio with respect to the ΛCDM fiducial model (*bottom panel*

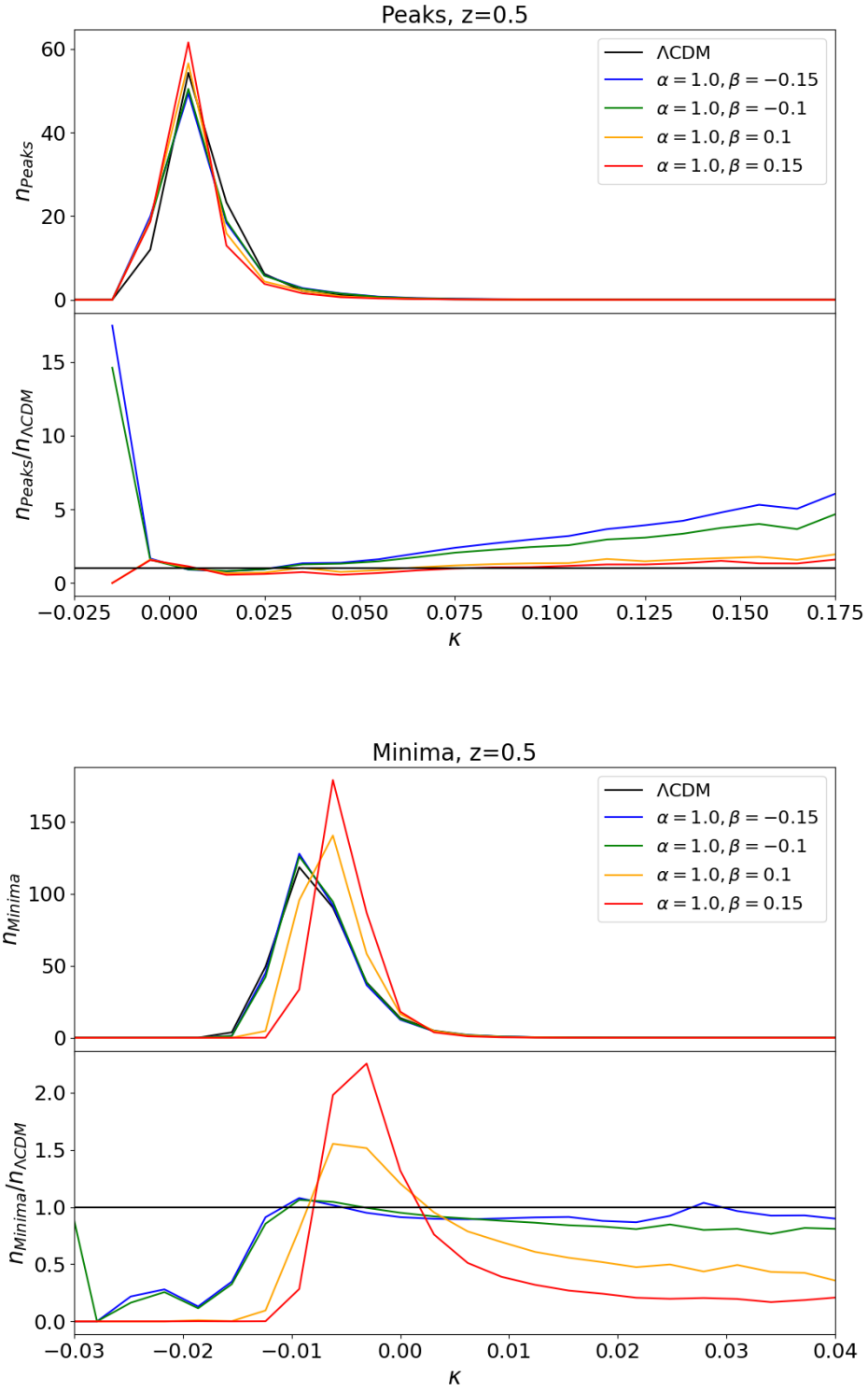

Figure 5.29: Peaks counts (*top*) and minima counts (*bottom*) for BCDE models, compared to ΛCDM model, for $z = 0.5$

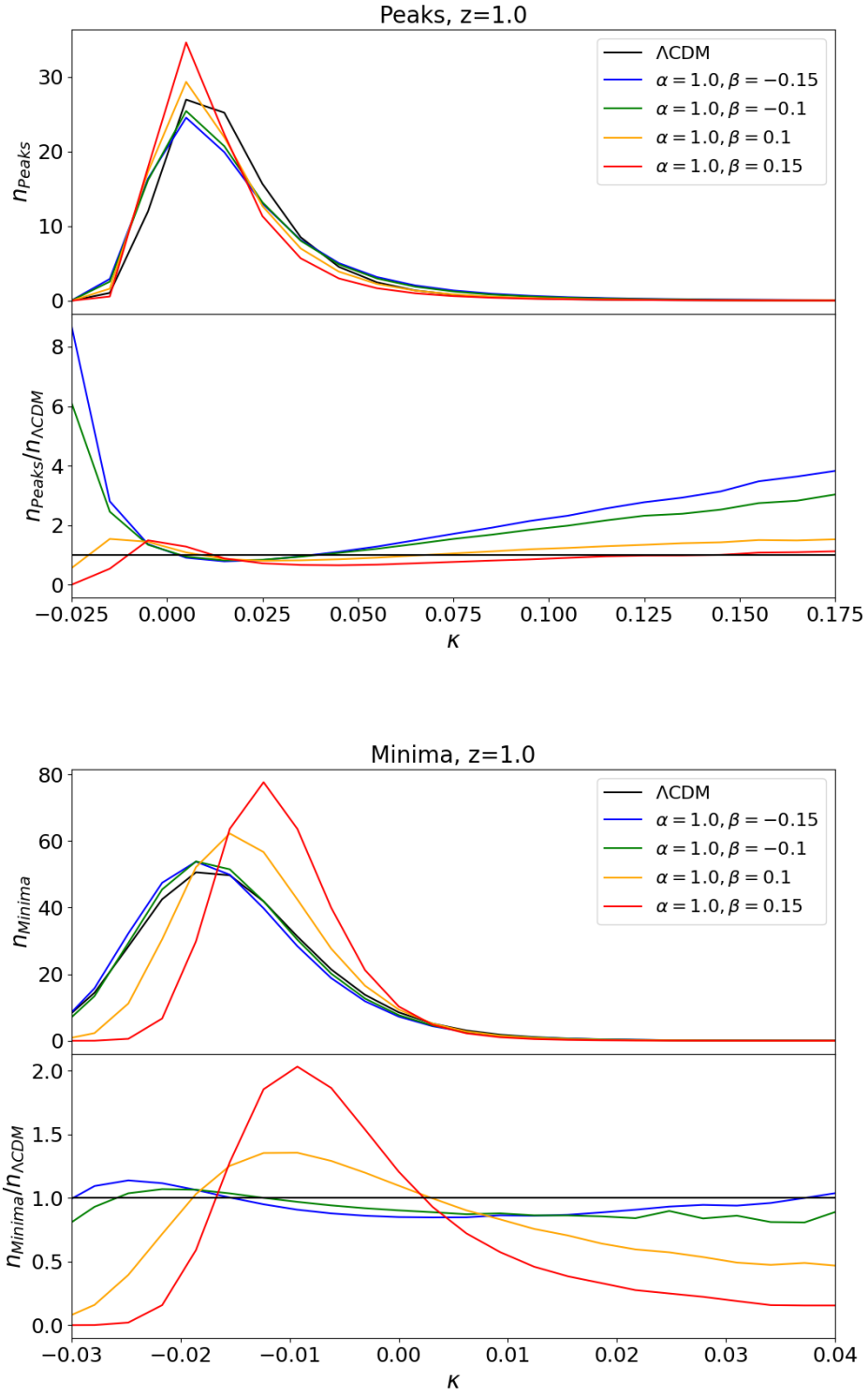

Figure 5.30: Peaks counts (*top*) and minima counts (*bottom*) for BCDE models, compared to ΛCDM model, for $z = 1.0$

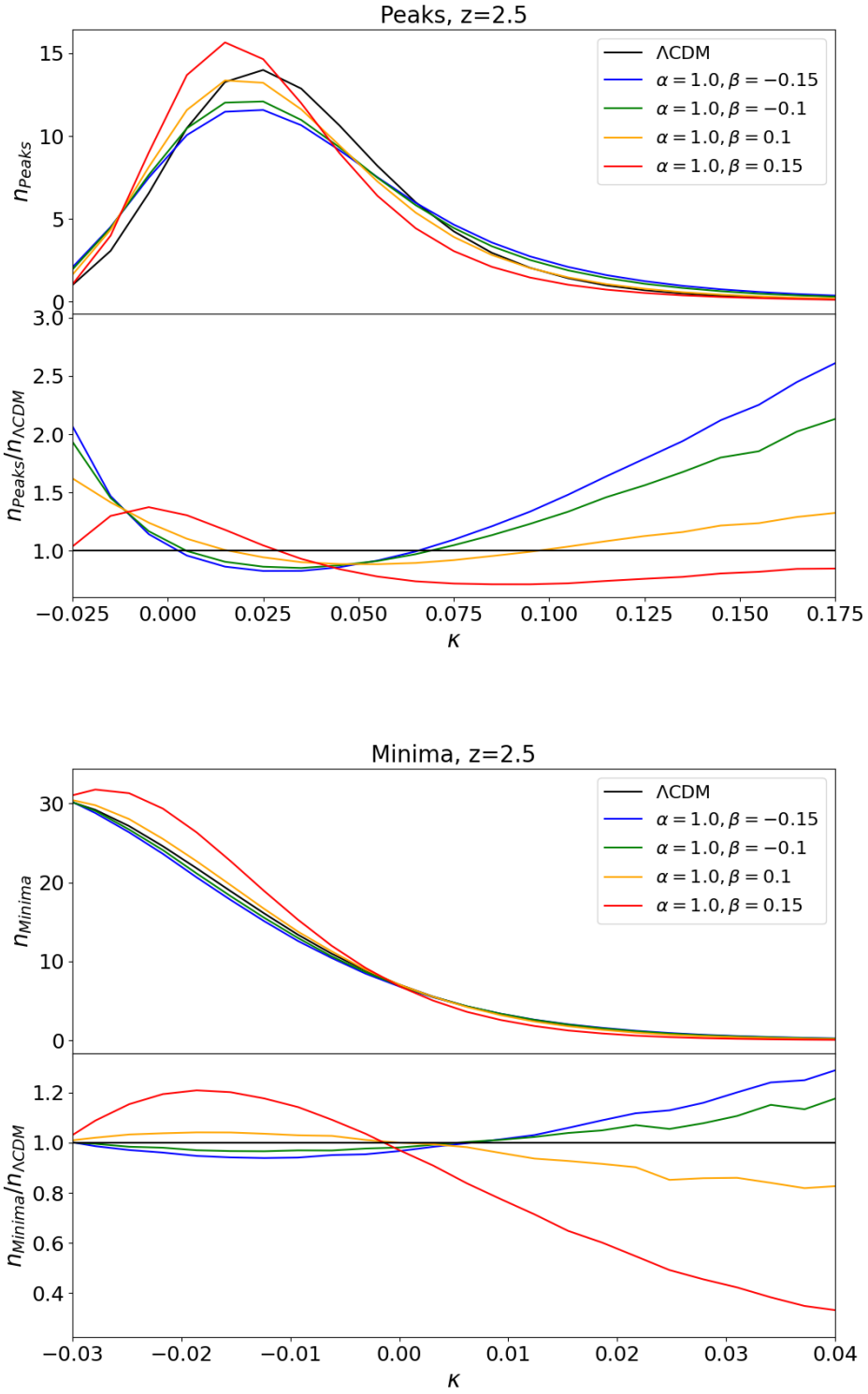

Figure 5.31: Peaks counts (*top*) and minima counts (*bottom*) for BCDE models, compared to ΛCDM model, for $z = 2.5$

Chapter 6

Conclusions

In this last chapter, we present a summary of the work carried out in this thesis, which aims to develop, implement, and validate a new version of the PANDA-GADGET-4 code to simulate cosmological observables such as matter and halo clustering and weak gravitational lensing for Coupled Dark Energy models. Alongside the code development, we also aim to validate the full simulation pipeline designed to study Coupled Dark Energy cosmologies. This pipeline combines *(i)* a numerical code, introduced in chapter 5.1, to investigate the background evolution and linear perturbations for general classes of interacting Dark Energy models; *(ii)* our newly developed implementation within the framework of the PANDA-GADGET4 code for nonlinear structure formation, offering a highly improved scalability and algorithm optimisations with respect to the previous C-Gadget3 implementation (Baldi, 2010) as well as a wide range of built-in output options, including 3D lightcones and spherical 2D mass maps; and *(iii)* the DORIAN library (Ferlito et al., 2025) to generate weak lensing observables along the simulated lightcone.

In chapter 1, we reviewed the fundamental principles of modern cosmology, including the FLRW metric, the Hubble law, and the growth of linear perturbations. We also highlighted the current observational tensions plaguing the ΛCDM model, such as the Hubble tension, the S_8 tension and the w_{DE} tension, which motivate the exploration of alternative theories like coupled dark energy.

In Chapter 2, we introduced dark energy models, starting with quintessence and extending to coupled dark energy scenarios. We discussed the unique features of BCDE models, where the scalar field evolves under a confining self-interaction potential, leading to a "bounce" in its trajectory. These models exhibit distinctive behaviors, such as time-varying particle masses, modified gravitational interactions and an extra velocity-dependent friction term, which can significantly impact the cosmic structure formation.

In Chapter 3, we provided an overview of numerical methods for simulating structure formation, focusing on the Tree-PM algorithm adopted by the GADGET-4 code. We also introduced PANDA-GADGET-4, an extension designed

to incorporate parameterized dark energy and modified gravity models, as preparation for the new PANDA-GADGET-4 implementation we developed to test Coupled Dark Energy features, discussed in the next chapter.

In Chapter 4, we detailed the modifications made to PANDA-GADGET-4 to enable the simulation of Coupled Dark Energy models. Our implementation builds upon the Coupled Dark Energy framework already available in the C-GADGET version of the GADGET-3 code. We extended this framework to PANDA-GADGET, which features a hybrid shared-distributed memory parallelisation scheme to minimise communication overheads and provide optimised scalability for large multicore HPC infrastructures. The Gadget4 code is written in the C++ programming language whereas all previous versions of Gadget have been written in standard C, which makes the porting of the modifications required for Coupled Dark Energy models far from trivial, and demands a careful validation of the new implementation to ensure its reliability. These modifications include implementing the mass variation for coupled particles dictated by the numerical solution of the scalar field dynamics, adding a velocity-dependent friction term (directly related to the scalar field evolution), and adapting the Tree-PM algorithm to account for the presence of a fifth force, as well as allowing the use of a modified background expansion encoded by a non-standard Hubble function $H(z)$.

We then validated our implementation by comparing results with the established C-GADGET code, achieving agreement within 1% for the nonlinear matter power spectrum.

In Chapter 5 we first analyze the background evolution and linear perturbations of different BCDE models to evaluate the impact of the coupling strength β and the potential slope α on the BCDE cosmology. We demonstrated how these models can simultaneously increase the Hubble parameter at late times while suppressing the growth of structures, offering a potential mitigation to the tensions observed within the ΛCDM cosmology. We then selected the most promising models to be simulated with our new PANDA-GADGET-4 implementation to investigate their effects on the nonlinear structure formation. Our analysis of the nonlinear matter power spectrum revealed significant deviations from ΛCDM. Models with positive coupling ($\beta > 0$) exhibit a suppression of power on large scales, while showing a notable enhancement in the nonlinear regime ($k > 1, h/\mathrm{Mpc}$). For instance, the A1BP15 model $\alpha = 1$, $\beta = +0.15$ exhibits a $\sim 20\%$ reduction in linear power at $z = 0$ and a $\sim 20\%$ increase in nonlinear regime ($k \gtrsim 0.5\, h/\mathrm{Mpc}$) at $z = 0$. Noticeably, however, this trend is strongly redshift-dependent, due to the oscillatory dynamics of the Dark Energy scalar field, and the same model – which is the one showing the largest deviations in our set of cosmologies – shows a $\gtrsim 15\%$ enhancement of the linear amplitude at $z = 2$.

Halo statistics further underscored these differences. Models with $\beta > 0$ displayed a significant reduction in halo abundance, particularly for high-mass

halos, with the A1BP15 model showing $> 50\%$ decrease in the number of halos with masses higher than $10^{14}\, M_\odot/h$ at $z = 0$. This suppression of high-mass halos is consistent with the late-time damping of structure growth caused by the friction term in BCDE models. In contrast, models with negative coupling ($\beta < 0$) remained closer to ΛCDM predictions, with only mild deviations. The A1BM15 model exhibits a halo abundance that nearly identical to ΛCDM at low redshifts (ratio remains under the 8% close to unity). The A2 models ($\alpha = 2.0, \beta_c < 0$) show a steeper reduction in the number of high-mass halos compared to their A1 ($\alpha = 1.0$) counterparts, highlighting the role of the potential slope in modulating structure formation.

Finally, we investigated the impact of BCDE cosmologies on Weak Lensing observables such as the convergence maps, the convergence angular power spectra, PDF, peaks and minima. Using the DORIAN library, we generated full-sky lensing observables and found that BCDE models generally produce weaker convergence signals, consistent with their suppressed growth of structure at late times.

The angular power spectrum of the convergence field κ revealed that almost all BCDE models exhibit lower power than ΛCDM for $z \leq 2.5$. The A1BP15 model, for instance, show a 60% reduction in the linear amplitude of the angular power spectrum relative to ΛCDM. Only the A1BM15 model displayed a slight excess in power at small scales ($\ell > 10^3$) for lensed sources at $z = 0.5$.

The Probability Density Function (PDF) of the convergence field κ further illustrated these differences. BCDE models consistently exhibited a higher probability for κ values near zero, while the tails of the distribution (both high and low κ) were suppressed compared to ΛCDM. This indicates that BCDE models produce fewer extreme density fluctuations, leading to a more concentrated distribution of convergence values around the mean. For lensed sources at $z = 2.5$, the A1BP15 model show a 25% higher probability for κ in the range $-0.035 \lesssim \kappa \lesssim 0.025$, while at $z = 0.5$ this effect became even more pronounced, with a 50% enhancement in probability for $-0.01 \lesssim \kappa \lesssim 0.01$.

Peaks and minima counts of the convergence field also highlighted the distinctive features of BCDE models. At $z = 2.5$, these models predicted an excess of low-κ peaks in the range $-0.01 \lesssim \kappa \lesssim 0.05$, which further shrinks at lower redshifts. The number of shallow minima, $-0.01 \lesssim \kappa \lesssim 0$, in BCDE models exceeded the ΛCDM prediction by a factor of 2 at $z = 2.5$ for the A1BP15 model, while deeper minima, $\kappa \lesssim -0.01$ were suppressed. These results align with the theoretical expectation that the friction term in BCDE cosmology dampens the growth of nonlinear density perturbations, reducing the prevalence of both high-density peaks and deep voids.

6.1 Future perspectives

The implementation of coupled dark energy (CDE) physics in `PANDA-GADGET-4` we have developed in this work represents a significant advancement in cosmological simulations, opening new avenues for exploring a wide range of interacting dark energy models. In particular, we demonstrated how Bouncing Coupled Dark Energy (BCDE) models with a specific choice of potential slope α and coupling strength β may possibly alleviate the current tensions within the ΛCDM cosmology.

While this work focused on BCDE models, which represents a specific subclass of coupled dark energy cosmologies, the modular design of our implementation allows for seamless integration of generic coupled dark energy scenarios. By decoupling the background and linear perturbation integration (provided to the code via external input tables) from the nonlinear structure formation (simulated in PANDA), our modified `PANDA-Gadget4` version is able to simulate a broad class CDE models without compromising computational performance.

The pipeline we developed in this work, combining background and perturbation analysis, nonlinear simulations with `PANDA-GADGET-4`, and weak lensing predictions with DORIAN, provides a powerful tool for constraining a wide range of interacting dark energy models.

While our new implementation in `PANDA-Gadget` achieves high accuracy (agreement with `C-GADGET` within 1%) the chosen $500 Mpc/h$ box size creates artificial repeating patterns when we generate full-sky weak lensing maps. Also, the number of particles we simulated (2×512^3) gives us decent resolution for tracking dark matter, but might contribute the 10% difference from expected results in the small-scale angular power spectrum (at scales smaller than 1 h/Mpc). To improve these results in future work, we could run larger simulations ($\geq 1 Gpc/h$) to reduce the repeating box effects. Addressing the current limitations, such as the 10% excess in the nonlinear power spectrum at small scales, could further refine the accuracy of our predictions. With upcoming cosmological surveys this pipeline will offer a powerful tool for testing and discriminating between cosmologies beyond the ΛCDM.

Bibliography

Abbott, B. P., Abbott, R., Abbott, T. D., Abernathy, M. R., Acernese, F., Ackley, K., Adams, C., Adams, T., Addesso, P., Adhikari, R. X., et al. (2016). Observation of gravitational waves from a binary black hole merger. *Physical review letters*, 116(6):061102.

Abbott, T. M., Aguena, M., Alarcon, A., Allam, S., Alves, O., Amon, A., Andrade-Oliveira, F., Annis, J., Avila, S., Bacon, D., et al. (2022). Dark energy survey year 3 results: Cosmological constraints from galaxy clustering and weak lensing. *Physical Review D*, 105(2):023520.

Aghanim, N., Akrami, Y., Ashdown, M., Aumont, J., Baccigalupi, C., Ballardini, M., Banday, A. J., Barreiro, R., Bartolo, N., Basak, S., et al. (2020). Planck 2018 results-vi. cosmological parameters. *Astronomy & Astrophysics*, 641:A6.

Akrami, Y., Arroja, F., Ashdown, M., Aumont, J., Baccigalupi, C., Ballardini, M., Banday, A. J., Barreiro, R. B., Bartolo, N., Basak, S., Benabed, K., Bernard, J. P., Bersanelli, M., Bielewicz, P., Bond, J. R., Borrill, J., Bouchet, F. R., Bucher, M., Burigana, C., Butler, R. C., Calabrese, E., Cardoso, J. F., Casaponsa, B., et al. (2019). Planck 2018 results. ix. constraints on primordial non-gaussianity.

Amendola, L. (2000). Coupled quintessence. *Physical Review D*, 62(4).

Amendola, L. (2004). Linear and nonlinear perturbations in dark energy models. *Physical Review D*, 69(10).

Baldi, M. (2010). Time-dependent couplings in the dark sector: from background evolution to non-linear structure formation: Time-dependent couplings in the dark sector. *Monthly Notices of the Royal Astronomical Society*, 411(2):1077–1103.

Baldi, M. (2011). Early massive clusters and the bouncing coupled dark energy: Bouncing dark energy and high-z clusters. *Monthly Notices of the Royal Astronomical Society*, 420(1):430–440.

Baldi, M. (2012). The codecs project: a publicly available suite of cosmological n-body simulations for interacting dark energy models. *Monthly Notices of the Royal Astronomical Society*, 422(2):1028–1044.

Baldi, M., Pettorino, V., Robbers, G., and Springel, V. (2010). Hydrodynamical n-body simulations of coupled dark energy cosmologies. *Monthly Notices of the Royal Astronomical Society*, 403(4):1684–1702.

Bartelmann, M. and Schneider, P. (2001). Weak gravitational lensing. *Physics Reports*, 340(4–5):291–472.

Bergström, L. (2012). Dark matter evidence, particle physics candidates and detection methods. *Annalen der Physik*, 524(9–10):479–496.

Bertone, G., Hooper, D., and Silk, J. (2005). Particle dark matter: evidence, candidates and constraints. *Physics Reports*, 405(5–6):279–390.

Brax, P. and Martin, J. (1999). Quintessence and supergravity. *Physics Letters B*, 468(1–2):40–45.

Breuval, L., Riess, A. G., Casertano, S., Yuan, W., Macri, L. M., Romaniello, M., Murakami, Y. S., Scolnic, D., Anand, G. S., and Soszyński, I. (2024). Small magellanic cloud cepheids observed with the hubble space telescope provide a new anchor for the sh0es distance ladder. *The Astrophysical Journal*, 973(1):30.

Burger, P. A., Friedrich, O., Harnois-Déraps, J., Schneider, P., Asgari, M., Bilicki, M., Hildebrandt, H., Wright, A. H., Castro, T., Dolag, K., Heymans, C., Joachimi, B., Kuijken, K., Martinet, N., Shan, H., and Tröster, T. (2023). KiDS-1000 cosmology: Constraints from density split statistics. *A&A*, 669:A69.

Carroll, S. M. (1998). Quintessence and the rest of the world: Suppressing long-range interactions. *Physical Review Letters*, 81(15):3067–3070.

Carroll, S. M. (2001). The cosmological constant. *Living Reviews in Relativity*, 4(1).

Chen, Z. and Yu, Y. (2024). Box replication effects in weak lensing light-cone construction. *Monthly Notices of the Royal Astronomical Society*, 534(2):1205–1216.

Chisari, N. E., Alonso, D., Krause, E., Leonard, C. D., Bull, P., Neveu, J., Villarreal, A., Singh, S., McClintock, T., Ellison, J., et al. (2019). Core cosmology library: Precision cosmological predictions for lsst. *The Astrophysical Journal Supplement Series*, 242(1):2.

Coles, P. and Lucchin, F. (2002). *Cosmology: The Origin and Evolution of Cosmic Structure, Second Edition*.

Congdon, A. B. and Keeton, C. R. (2018). *Principles of Gravitational Lensing: Light Deflection as a Probe of Astrophysics and Cosmology*.

Damour, T., Gibbons, G. W., and Gundlach, C. (1990). Dark matter, time-varying g, and a dilaton field. *Phys. Rev. Lett.*, 64:123–126.

Davis, M., Efstathiou, G., Frenk, C. S., and White, S. D. M. (1985). The evolution of large-scale structure in a universe dominated by cold dark matter. *The Astrophysical Journal*, 292:371–394.

DESI, C., Abdul-Karim, M., Adame, A. G., Aguado, D., Aguilar, J., Ahlen, S., Alam, S., Aldering, G., M., D., et al. (2025a). Data release 1 of the dark energy spectroscopic instrument.

DESI, C., Abdul-Karim, M., Aguilar, J., Ahlen, S., Alam, S., Allen, L., Prieto, C. A., Alves, O., Anand, A., U., et al. (2025b). Desi dr2 results ii: Measurements of baryon acoustic oscillations and cosmological constraints.

Di Valentino, E., Anchordoqui, L. A., Akarsu, Ö., Ali-Haimoud, Y., Amendola, L., Arendse, N., Asgari, M., Ballardini, M., Basilakos, S., Battistelli, E., et al. (2021a). Cosmology intertwined iii: fσ8 and s8. *Astroparticle Physics*, 131:102604.

Di Valentino, E., Anchordoqui, L. A., Akarsu, Ö., Ali-Haimoud, Y., Amendola, L., Arendse, N., Asgari, M., Ballardini, M., Basilakos, S., Battistelli, E., et al. (2021b). Snowmass2021-letter of interest cosmology intertwined ii: The hubble constant tension. *Astroparticle Physics*, 131:102605.

Di Valentino, E., Mena, O., Pan, S., Visinelli, L., Yang, W., Melchiorri, A., Mota, D. F., Riess, A. G., and Silk, J. (2021c). In the realm of the hubble tension—a review of solutions. *Classical and Quantum Gravity*, 38(15):153001.

Einstein, A. (1905). Zur elektrodynamik bewegter körper. *Annalen der Physik*, 322(10):891–921.

Einstein, A. (1915). Die Feldgleichungen der Gravitation. *Sitzungsberichte der Königlich Preussischen Akademie der Wissenschaften*, pages 844–847.

Einstein, A. (1917). Kosmologische Betrachtungen zur allgemeinen Relativitätstheorie. *Sitzungsberichte der Königlich Preussischen Akademie der Wissenschaften*, pages 142–152.

Ferlito, F., Davies, C. T., Springel, V., Reinecke, M., Greco, A., Delgado, A. M., White, S. D. M., Hernández-Aguayo, C., Bose, S., and Hernquist, L. (2025). Ray-tracing vs. born approximation in full-sky weak lensing simulations of the millenniumtng project.

Frenk, C. and White, S. (2012). Dark matter and cosmic structure. *Annalen der Physik*, 524(9–10):507–534.

Friedmann, A. (1922). Über die Krümmung des Raumes. *Zeitschrift fur Physik*, 10:377–386.

Frieman, J. A., Turner, M. S., and Huterer, D. (2008). Dark energy and the accelerating universe. *Annual Review of Astronomy and Astrophysics*, 46(1):385–432.

Galassi, M., Davies, J., Theiler, J., Gough, B., Jungman, G., Alken, P., Booth, M., Rossi, F., and Ulerich, R. (2002). *GNU scientific library*. Network Theory Limited Godalming.

Gómez-Valent, A., Pettorino, V., and Amendola, L. (2020). Update on coupled dark energy and the h_0 tension. *Physical Review D*, 101(12):123513.

Heymans, C., Tröster, T., Asgari, M., Blake, C., Hildebrandt, H., Joachimi, B., Kuijken, K., Lin, C.-A., Sánchez, A. G., Van Den Busch, J. L., et al. (2021). Kids-1000 cosmology: Multi-probe weak gravitational lensing and spectroscopic galaxy clustering constraints. *Astronomy & Astrophysics*, 646:A140.

Hubble, E. (1929). A Relation between Distance and Radial Velocity among Extra-Galactic Nebulae. *Proceedings of the National Academy of Science*, 15(3):168–173.

Jeans, J. H. (1902). The Stability of a Spherical Nebula. *Philosophical Transactions of the Royal Society of London Series A*, 199:1–53.

Joyce, A., Lombriser, L., and Schmidt, F. (2016). Dark energy versus modified gravity. *Annual Review of Nuclear and Particle Science*, 66(1):95–122.

Kilbinger, M. (2015). Cosmology with cosmic shear observations: a review. *Reports on Progress in Physics*, 78(8):086901.

Kodama, H. and Sasaki, M. (1984). Cosmological perturbation theory. *Progress of Theoretical Physics Supplement*, 78:1–166.

Komatsu, E., Smith, K. M., Dunkley, J., Bennett, C. L., Gold, B., Hinshaw, G., Jarosik, N., Larson, D., Nolta, M. R., Page, L., Spergel, D. N., Halpern, M., Hill, R. S., Kogut, A., Limon, M., Meyer, S. S., Odegard, N., Tucker, G. S., Weiland, J. L., Wollack, E., and Wright, E. L. (2011). Seven-year Wilkinson Microwave Anisotropy Probe (WMAP) Observations: Cosmological Interpretation. *The Astrophysical Journal Supplement*, 192(2):18.

La Vacca, G. L., Kristiansen, J., Colombo, L., Mainini, R., and Bonometto, S. (2009). Do wmap data favor neutrino mass and a coupling between cold dark matter and dark energy? *Journal of Cosmology and Astroparticle Physics*, 2009(04):007–007.

Lemaître, G. (1931). A homogeneous universe of constant mass and increasing radius accounting for the radial velocity of extra-galactic nebulae. *Monthly Notices of the Royal Astronomical Society*, 91:483–490.

Lewis, A., Challinor, A., and Lasenby, A. (2000). Efficient computation of cosmic microwave background anisotropies in closed friedmann-robertson-walker models. *The Astrophysical Journal*, 538(2):473–476.

Normann, B. D., Solevåg-Hoti, K., and Schaathun, H. G. (2024). A short review on joint weak and strong cluster lens-mass reconstruction.

Peebles, P. J. E. and Ratra, B. (2003). The cosmological constant and dark energy. *Reviews of Modern Physics*, 75(2):559–606.

Perlmutter, S., Gabi, S., Goldhaber, G., Goobar, A., Groom, D., Hook, I., Kim, A., Kim, M., Lee, J., Pain, R., et al. (1997). Measurements* of the cosmological parameters ω and λ from the first seven supernovae at z$\geq$ 0.35. *The astrophysical journal*, 483(2):565.

Perlmutter, S. and Schmidt, B. P. (2003). *Measuring Cosmology with Supernovae*, page 195–217. Springer Berlin Heidelberg.

Phillips, M. M. (1993). The absolute magnitudes of Type IA supernovae. *Astrophys. J. Lett.*, 413:L105–L108.

Poulin, V., Smith, T. L., Grin, D., Karwal, T., and Kamionkowski, M. (2018). Cosmological implications of ultralight axionlike fields. *Physical Review D*, 98(8).

Ratra, B. and Peebles, P. J. E. (1988). Cosmological consequences of a rolling homogeneous scalar field. *Phys. Rev. D*, 37:3406–3427.

Riess, A. G., Filippenko, A. V., Challis, P., Clocchiatti, A., Diercks, A., Garnavich, P. M., Gilliland, R. L., Hogan, C. J., Jha, S., Kirshner, R. P., et al. (1998). Observational evidence from supernovae for an accelerating universe and a cosmological constant. *The astronomical journal*, 116(3):1009.

Robertson, H. P. (1935). Kinematics and World-Structure. *The Astrophysical Journal*, 82:284.

Springel, V. (2005). The cosmological simulation code gadget-2. *Monthly Notices of the Royal Astronomical Society*, 364(4):1105–1134.

Springel, V. (2014). High performance computing and numerical modelling.

Springel, V. (2015). N-GenIC: Cosmological structure initial conditions. Astrophysics Source Code Library, record ascl:1502.003.

Springel, V., Pakmor, R., Zier, O., and Reinecke, M. (2021). Simulating cosmic structure formation with the ¡scp¿gadget¡/scp¿-4 code. *Monthly Notices of the Royal Astronomical Society*, 506(2):2871–2949.

Takahashi, R., Hamana, T., Shirasaki, M., Namikawa, T., Nishimichi, T., Osato, K., and Shiroyama, K. (2017). Full-sky gravitational lensing simulation for large-area galaxy surveys and cosmic microwave background experiments. *The Astrophysical Journal*, 850(1):24.

Velten, H. E. S., vom Marttens, R. F., and Zimdahl, W. (2014). Aspects of the cosmological "coincidence problem". *The European Physical Journal C*, 74(11).

Verde, L., Treu, T., and Riess, A. G. (2019). Tensions between the early and late universe. *Nature Astronomy*, 3(10):891–895.

Villaescusa-Navarro, F. (2018). Pylians: Python libraries for the analysis of numerical simulations. Astrophysics Source Code Library, record ascl:1811.008.

Walker, A. G. (1937). On milne's theory of world-structure. *Proceedings of the London Mathematical Society*, s2-42(1):90–127.

Weinberg, S. (2008). *Cosmology*.

Wetterich, C. (1988). Cosmology and the Fate of Dilatation Symmetry. *Nucl. Phys. B*, 302:668–696.

Wetterich, C. (1994). The cosmon model for an asymptotically vanishing time-dependent cosmological "constant".

White, S. D. M. (1994). Formation and evolution of galaxies: Les houches lectures. *arxiv preprint*.

Will, C. M. (2014). The confrontation between general relativity and experiment. *Living Reviews in Relativity*, 17(1).

Yadav, J., Bharadwaj, S., Pandey, B., and Seshadri, T. R. (2005). Testing homogeneity on large scales in the sloan digital sky survey data release one. *Monthly Notices of the Royal Astronomical Society*, 364(2):601–606.

Zel'dovich, Y. B. (1970). Gravitational instability: An approximate theory for large density perturbations. *Astronomy & Astrophysics*, 5:84–89.